

UNIVERSITY OF CALIFORNIA, SAN DIEGO

Experiments with the $l = 1$ Diocotron Mode

A dissertation submitted in partial satisfaction of the
requirements for the degree Doctor of Philosophy

in Physics

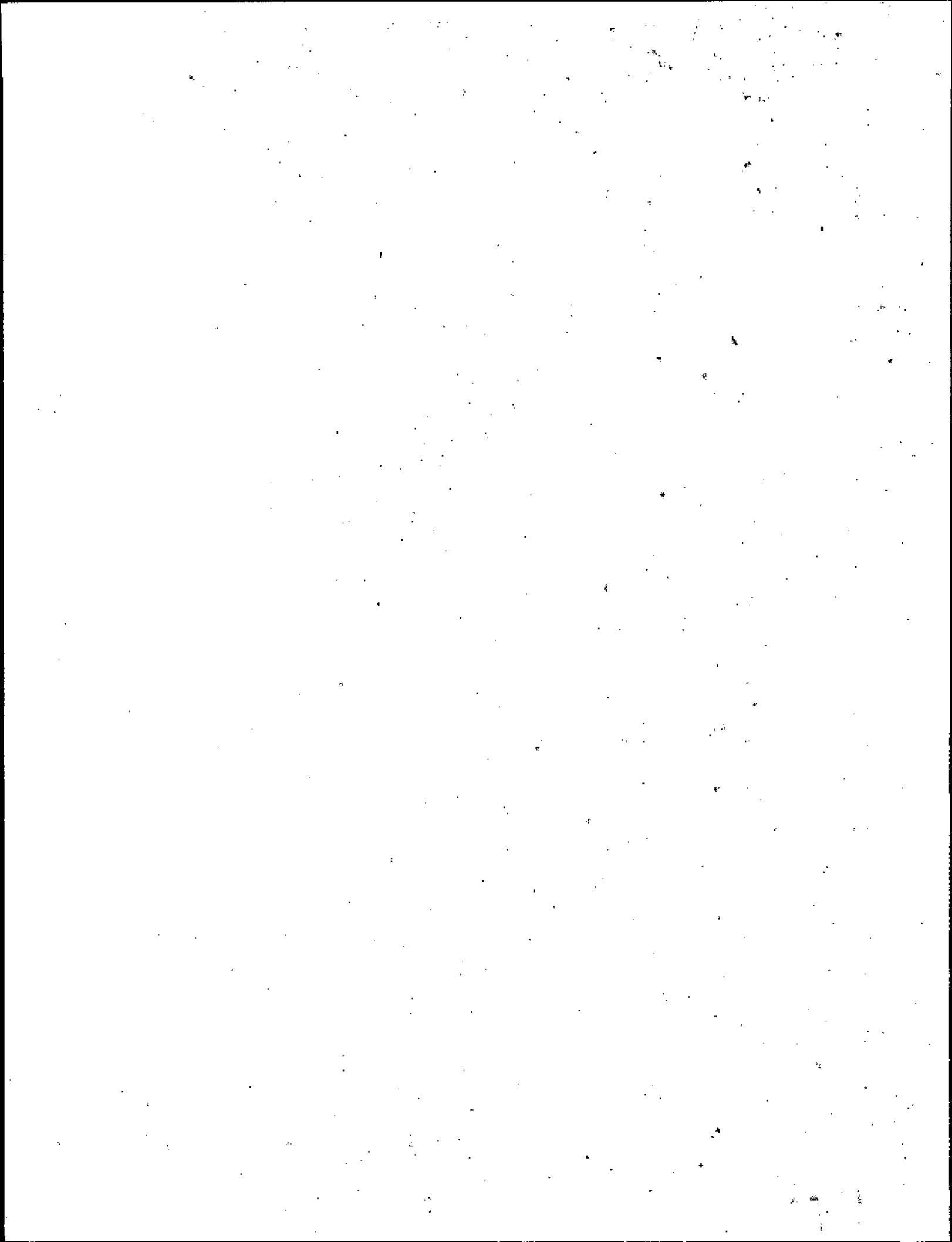
by

Kevin Sanford Fine

Committee in charge:

Professor John H. Malmberg, Chairman
Dr. C. Fred Driscoll, Co-Chairman
Professor Thomas M. O'Neil
Professor Carl E. McIlwain
Professor David R. Miller
Professor Manuel Rotenberg

1988



The dissertation of Kevin Sanford Fine is approved, and it is
acceptable in quality and form for publication on
microfilm:

David R. Miller

Thomas O'Meal

Daniel K. Stenberg

Carl E. McAlwain

Charles F. Driscoll

John H. Malmsberg Co-Chairman
Chairman

University of California, San Diego

1988

3.2	The Image Charge Model of the Diocotron Mode	26
3.3	The Signal on a Sector Probe from a Diocotron Mode	29
3.4	Resistive Growth of the Diocotron Mode	32
3.5	Feedback Growth and Damping	33
4	The Large Amplitude Diocotron Mode	39
4.1	Overview	39
4.2	Phase-Locked Density Measurements	41
4.2.1	Experimental Setup	41
4.2.2	Distortion of Plasma Shape	44
4.3	Frequency Measurements	47
4.3.1	Measurement of Frequency and Displacement	47
4.3.2	Frequency versus Displacement	48
4.3.3	Simple Model of Nonlinear Frequency Shift	52
4.4	The Waterbag Model	55
4.5	Comparison with Calculation of Prasad and Malmberg	56
5	The Finite Length Diocotron Mode	59
5.1	Overview	59
5.2	Theory	61
5.3	Shifts in the Real Part of the Frequency	67
5.4	Shifts in the Imaginary Part of the Frequency	71
6	Induced Damping and Transport from External Field Perturbations	76
6.1	Overview	76
6.2	Axisymmetric Electrostatic Field Perturbations (Squeeze)	78
6.2.1	Measurement of Induced Diocotron Mode Damping	78

6.2.2	Relation to Beat-Wave Theory	84
6.2.3	Radial Transport due to Squeeze	86
6.3	Magnetostatic $l = 1$ Field Perturbations (Tilt)	90
A	Estimate of Electron Loss inside Collimator Hole	97
B	Image Charge in Cylindrical Geometry	101
References	103

List of Figures

2.1	Schematic diagram of the EV apparatus.	10
2.2	Radial density profiles with and without tilt.	17
2.3	Confinement time versus L_p/B_z	19

List of Tables

5.1	Comparison between diocotron damping rates predicted by the theory of Prasad and O'Neil and experimental measurements.	73
6.1	Mode numbers and frequencies for squeeze, diocotron and beat waves.	85

Acknowledgements

I would like to thank my two advisors, Prof. John Malmberg and Dr. Fred Driscoll. Prof. Malmberg has shown me what it takes to be a first-rank physicist: all that is needed is a great intellect, a lively creativity, the tenacity of a bulldog, and a sparkling wit. In my almost daily contact with Dr. Driscoll I have learned much about the trade of being a physicist. Most especially, he has taught me the crucial lesson that details should never obscure the broad perspective.

Prof. Tom O'Neil has provided invaluable insight into theory. Drs. S. A. Prasad and J. D. Crawford have also been generous with their theoretical help, as has Prof. Dan Dubin. A number of post-docs and graduate students have helped, among them Warren White, Al Hyatt, Bret Beck, Poul Hjorth, Joel Fajans, Dennis Eggleston and Stan Tsunoda. Tim Mitchell proofread the thesis. Looking at the names above, I realize that the Malmberg group is really a group of friends that I have happened to work with.

Bonnie Horstmann in the department office has helped me many times over the years. JoAnn Christina has kept the group running smoothly and has also been a good friend. Fellow graduate students Greg Elliott, Gabe Lengua, Agusta Flosadottir, and Kerry Buckland have become lifelong pals.

Many people outside the department have provided encouragement over the years, notably my parents and my brother Neal, Bill Lackey and Kevin Carps. Mike Smith and Tavier Gamboa have helped me in the long run. And thanks to

that wonderful lady who has been a big influence since elementary school, Hattie Highfield.

Financial support for this research was provided by ONR Contract N00014-82-K-0621, NSF Grant PHY87-06358 and DOE Grant DE-FG03-85ER53199.

Vita, Publications and Fields of Study

Vita

5 August 1954	Born, High Point, North Carolina
1972-1976	B.S., University of North Carolina at Chapel Hill
1976-1978	M.S., Massachusetts Institute of Technology
1979	Research Assistant, National Magnet Lab, Cambridge Massachusetts
1980	Systems Analyst, Intermetrics, Inc., Huntington Beach, California
1980-1988	Ph.D., University of California, San Diego

Publications

1. C. F. Driscoll, K. S. Fine and J. H. Malmberg. Reduction of radial losses in a pure electron plasma. *Bull. Am. Phys. Soc.*, 29:1279 (1984).
2. A. W. Hyatt, J. H. Malmberg, C. F. Driscoll, K. S. Fine, B. R. Beck and D. L. Eggleston. Observation of anisotropic temperature relaxation. *Bull. Am. Phys. Soc.*, 30:1552 (1985).
3. C. F. Driscoll, K. S. Fine and J. H. Malmberg. Transport to thermal equilibrium in pure electron plasmas. *Bull. Am. Phys. Soc.*, 30:1552 (1985).
4. C. F. Driscoll, K. S. Fine and J. H. Malmberg. Reduction of radial losses in a pure electron plasma. *Physics of Fluids*, 29:2015, 1986.
5. K. S. Fine, W. D. White, J. H. Malmberg and C. F. Driscoll. Induced damping of a diocotron wave and associated transport. *Bull. Am. Phys. Soc.*, 31:1391 (1986).
6. C. F. Driscoll, K. S. Fine and J. H. Malmberg. Enhanced like-particle transport in pure electron plasmas. *Bull. Am. Phys. Soc.*, 31:1392 (1986).
7. C. F. Driscoll, J. H. Malmberg and K. S. Fine. Like particle transport scaling as B^{-1} in pure electron plasmas. *Bull. Am. Phys. Soc.*, 32:1754 (1987).
8. K. S. Fine, C. F. Driscoll and J. H. Malmberg. Large amplitude and finite length effects in diocotron modes. *Bull. Am. Phys. Soc.*, 32:1755 (1987).
9. C. F. Driscoll, J. H. Malmberg and K. S. Fine. Observation of transport to thermal equilibrium in pure electron plasmas. *Physical Review Letters*, 60:1290, 1988.
10. K. S. Fine, C. F. Driscoll and J. H. Malmberg. Measurements of a nonlinear diocotron mode. *Bull. Am. Phys. Soc.*, 33 (1988) (To be published).
11. J. H. Malmberg, C. F. Driscoll, B. R. Beck, D. L. Eggleston, J. Fajans, K. S. Fine, X-P. Huang and A. W. Hyatt. Experiments with pure electron plasmas. To appear in *Nonneutral plasma physics* (C. W. Roberson and C. F. Driscoll, eds.), AIP Conf. Proceedings 175:34, 1988.
12. C. F. Driscoll, J. H. Malmberg, K. S. Fine, R. A. Smith, X-P. Huang and R. W. Gould. Growth and decay of turbulent vortex structures in pure electron plasmas. To be published in *Proc. of 12th International Conference on Plasma Physics and Controlled Nuclear Fusion*, I.A.E.A., 1988.

Fields of Study

Major Field: Physics

Studies in Plasma Physics

Professors John H. Malmberg, Thomas M. O'Neil and
William B. Thompson

Studies in Mechanics

Professor Thomas M. O'Neil

Studies in Electromagnetism

Professor Robert A. Swanson

Studies in Quantum Mechanics

Professors Norman M. Kroll and Harry Suhl

Studies in Statistical Mechanics

Professor Robert J. Gould

Studies in Nuclear Physics

Professor Keith A. Brueckner

Studies in Mathematical Physics

Professor Audrey Terras

Abstract of the Dissertation

Experiments with the $l = 1$ Diocotron Mode

by

Kevin Sanford Fine

Doctor of Philosophy in Physics

University of California, San Diego, 1988

Professor John H. Malmberg, Chairman

Dr. Charles F. Driscoll, Co-Chairman

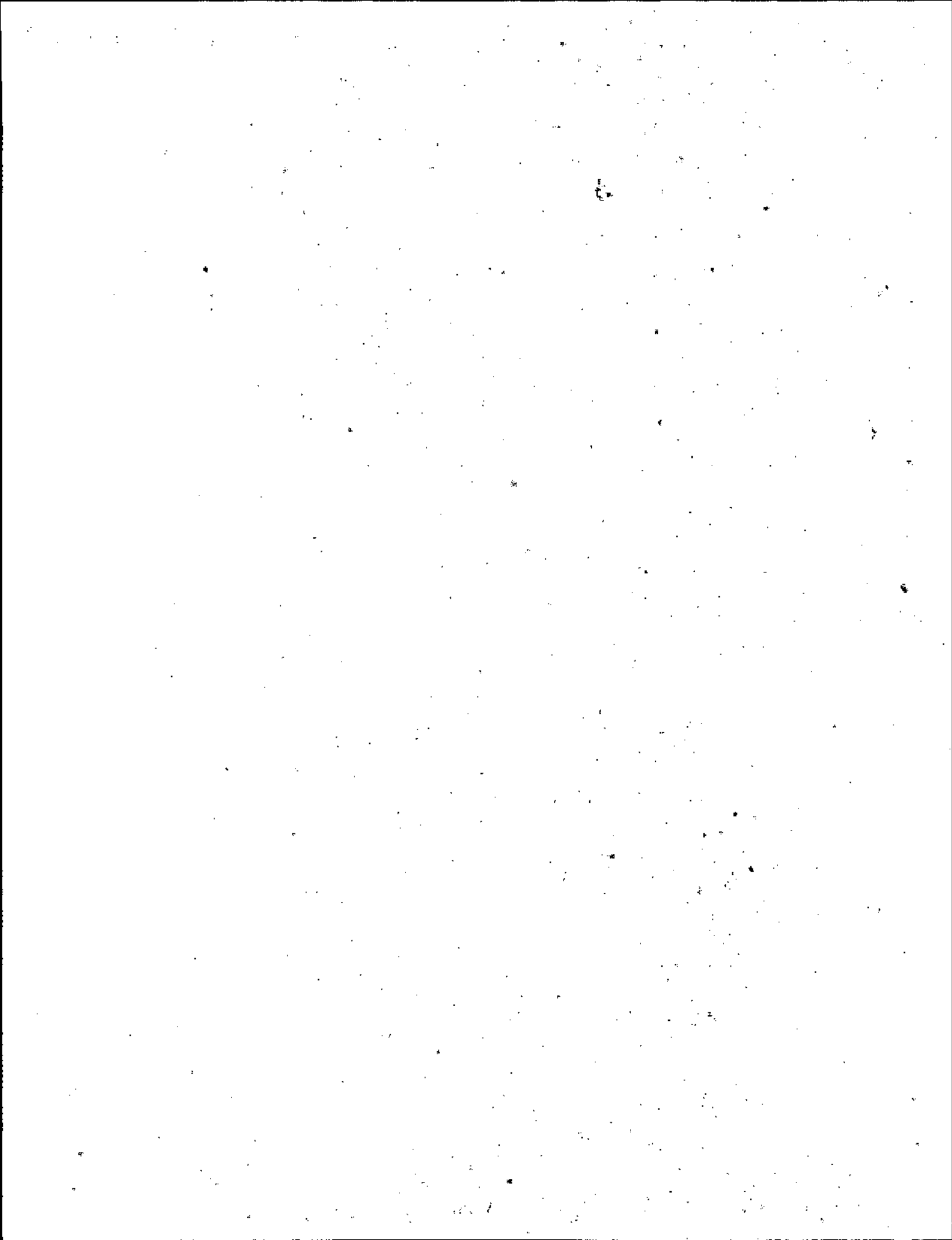
Experiments are presented on a particularly interesting oscillatory mode in pure electron plasmas. The plasmas studied are columns contained inside conducting cylinders in an axial magnetic field. Traditional theory models diocotron modes as surface density perturbations; the mode of interest has azimuthal mode number $l = 1$ (*i.e.* varying as $\cos \theta$) and is essentially independent of axial position (*i.e.* $k_z \approx 0$). At large amplitude the mode is more correctly viewed as a dynamical equilibrium in which the plasma column is offset by a displacement, D , and drifts around the cylindrical axis.

The frequency, f , of the mode is observed to vary with amplitude as $\Delta f \propto D^2$. This frequency shift arises because 1) the plasma is closer to its image charge than a linear model assumes, and 2) the plasma distorts from a circular shape. From measurements of $n(r, \theta)$ it is seen that at large amplitudes the column shape becomes elliptical with elongation in the θ -direction. The distortion and frequency shifts are such as to make the density stationary in a frame rotating at the mode

frequency.

The small-amplitude frequency of the diocotron mode in an infinite length column, f_d , depends only on the charge per unit length. Measurements of frequency have been made versus plasma length, L_p , and plasma radius, R_p . The mode frequency is found to be up to 200% higher in short plasmas, and the fractional frequency shift increases as L_p^{-1} and decreases with R_p . These observations are in agreement with linear theory. Finite length theory also predicts damping of the diocotron mode. Measurements indicate that mode damping is at least three orders of magnitude smaller than predicted: the mode oscillates 10^5 cycles with negligible change in amplitude.

Finally, the effects of two field perturbations have been studied. An axisymmetric electrostatic field induces exponential damping in the diocotron mode. The other is a small (10^{-3} rad) tilt of the magnetic field that induces mode damping, as well as particle transport towards a square, low-noise density profile.



Chapter 1

Introduction and Summary

This thesis presents experiments on a particularly interesting oscillatory mode in pure electron plasmas. The plasmas studied are columns contained inside conducting cylinders in an axial magnetic field. Traditional theory models diocotron modes as surface density perturbations; the mode of interest has azimuthal mode number $l = 1$ (*i.e.* varying as $\cos \theta$) and is essentially independent of axial position (*i.e.* $k_z \approx 0$). At large amplitude the mode is more correctly viewed as a dynamical equilibrium in which the plasma column is offset by a displacement, D , and drifts around the cylindrical axis. I have studied this mode at large amplitude, when the plasma column is relatively short, and when external field perturbations are applied.

The word 'diocotron' was first used to describe instabilities in hollow electron columns [2,3,6,13,29]. The instabilities were thought to be driven by shears in the plasma rotation velocity, and the word diocotron originates from the Greek word 'διωκειν', meaning 'pursue'. The word now generally refers to low frequency electrostatic oscillations perpendicular to the magnetic field, including mixed modes with z -dependence as well.

DeGrassie and Malmberg first measured the properties of diocotron modes in confined pure electron columns [8]. Most of their measurements were performed

on columns that had monotonically decreasing density profiles. For such profiles the modes are basically density perturbations on the plasma surface that interact with the conducting wall. I will call these modes 'outer' modes.

DeGrassie and Malmberg also reported that hollow electron plasma columns were unstable on a timescale of 50 μsec . In recent months, it has been discovered that these instabilities in hollow electron columns [12,28] are distinct from the outer diocotron modes. This second set of unstable diocotron modes is primarily due to interactions between the inner and outer surfaces of the column. I will call these modes 'inner' modes. These inner modes are being experimentally investigated by Driscoll, *et. al.* [12], and these researchers find that the instabilities produce rapid transport towards a monotonically decreasing profile.

The experiments discussed in this thesis were performed exclusively with monotonically decreasing density profiles, and only outer diocotron modes are discussed. In particular, I will discuss only the $l = 1$, $k_z \approx 0$ diocotron mode.

The experiments were performed on a pure electron plasma containment device that was designed to minimize radial transport and loss of the plasma. The apparatus contains a column of electrons in ultra-high-vacuum (5×10^{-11} Torr) in a uniform axial magnetic field ($0 < B_z < 470$ gauss). The electron column has a density $n < 10^7 \text{ cm}^{-3}$, a radius $R_p < 3$ cm, and a length $2 < L_p < 40$ cm. The plasma kinetic energy is typically about 1 eV, which is small compared to the electrostatic energy per particle of $-e\phi \sim 20$ eV. The contained plasma has a lifetime which depends on n , L_p , and B_z , being around 100 seconds for the experiments described herein.

The plasma density is measured by dumping the electrons axially and measuring the charge Q which passes through a collimator hole at a particular radial position. By repeating this measurement many times on identical plasmas, but

varying the position of the hole, $Q(r)$ is obtained. For axisymmetric plasmas, a computer solution of Poisson's equation in (r, z) is used to determine the plasma shape at the ends from $Q(r)$, and to obtain the density $n(r, z)$. The density measurement can be calibrated to 1%.

We are also able to measure the average kinetic energy of the plasma electrons, $T(r)$, although this energy is not important for the modes of interest. Note that the measurement of both $T(r)$ and $Q(r)$ rely on the high degree of shot-to-shot reproducibility of the plasma.

When a diocotron mode is present, the plasma is dumped at a variable phase of the wave to obtain the phase-locked charge $Q(r, \theta)$. For long plasmas, the density can be estimated as $n(r, \theta) \approx Q(r, \theta)/(-eA_h L_p)$, where L_p is the plasma length, and A_h is the collimator hole area. This measurement allows a complete characterization of the dynamics of the wave, to the extent the dynamics is independent of the axial position z .

The diocotron mode is essentially an offset of the plasma column from the conducting wall axis by a displacement, D . The electric field can be calculated using the method of images: the image charges in the conducting wall are replaced by a rod of charge at a particular position outside the wall. The diocotron motion is the $\mathbf{E} \times \mathbf{B}$ drift of the column in the electric field of this image charge.

The diocotron mode can be measured and manipulated with sector probes. Sector probes are electrically isolated wall patches that capacitively couple to the plasma. The signal produced on a sector probe by the diocotron mode consists of a fundamental component at the mode frequency plus harmonics. The displacement can be calculated from the measured $n(r, \theta)$, and using this measure of D I have found that the amplitude of the fundamental component is proportional to D . The coefficient is in good agreement with a theory by Kapetanacos and Trivelpiece [17],

once an algebraic error in the theory is corrected. Also, the second harmonic agrees well with theory.

A feedback circuit connected between a 'receiver' probe and a 'transmitter' probe can be used to grow the diocotron mode to large amplitudes and to damp the mode to levels comparable with noise. It is striking that the mode can be grown, then damped, with negligible change in the density profile. I find that the growth and damping rate depend on amplifier gain and phase, in good agreement with a simple calculation based upon an energy argument.

Measurements have been made of the frequency and phase-locked density $n(r, \theta)$ of a large amplitude diocotron mode. I find that prior theories are inadequate at describing the mode at large amplitude, but that most effects can be understood from my image charge model. The mode frequency shifts from its low amplitude value by an amount proportional to D^2 . This frequency shift is understood as being due to two effects: 1) the plasma is closer to its image charge than a linear model assumes, and 2) the plasma distorts from a circular shape. From the plots of $n(r, \theta)$, it can be seen that at large amplitudes the column shape becomes elliptical with elongation in the θ -direction. The distortion and frequency shifts are in excellent agreement with a waterbag computer code. The code iterates both the frequency and plasma shape until the plasma boundary is coincident with a potential contour in a frame rotating at the diocotron frequency. This condition implies that the plasma density is time-invariant in this rotating frame.

Finite length effects are important even for small amplitude diocotron modes. I have measured the diocotron frequency as a function of L_p and plasma radius, R_p . The image charge model predicts a mode frequency, f_d , that depends only upon charge per unit length in the column. I have found that the measured frequency, f , is up to 200% higher in short plasmas. The fractional frequency shift

$(f - f_d)/f_d$ increases as L_p^{-1} and decreases with R_p . This is in reasonable agreement with a finite length theory of Prasad and O'Neil [27,26].

Finite length theory suggests that couplings to other plasma modes may induce damping in the $l = 1$ diocotron mode. I have measured the damping rate of the finite length diocotron mode at various B_z and amplitudes. In all cases, the diocotron mode was found to not be damped to within the accuracy of the measurement. The quality factor, Q , of this resonance was determined to be greater than 10^7 . The measurements indicate that the mode damping is at least three to four orders of magnitude smaller than the theory predicts.

Finally, I have measured the effect on the plasma of two externally applied field perturbations. The 'squeeze' perturbation is an axisymmetric electric field which squeezes the plasma towards one end; and the tilt perturbation is a tilt of the magnetic field with respect to the conducting wall axis. I find that the previously stable diocotron mode becomes exponentially damped when these fields are applied. Extensive measurements of the diocotron damping rate were made for the case of the squeeze perturbation. The damping rate scales as perturbation amplitude squared. A possible explanation agreeing with these scalings is a nonlinear interaction proposed by Crawford, O'Neil and Malmberg [5]. It may be that the squeeze damping of the diocotron wave is a particularly simple example of this nonlinear effect.

The tilt perturbation also produces a remarkable transport towards a square density profile and a flat temperature profile. There is in addition a reduction in the shot-to-shot variability to about 0.1%, as compared to a variability of 1% before the tilt-induced transport. The tilt field is an important experimental technique in obtaining repeatable plasma samples of uniform density and temperature. So far, the effect has no carefully derived theoretical explanation.

These results are explained in detail in the following chapters. Each chapter begins with an overview that summarizes the main ideas and results of the chapter.

Chapter 2

Design and Operation of the EV Experiment

2.1 Overview

The EV experiment will be described in this chapter. (The acronym EV derives from Equilibrium plasma, Voltage containment.) Basically, the apparatus produces stable, repeatable electron plasmas that can be varied from 2 to 40 cm in length and 1.3 to 2.9 cm in radius. The density is about 10^7 electrons per cc, and the plasma is immersed in a uniform magnetic field that can be varied up to 500 gauss. A typical temperature is about 1 eV. For these parameters, the cyclotron radius is much smaller than the Debye length, and there are about three to eight Debye lengths in a plasma radius.

The main diagnostic is a density measurement. Essentially, the plasma is dumped along the magnetic field and a fraction of the electrons pass through a hole in a collimator plate. The electrons passing through the collimator hole then encounter a collector. The measured capacitance of the collector is used to calculate the number of electrons from the voltage produced by the electrons. This measurement is repeated with the collimator hole at different radial locations until a radial profile of the z -integrated charge, $Q(r)$, is compiled.

An independent Gauss's Law measurement has been used to check the

accuracy of the density measurement. I find that the density measurement can be low by as much as four percent, probably due to electrons colliding with the edges of the collimator hole due to the cyclotron motion. Nevertheless, the accuracy is better than one percent if the radial integral of the profile is normalized to the total number of electrons, which is measured separately by the collimator plate.

The EV apparatus has a perpendicular temperature analyzer that measures the temperature as a function of radius. We routinely use these temperatures along with charge profiles, $Q(r)$, as input to a computer program that solves for density, $n(r, z)$, as a function of r and z . This calculation relies upon the assumption that the plasma has a Boltzmann distribution in z . The density can then be used to compute plasma length, L_p , and number of electrons per axial length, N_L . Both L_p and N_L are used in the analysis of finite length effects in Chapter 5.

The angular momentum, P_θ , can be obtained directly from radial profiles of $Q(r)$. Theory states that the angular momentum of the plasma should be conserved under the influence of axisymmetric perturbations. The measurement of P_θ will be used in Chapter 6 to test this hypothesis for the symmetrical 'squeeze' field. I find that the contribution of the wall charges to P_θ should be included if changes in P_θ are to be meaningful.

Conservation of P_θ implies that the plasma is radially confined [21]. There is background loss, however, which is due to cylindrically asymmetric fields coupling to the plasma. The main objective in designing the EV apparatus was to minimize these couplings. The result is that the EV apparatus has containment times a factor of 20 better than the previous apparatus. This background loss of electrons is a basic limit to some experimental measurements, such as the long time damping of the diocotron wave.

Finally, the chapter is concluded with a short discussion of the dramatic

effect of field tilt. I have found that if the magnetic field is tilted by a small amount ($\sim 10^{-3}$ radians) with respect to the containment cylinder axis for a short period (~ 1 second), the radial profile becomes very square in shape and the shot-to-shot variability decreases by a factor of ten. This effect will be discussed in more detail in Chapter 6. It is such an important technique that it is used in almost all the experiments in this thesis.

2.2 Overview of the Apparatus

A schematic of the EV apparatus is shown in Fig. 2.1. The apparatus essentially consists of a filament source, cylindrical conducting electrodes, a temperature analyzer, and charge collectors. These electrodes are enclosed in an ultra-high vacuum chamber (pressure $\sim 5 \times 10^{-11}$ Torr) in a uniform axial magnetic field, B_z . The value of B_z can be varied up to about 500 gauss. During both design and construction, prime consideration was given to minimizing all loss processes, so that the plasma would relax to a confined state at thermal equilibrium.

The source of electrons is a directly heated spiral of tungsten wire. The center of this spiral is biased negatively with respect to ground, to potential V_b ; usually, V_b is between -20 Volts and -35 Volts. For the quiescent injection normally used, the space charge potential of the plasma closely matches the filament potential. Typical plasma density is $\sim 10^7 \text{ cm}^{-3}$ and typical plasma temperature is ~ 1 eV. The electron plasma contains a negligible number of positive ions, since ions are not confined longitudinally.

The apparatus is operated in an inject, hold, dump and measure cycle. For injection, the inject cylinder is briefly grounded, while the dump cylinder is biased to V_c ($V_c \sim -100$ Volts). The plasma then forms a column between the source and the dump cylinder, with continuous emission and reabsorption by the filament.

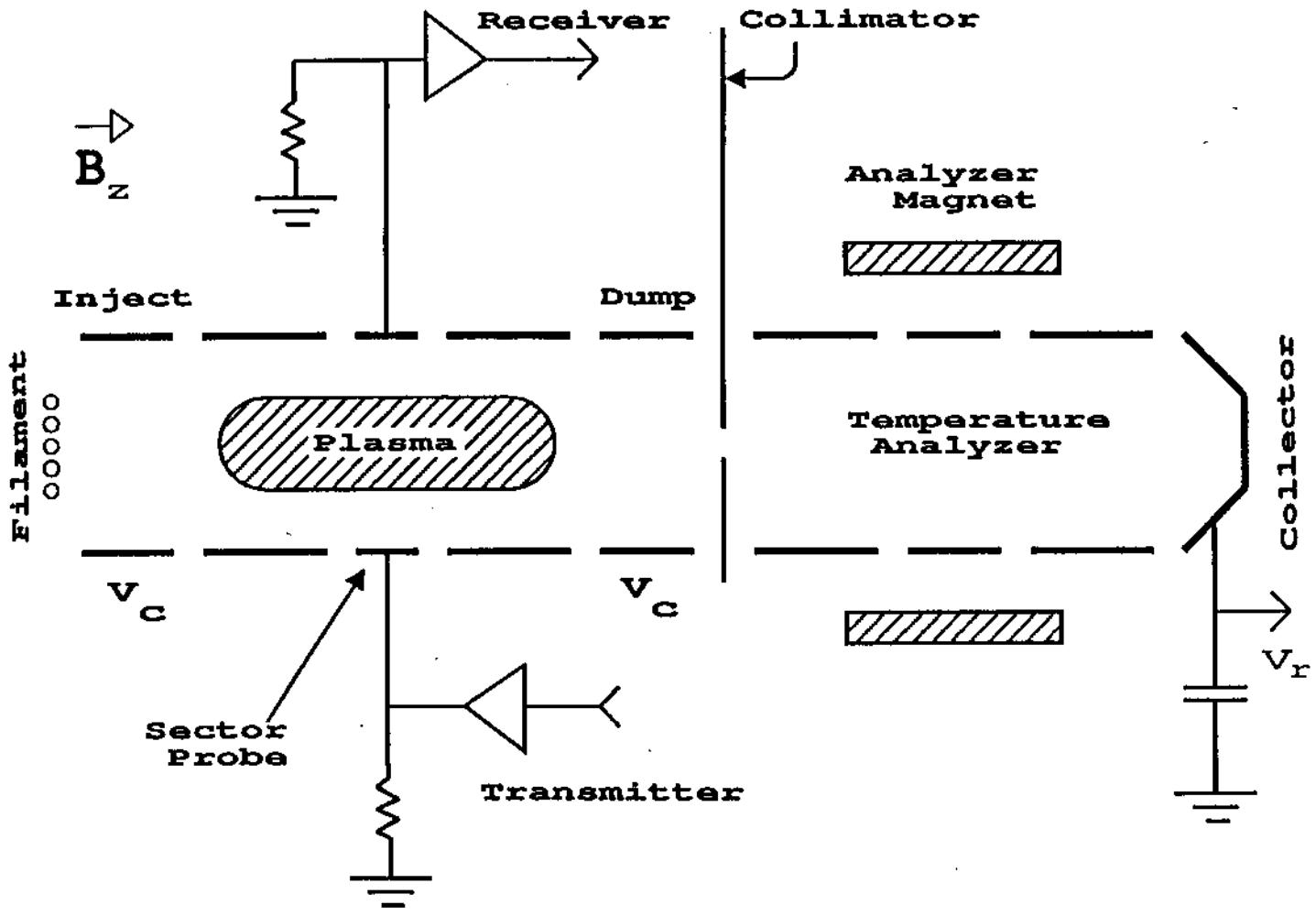


Figure 2.1: Schematic diagram of the EV apparatus.

This injection configuration is established for approximately 100 μsec , and then the inject cylinder is ramped to V_c . This reflects the incoming electrons and traps the column. The cylinders between the inject and dump cylinders are grounded. Since there is actually a stack of eight electrically separate cylindrical electrodes to the left of the collimator plate in Fig. 2.1, the length of the containment cylinders, L_c , can be varied in discrete steps from 4.1 cm to 43.5 cm. The radius of all cylindrical electrodes is 3.81 cm, which I will denote by R_w .

2.3 Radial Density Measurements

After a chosen hold time, the dump cylinder is pulsed to ground potential, and the electrons stream along the magnetic field to the collimator and collector. Repeating the cycle with the collimator hole at varying radii allows us to construct a radial density profile of the plasma. I am assuming here that the plasma is cylindrically symmetric around the conducting wall axis; density measurements of θ dependent profiles will be discussed in Chapter 4.

Our basic density measurement is the total charge $Q(r)$ which exists along a field line at radius r and angle θ , and passes through the collimator hole of area $A_h = 0.08 \text{ cm}^2$ (0.159 cm radius). This is the z integral of the plasma density:

$$Q(r) = -eA_h \int dz n(r, z), \quad (2.1)$$

where e is the proton charge.

I routinely use the measurement of $Q(r)$, along with temperature measurements and the boundary conditions at the wall, to calculate $n(r, z)$. Assume that the plasma maintains a Boltzmann distribution along each field line, so that Poisson's equation becomes

$$\nabla^2 \phi(r, z) = \frac{n(r, z)e}{\epsilon_0} = \frac{n_0(r)e}{\epsilon_0} \exp\left(\frac{e\phi(r, z)}{kT(r)}\right), \quad (2.2)$$

with boundary conditions $\phi(R_w, z) = 0$ for $-L_c/2 < z < +L_c/2$ and $\phi(R_w, z) = V_c$ for $L_c/2 < |z|$. The function $n_0(r)$ is chosen so that Eq. 2.1 is satisfied. Eq. 2.2 is solved numerically using an iterative calculation: a guess is made for $n(r, z)$ and this is used with the boundary conditions to calculate $\phi(r, z)$, which is in turn used to calculate a new guess for $n(r, z)$. A fraction of the new solution for $n(r, z)$ is added to the old solution, taking care to satisfy Eq. 2.1. This process is repeated until the maximum change in $n(r, z)$ is smaller than a given parameter (usually 10^3 electrons per cm^3).

The finite size of the cyclotron radius, r_c , has an effect upon the radial density measurements. At the lowest values of B_z used, only about six cyclotron orbits will fit side by side across the collimator hole. During the time the electrons are passing through the hole, the electrons continue to move along the cyclotron orbits, and a small fraction will collide with the hole edge and be lost.

In Appendix A, the number lost is estimated for the EV experiment. The calculation uses the assumptions that density is constant across the hole, and that r_c is much smaller than the collimator hole. The result is that the effective collimator area is changed by ΔA_h ;

$$\frac{\Delta A_h}{A_h} \approx 0.036 T_1^{1/2}, \quad (2.3)$$

so that at the typical temperature of 1 eV, 3%–4% of the electrons will be lost to the collimator hole edges, independent of B_z .

The number of electrons passing through the collimator hole is measured by the collector (Fig. 2.1). These electrons pass through the temperature analyzer, biased to +10 Volts, to the collector biased to +158 Volts, where they are absorbed. These electrons will result in an incremental change in the collector voltage V_r , where $Q(r) = C_r V_r$, with C_r being the capacitance of the collector and electronics. The value of C_r is known to $\sim 0.5\%$, and consequently the number of electrons

hitting the collector is known to $\sim 0.5\%$.

Amplifier noise contributes an uncertainty of about 10^4 electrons. For a typical plasma with $L_p \approx 30$ cm and $n \approx 10^7$, $Q \approx 2 \times 10^7$. Therefore, amplifier noise is about a 0.04% uncertainty in the density measurement.

2.4 Measurement of Total Number and Gauss's Law Measurement

In addition to $Q(r)$, the total number of electrons in the plasma, N_t , is measured. The electrons that do not go through the collimator hole strike the collimator plate, and produce a voltage change V_p . The collimator capacitance, C_p , is also known to $\sim 0.5\%$; so $N_t = (C_p V_p + C_r V_r)/(-e)$ is known to $\sim 0.5\%$.

The total number can also be obtained from integrating $Q(r)$:

$$N_{int} = \frac{1}{-eA_h} \int_0^{R_w} dr 2\pi r Q(r) \quad (2.4)$$

where R_w = radius of the conducting wall. I routinely compare measured N_t and N_{int} ; N_{int} is usually less than N_t by about 4% , presumably because of the effect described by Eq. 2.3. The simplest way to correct $Q(r)$ for this effect is to multiply $Q(r)$ by N_t/N_{int} : this has been done for the analysis of radial profiles presented in this thesis.

The basic assumption of our density measurement is that all the electrons that strike the collimator plate and collector are collected. I will call the percentage of electrons that are collected the 'collection efficiency': if all electrons that strike the collimator plate stay on the plate, then the plate has a collection efficiency of 100% . For the density measurement to be absolute, the collection efficiencies should be either calibrated or 100% .

There is a measurement that allows us to measure density without use of the collimator plate or collector. This measurement is based upon Gauss's Law.

Imagine a cylindrical Gaussian surface lying inside the conducting material of one of the containment cylinders. Assume that the cylinder is far enough from the plasma ends so that the electric field is radial inside and the contribution of the endcaps can be ignored. Gauss's Law states that the total enclosed charge is zero. The charge in the plasma is balanced by the absence of electrons on the wall. When the plasma is dumped, electrons must flow from outside the Gaussian cylinder to keep the net charge zero.

The interaction of the containment cylinder with the rest of the apparatus is approximated by a capacitor connected between ground and the cylinder. This capacitance comes from a combination of the capacitance of the lead connected to the cylinder and the distributed capacitance of the cylinder to ground. The charge flowing onto the cylinder will come from this capacitance and produce a voltage with respect to ground. From this voltage and the measured capacitance the original number can be measured (again, to $\sim 0.5\%$). I will call this the 'Gauss's Law Measurement.'

The number inside any part of the containment wall can also be calculated from the measured $Q(r)$ (corrected by multiplying by N_t/N_{int}) and $T(r)$ by integrating $n(r, z)$ obtained with the computer code described in the previous section. These two independent ways of obtaining the number inside a cylinder allow a consistency check: the two numbers are found to agree better than 1%. This gives confidence that the collection efficiencies are nearly 100%.

Note that for the Gauss's Law measurement to work correctly, the voltage of the cylinder must not rise enough to trap electrons inside. Typically, the voltage rises to a few millivolts, which is negligible compared to space charge voltage and temperature. This has been confirmed by comparing N_t measured with the Gauss's Law circuit in place with that measured when the Gauss's Law cylinder is

grounded: both measurements of N_t are the same within 0.1%.

To summarize: we measure both the total number N_t and the radial profile $Q(r)$. Measured $Q(r)$ is about 4% lower than that predicted by Eq. 2.1 because some electrons hit the edges of the collimator hole, and I typically correct for this by multiplying $Q(r)$ by N_t/N_{int} . Finally, the Gauss's Law measurement allows a consistency check, and gives confidence that absolute density measurements are good to about 1%.

2.5 Temperature Measurements

I measure the perpendicular temperature, T_{\perp} , by use of a 'beach analyzer' utilizing a secondary magnetic field. The analyzer consists of an analyzer solenoid enclosing an electrically separate cylindrical electrode located between the collimator and the collector. Essentially, the analyzer uses an electrostatic velocity analyzer to measure the change in the parallel energy of exiting electrons caused by the secondary magnetic field.

The temperature measurement begins when the dump cylinder potential is abruptly switched to ground. The plasma disassembles and the electrons form a beam with a parallel energy distribution determined by a combination of the parallel temperature and space charge energy. The perpendicular energy distribution, however, is the same as it was before the plasma was dumped. This is because the time for a gyro orbit (~ 1 nsec) is much less than the disassembly time ($\sim 1\mu\text{sec}$) or the collision time (~ 1 msec), and the gyromagnetic moment $\mu = mv_{\perp}^2/2B_z$ is conserved. Since B_z is fixed, v_{\perp}^2 remains unchanged and therefore the perpendicular energy distribution remains unchanged.

The electrons encounter the secondary magnetic field as the beam travels towards the collector. The distance an electron moves during a gyro orbit is small

compared to the distance over which the magnetic field changes. This implies that there are two quantities conserved by each electron in the exiting beam: the total energy $\frac{1}{2}m(v_{\perp}^2 + v_{\parallel}^2)$ and the magnetic moment, μ . In order to conserve both quantities the average parallel energy must change by $\Delta E_{\parallel} = -(\delta B_z/B_z)kT_{\perp}$ inside the analyzer solenoid. By measuring the difference in the parallel energy distribution on consecutive shots with δB_z at different values, the perpendicular energy distribution can be obtained. Note that one temperature measurement requires many shots and many inject, hold and dump cycles.

With this method, we routinely obtain T_{\perp} as a function of radius to a few percent accuracy. This technique is described more completely in separate publications [15,14].

2.6 Radial Density Profiles

Figure 2.2 is an example of a radial density profile. The two vertical dashed lines represent the location of the conducting wall. The solid line connects the average of the measurements of $Q(r)$ at each radius. For this particular profile there are eight shots taken at each radial point. The result of each shot is represented by a horizontal bar. The close vertical clustering of each group of eight bars is an indication of the reasonable degree of shot-to-shot repeatability. After each set of eight shots, the collimator is moved to a new location by a stepper motor. Included in Fig. 2.2 are six crosses which represent the results of the perpendicular temperature analysis at the radii indicated by the abscissa. The vertical extent of each cross is an indication of the uncertainty of the measurement.

On the left vertical dashed line in Fig. 2.2, is a small horizontal bar representing the results of the measurement of N_t . There are actually eight separate bars plotted for eight separate measurements. The measurement appears as one

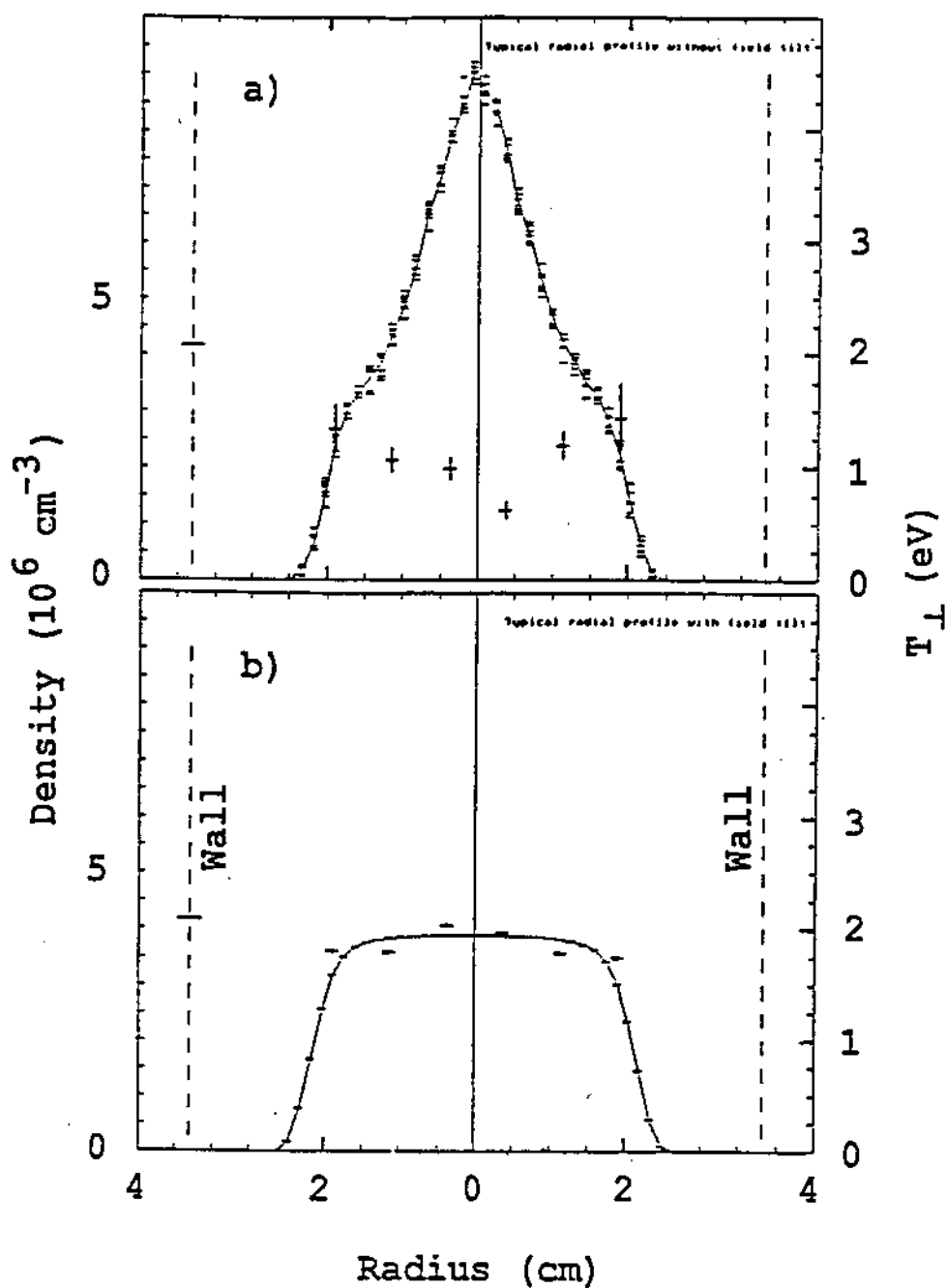


Figure 2.2: Typical radial density profile a) without field tilt, and b) same as a) except field was tilted by 6.2 mrad for 0.4 sec. For these profiles, there are eight density measurements at each radial location. Temperatures are the crosses, with the vertical extent an estimate of the error. These profiles were taken at $B_z = 188$ gauss.

bar because of the high degree of shot-to-shot repeatability.

The data of Fig. 2.2 was taken with a lab computer, a DEC LSI 11. The plot shown was made by the computer, which also stored the same information in a file. Both $Q(r)$ and N_t are converted into numbers of electrons using the amplifier gains and capacitances which are inputs into the computer program. In addition to density and temperature data, the file includes a record of various voltage and magnetic field settings for the radial profile. This file can be transferred to a larger VAX computer for more analysis. An example of such a post-processing program on the VAX is the calculation of $n(r, z)$ described previously.

The computer oriented approach is typical of much of the data taken on the EV machine. The design philosophy has been to always have manual electronics as an alternate, while developing computer software for very repetitive and tedious data taking, such as radial profiles. The use of the lab computer has made possible experiments that would have been very tedious before, such as radial temperature scans and the cross-sectional density plots described in Chapter 4.

2.7 Angular Momentum and Radial Losses

The angular momentum about the z axis, P_θ , is important for understanding radial confinement [20]. The total canonical angular momentum is the sum of a mechanical and an electromagnetic part. The mechanical part is much smaller (at least a factor of 100) in the experiments discussed here. Ignoring the mechanical angular momentum,

$$P_\theta = \left(\frac{eB_z}{2c} \right) \left[N_t R_w^2 - \sum_j r_j^2 \right], \quad (2.5)$$

which includes the contribution due to charges on the wall. Note that P_θ can be calculated directly from the experimentally measured $Q(r)$, without any need to know $n(r, z)$.

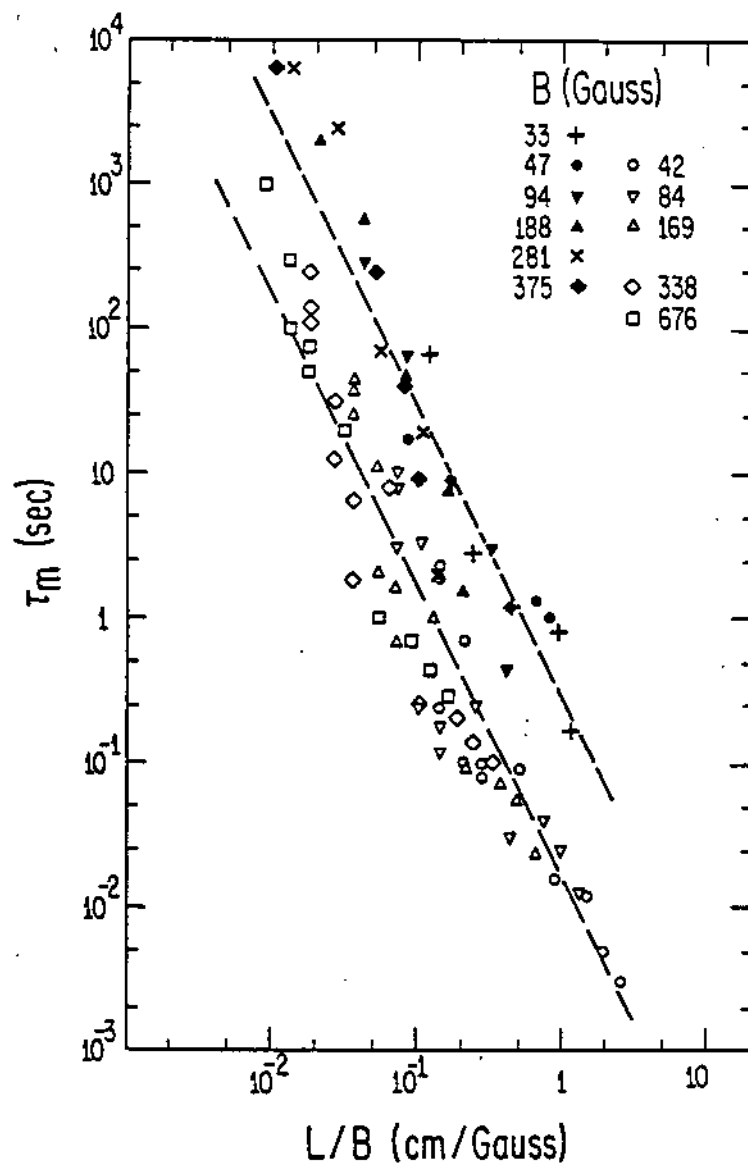


Figure 2.3: Measured evolution times τ_m versus plasma length L divided by magnetic field B for the new apparatus (solid symbols) and for the prior apparatus (hollow symbols). From Ref. [10].

If the system were azimuthally symmetric, then P_θ would be conserved. This implies a constraint on the allowed radial positions of the electrons, *i.e.* $\sum_j r_j^2 = \text{const.}$ If some electrons move out, then others must move in. This argument has been developed rigorously in a paper by O'Neil [21].

Contrary to this theory, the experiments have shown radial loss. This implies that there is an external coupling which applies a torque to the plasma. Examples of couplings that change P_θ are electron-neutral collisions, finite wall resistance, electromagnetic radiation, and deviations from cylindrical symmetry in the construction of the device. These external couplings are always present to some extent in experimental containment devices, although different effects dominate in different devices. This radial loss will be referred to as 'external transport'.

DeGrassie and Malmberg [8] investigated external transport in an early containment apparatus (the 'V' machine), which operated at neutral background pressures above 10^{-7} Torr. DeGrassie found that the transport rates scaled as P/B_z^2 , where P is the neutral pressure, and found good agreement with a theory by Douglas and O'Neil [9]. Later, Malmberg and Driscoll [19] measured the external transport rates on an ultra-high-vacuum apparatus ('V-prime') at low pressure; they found that the transport was dominated by a mechanism that was independent of P . This transport mechanism was termed 'anomalous'.

Driscoll and Malmberg [11] investigated the scaling of the anomalous transport rate by measuring the time, τ_m , for the central density to decrease by a factor of two as a function of B_z and L_p (plasma length). They found that τ_m scaled as $(L_p/B_z)^{-2}$ over five decades in (L_p/B_z) , with one decade of scatter. The results of this experiment on V-prime are the hollow symbols in Fig. 2.3.

Experimentation indicated that the most probable cause of the length-dependent anomalous losses is small electrostatic or magnetostatic field errors.

These small deviations from cylindrical symmetry can exert external torques on the plasma, and thereby cause radial transport.

The EV experiment was designed to minimize these asymmetries. The solid symbols in Fig. 2.3 are data from the EV experiment [10], and a best slope-2 logarithmic fit to the EV data gives

$$\tau_m = 0.32 \left(\frac{B_z}{L_p} \right)^2 \quad (2.6)$$

where L_p is in cm, B_z is in gauss and τ_m is in seconds. The containment times on EV are a factor of 20 longer than in the prior experiment.

2.8 Magnetic Alignment and Tilt

In addition to the main solenoid, EV has external field coils that produce magnetic fields perpendicular to B_z . The purpose of these coils is to align the magnetic axis with the axis of the containment cylinders. This alignment has a strong effect on the evolution of the plasma. The alignment is performed by maximizing the central density left after a chosen containment time t_d , $Q(r=0, t_d)$.

The external alignment coils create secondary B fields in the \hat{x} or \hat{y} directions: a uniform field B_x effectively tilts the main field B_z by the angle $\theta_x = B_x/B_z$. Figure 2.4 plots central density $Q(0, t_d)$ versus θ_x at $B_z = 94$ gauss. It is seen that $Q(0, t_d)$ is a sharp function of the axis alignment, with a misalignment of 10^{-4} radians being significant. In this graph, B_y has already been set so that $Q(0, t_d)$ is a maximum.

For most of the data presented in this thesis, the magnetic field is intentionally tilted for a period of time after injection. I perform the injection process with the field aligned and then change the current in the B_x or B_y field coil. This change in the magnetic field takes about 100 msec to penetrate the conducting cylinders into the plasma, since eddy currents in the wall last this length of time.

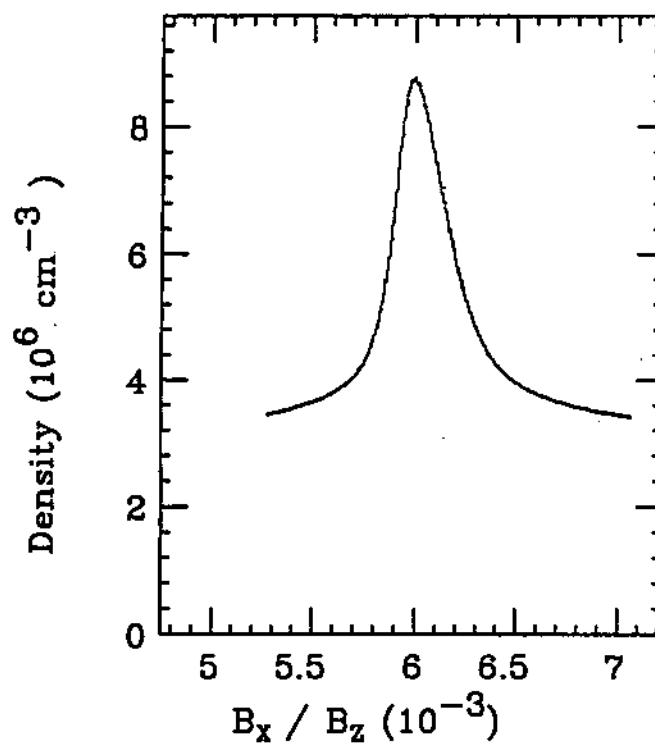


Figure 2.4: Central density at time t_d versus magnetic tilt angle.

I leave the field tilted for a time on the order of 1 second, then reset the B_x or B_y field back to the aligned value. After waiting longer than 100 msec for the fields to again penetrate the conducting wall, the experiment can be continued.

The field tilt has a dramatic effect upon the radial profile. Figure 2.2b is a radial profile taken after the profile of Fig. 2.2a. The number of averages, the amplifier gains, the dump time (0.7 sec); all parameters are the same as in Fig. 2.2a, except that the field was tilted by 6.2×10^{-3} radian for 0.4 seconds. The field tilt was then turned off 200 msec before the plasma was dumped.

Note that after the field tilt, both the plasma density and temperature have very flat profiles. The noise in both $Q(r)$ and $T(r)$ is also much smaller than in Fig. 2.2. The total number of electrons is the same in both cases, with the tilted profile being slightly expanded in the radial direction. The flattening of the profile and decrease of the shot to shot noise seems to be a general characteristic of the tilt effect.

Such a tilt-quieted profile has two important advantages: fewer shots need be averaged for the same statistical accuracy, and the profile is a good approximation to the ubiquitous 'square profile' of theory. These advantages are so important that the tilting procedure is almost always used for EV experiments.

Chapter 3

Measurement and Manipulation of the Diocotron Mode

3.1 Overview

This chapter will introduce the $k_z \approx 0$, azimuthal mode number $l = 1$ diocotron mode and the experimental techniques used to manipulate this mode. The word 'diocotron' refers to modes with potential variations $\delta\phi \sim e^{(il\theta - k_z z)}$, and often means the $k_z \approx 0$ modes in particular. The $l = 1$, $k_z \approx 0$ diocotron mode is unique in that it is very stable. In this thesis the term 'diocotron mode' will be used as short for ' $l = 1$, $k_z \approx 0$ diocotron mode'.

The diocotron mode can be pictured as a displacement by a distance D of the plasma column from the axis of the conducting wall. The method of images can be used to calculate the electric field: the conducting wall is replaced by an infinitely thin line of charge that is opposite in charge from the plasma and located at a radius of R_w^2/D . The diocotron mode is essentially the motion of the column around the wall axis due to $\mathbf{E} \times \mathbf{B}$ drift in the field of the image charge.

The diocotron mode can be manipulated and measured with the use of 'sector probes'. Sector probes are electrically isolated conducting wall patches. As the plasma column moves in θ , image charges move on and off of the sector probes. If a resistor (usually 50Ω) is connected from the sector probe to ground,

a fluctuating voltage will develop across the resistor due to the diocotron motion. I have found that this signal consists of a fundamental oscillation at the diocotron frequency plus oscillations at the harmonics of this frequency. The displacement can be measured by taking a phase-locked density profile, and using this measure of D I have found that the amplitude of the fundamental increases as D , and that the amplitude of the first harmonic increases as D^2 . These results agree with a theory by Kapetanacos and Trivelpiece [17], once an algebraic error in the theory (the right hand side of Eq. 22 in Ref. [17] should be multiplied by two) is corrected.

Growth of the diocotron mode can be induced by a resistor attached to a sector probe. This effect has been investigated by White, Malmberg and Driscoll [31]. They derive an expression for the growth rate by relating the energy in the wave to the power lost in the resistor. The small resistance in the wall and sector probe leads will cause a background growth of the mode: I estimate this to be about 0.05 dB/sec, which is generally negligible on the one to ten second timescale of the experiments described here.

Alternately, growth or damping of the diocotron mode can be induced using an active feedback loop instead of a passive resistor. The feedback loop can be set up by phase-shifting and amplifying the signal from a 'receiver' sector probe and applying this voltage to a 'transmitter' sector probe [30]. This feedback causes the diocotron mode to grow or damp exponentially, depending upon the amount of phase shift. Using feedback, the diocotron mode can be grown to large amplitudes and then damped with negligible change in the radial profile. I have measured the feedback growth rate and find that it increases linearly with the amplifier gain and varies as the sine of the phase shift. These measurements agree with a simple calculation which is also presented.

3.2 The Image Charge Model of the Diocotron Mode

The diocotron mode can be pictured as a displacement by distance D of the plasma column from the axis of the conducting wall. This simple interpretation of the diocotron mode leads to an analysis using the method of images. Figure 3.1a depicts a cross-section of a line charge with charge per length $-N_L e$ displaced a distance D from the axis of a conducting cylinder.

It is easily shown (Appendix B) that the boundary condition $\phi(R_w, \theta) = 0$ is met by replacing the conducting wall with a line charge with charge per length $+N_L e$ located at the radius

$$S = \frac{R_w^2}{D}. \quad (3.1)$$

From the method of images it is clear that the two line charge system has exactly the same electric field inside $r = R_w$ as the line charge and conducting wall system.

The method of images can also be used to solve for the electric field of a plasma column of radius R_p . Assume that the plasma is cylindrically symmetric about an axis displaced by D , as depicted in Fig. 3.1b. Assume also that this plasma has the same N_L as the line charge in Fig. 3.1a. Imagine for a moment that the conducting walls are removed in Fig. 3.1. From Gauss' Law, the electric field from the plasma in Fig. 3.1b is the same as the field due to the line charge in Fig. 3.1a for points outside the plasma. In particular the electric field at the location of the conducting walls is the same. Therefore, if the walls are replaced, the image charges will be the same. It can be concluded that the positive image charge used with the line charge also works with the plasma, as long as the plasma is cylindrically symmetric about its axis.

The physics of the diocotron mode becomes clear from the image charge model. If $D/R_w \ll 1$ then the image charge is far away and the image electric field

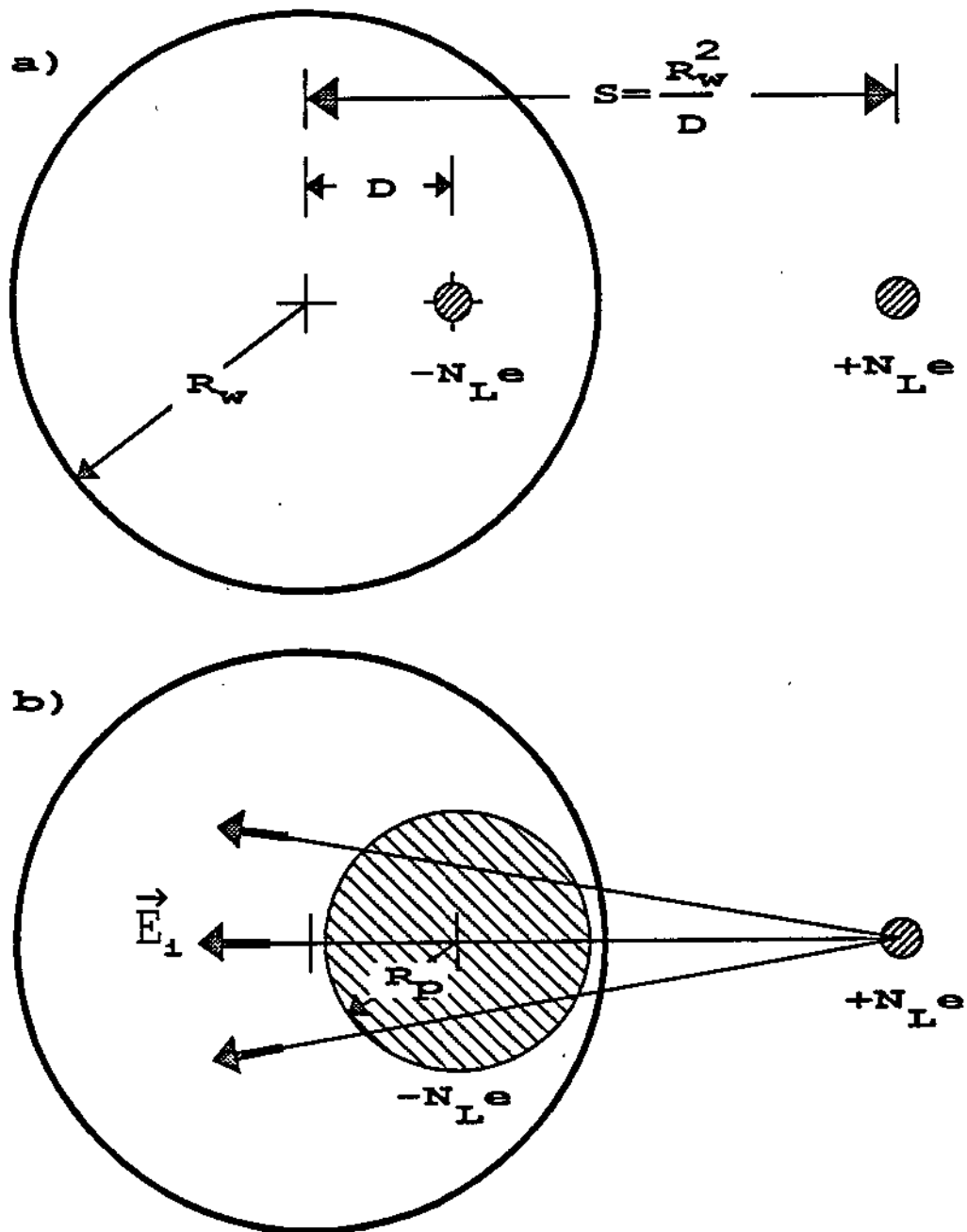


Figure 3.1: Image charge model of the diocotron wave for a) charged, infinitely thin line charge offset by D ; b) a plasma column of radius R_p , cylindrically symmetric about an axis offset by D .

is approximately constant across the plasma. This results in an $\mathbf{E} \times \mathbf{B}$ drift which is the same for every part of the plasma. This drift causes the plasma to revolve around the conducting cylinder axis. At the same time the plasma rotates about its own axis due to its self-field. To the extent the image field is constant over the plasma, this rotation is not perturbed by the image field and the plasma remains cylindrically symmetric, consistent with the model.

Several results can be immediately obtained from the model; first the frequency of revolution will be calculated. The field from a line charge is given by

$$E = \frac{N_L e}{2\pi\epsilon_0 r} \quad (3.2)$$

Assuming $D/R_w \ll 1$, and using the image electric field E_i at the center of the conducting cylinders, the $\mathbf{E} \times \mathbf{B}$ drift velocity is

$$v_d = \frac{E_i}{B} = \frac{N_L e D}{2\pi\epsilon_0 B_z R_w^2}, \quad (3.3)$$

from which the frequency of revolution is calculated to be

$$\omega_d = \frac{N_L e}{2\pi\epsilon_0 B_z R_w^2} \quad (3.4)$$

Equation 3.4 is identical to the result derived in the standard linear theory of diocotron modes [18]. (An excellent bibliography of previous work on diocotron modes can be found in Davidson [7].) The beauty of the image charge model is that this result can be derived easily.

The diocotron mode energy, W , is negative. Since the image charge is opposite in sign from the plasma charge, the electrostatic energy is lowered as the plasma is moved closer to its image, or as D increases. If part of the conducting wall is made resistive, the wave will be destabilized and grow exponentially. It is straightforward to derive an expression for W . The energy is the work needed to move the plasma off center a distance D in the image electric field. The work

needed to displace a section of plasma of length L_p is

$$W = \int_0^D F dx = \int_0^D -(N_L e L_p) \frac{N_L e}{2\pi\epsilon_0 R_w^2} x dx = -\frac{(eN_L)^2}{4\pi\epsilon_0} \left(\frac{D}{R_w}\right)^2 L_p. \quad (3.5)$$

This expression will be used to derive the growth rates due to both feedback and the resistive wall effect.

The fact that the diocotron mode is stable, and the simple picture of it as an orbit of the plasma around the center of the conducting cylinders, lead me to call it a *dynamical equilibrium*.

There is a difference between the image charge model and the standard linear diocotron theory which should be pointed out. Linear diocotron theory requires that both D/R_p and D/R_w be small, while the image charge model only requires that D/R_w be small. The behavior of the diocotron mode with $D/R_w \sim 1$ will be discussed in Chapter 4.

3.3 The Signal on a Sector Probe from a Diocotron Mode

One of the EV cylindrical sections is divided azimuthally into four 60° electrically isolated patches whose centers are separated azimuthally by 90° . These patches are known as *sector probes*. The sector probes capacitively couple to diocotron modes in the plasma, and are used to detect and manipulate the diocotron mode in the experiments described here. The topic of this section is the signal that can be expected on a sector probe when an diocotron mode is in the plasma.

The image charge model can be used to calculate the signal from the diocotron mode, assuming that the plasma is cylindrically symmetric about its axis. The electric field at the wall, $E(R_w)$, can be calculated by adding the fields of the plasma and the image, and the charge density at the conducting wall is $\epsilon_0 E(R_w)$. The total charge on a sector probe can be found by integrating the charge den-

sity over the probe. This problem is analyzed in more generality in a paper by Kapetanakos and Trivelpiece [17]. They find that the current induced by an orbiting line charge is

$$i_s = - \left(\frac{2\omega N_L e L_s}{\pi} \right) \sum_{n=1}^{\infty} \sin \left(\frac{n\Delta\theta}{2} \right) \sin(n\omega t - \theta_s) \left(\frac{D}{R_w} \right)^n, \quad (3.6)$$

where $L_s \equiv$ length of sector probe, $\Delta\theta \equiv$ angular width of sector probe, and $\theta_s \equiv$ angular position of the sector probe center. (Note that the right hand side of Eq. 22 in Ref. [17] should be multiplied by two.)

I performed an experiment to test Eq. 3.6. The quantities L_s , $\Delta\theta$ and R_w are known physical dimensions. The frequency, ω , was measured with a spectrum analyzer. The line density, N_L , was calculated from the measured radial profile using the computer solution of $n(r, z)$ (see Section 2.6). The sector probe current was measured by connecting the sector probe to a known resistor and measuring the voltage amplitude with a spectrum analyzer.

The displacement was measured with the density diagnostic. This technique will be described in Section 4.2, and consists of making a cross-sectional plot $n(r, \theta)$ from density measurements compiled over many shots. The displacement, D , is defined to be the distance from the center of mass of $n(r, \theta)$ to the conducting wall axis.

If the coefficient in front of Eq. 3.6 is constant with D , then Eq. 3.6 predicts that the signal from the fundamental ($n = 1$) will increase linearly with D , and the signal from the first harmonic ($n = 2$) should increase as D^2 . This simple behavior is complicated by the fact that ω and N_L , which appear in the coefficient, vary somewhat with amplitude. If all measured amplitudes are multiplied by $N_L\omega/N_{L0}\omega_0$, where N_{L0} and ω_0 are measured at the smallest amplitude, then this variation is corrected. (The correction is at most 20%).

The results of this experiment are shown in Fig. 3.2, where the measured i_s

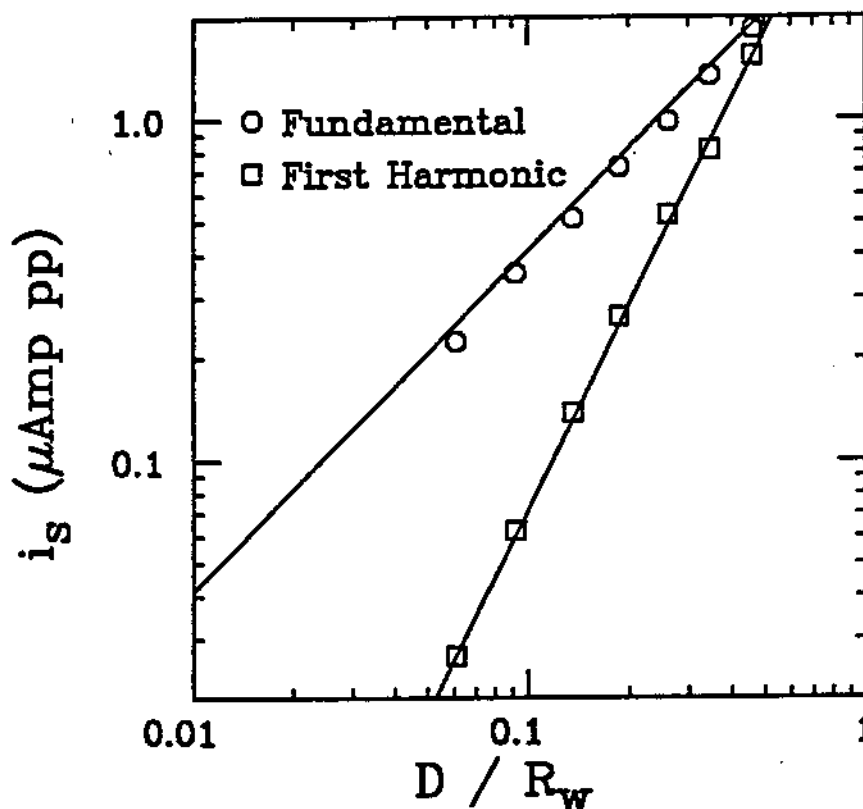


Figure 3.2: Measured sector probe current, i_s , as a function of diocotron displacement, D . The fundamental and first harmonic are shown and compared to theory (solid lines).

(multiplied by $N_{L\omega}/N_{L0\omega_0}$) at both the fundamental and first harmonic frequencies is plotted versus D/R_w . The predictions of Eq. 3.6 are represented by the solid lines. It is seen that there is agreement within the accuracy of the measurement.

One caveat is that the diocotron mode is not only an orbit of the plasma but also includes a distortion of the profile at large amplitudes. The amplitudes in Fig. 3.2 are large, and some distortion could be expected. However, a narrow radius plasma was used, and it will be shown in Chapter 4 that the distortion is minimized for a narrow radius plasma.

3.4 Resistive Growth of the Diocotron Mode

The $l = 1$ diocotron mode can be exponentially grown by attaching a resistor to a sector probe. As was previously mentioned, the diocotron mode is a negative energy mode, so that it is grown by removing energy from the plasma. This effect was experimentally investigated by White, Malmberg and Driscoll [31], and good agreement was found with the formula

$$\gamma_{res} = \left(\frac{4\epsilon_0}{\pi} \right) \frac{L_s^2 \sin^2(\Delta\theta/2)}{L_p} \left[\frac{R_s}{1 + (\omega R_s C_s)^2} \right] \omega^2, \quad (3.7)$$

where $\gamma_{res} \equiv$ growth rate in sec^{-1} , $R_s \equiv$ resistor attached to sector probe, $C_s \equiv$ capacitance of sector probe, $\omega \equiv$ diocotron frequency.

Equation 3.7 can be derived by equating the time rate of change of the energy of the mode, W , to the power absorbed in the resistor. Eq. 3.7 results if the expression for W from the image charge model (Eq. 3.5) is used along with the fundamental component of the sector probe current in Eq. 3.6. Since the image charge model is two-dimensional, Eq. 3.7 does not include end effects. Eq. 3.7 also does not include the effect of the higher harmonics of the signal, and the effect of large amplitude density distortions. I have not studied these corrections.

A resistor is attached to a sector probe in order to observe the diocotron mode. This means that the process of detecting the diocotron mode will itself result in a small growth rate. The detection resistor is normally 50Ω , which with $C_s \approx 500\text{pF}$, a typical frequency of 10^5 Hz , and a plasma length $L_p = 28\text{cm}$ gives a growth rate of 3 dB/second.

Even with all of the sectors grounded, there is a small resistance due to the resistances of the cables attached to the sectors. The ground connection is made at the end of each cable, so that each sector has a resistance of 0.2Ω attached to it. For the same conditions as in the previous paragraph, Eq. 3.7 predicts a growth

rate of 0.05 dB/sec due to all four sectors.

There is also a small growth rate induced by the finite wall resistance. This growth rate can be estimated by approximating the wall as two 180° sector probes, each with resistance

$$R_s = \rho \times \frac{\pi R_w}{L_p \times \delta}, \quad (3.8)$$

where $\rho \equiv$ resistivity of wall material, $\delta \equiv$ skin depth. Using Eq. 3.8 in Eq. 3.7 and noting that $\omega R_s C_s \ll 1$, the growth rate due to the finite wall resistance is

$$\gamma_{wall} = 32\pi^2 \epsilon_0 R_w f^2 \sqrt{\pi \mu_0 f \rho}. \quad (3.9)$$

Equation 3.8 can be derived more rigorously using a technique described in Jackson [16, Section 8.1] (also see [1]). The result is identical to Eq. 3.9.

Taking $\rho = 1.74 \times 10^{-8} \Omega\text{-m}$ (Copper), Eq. 3.9 becomes

$$\gamma_{wall} = (0.077 \text{ dB/sec}) \left(\frac{R_w}{3.81 \text{ cm}} \right) \left(\frac{f}{100 \text{ kHz}} \right)^{2.5}, \quad (3.10)$$

so that for a typical case with $f = 100 \text{ kHz}$ we obtain $\gamma_{wall} = 0.077 \text{ dB/sec}$. Combining the growth due to finite wall resistance and sector probe cables for the case $L_p = 28 \text{ cm}$, $\gamma_{wall} = 0.13 \text{ dB/sec}$.

In summary, a resistor attached to a sector probe will cause an exponential growth of the $l = 1$ diocotron mode. This means that the process of detecting the mode will necessarily induce a small growth while the detection resistor is connected to the sector probe. The finite resistance of the wall and the sector probe cable resistance also cause a small growth.

3.5 Feedback Growth and Damping

The diocotron mode can be accurately and repeatably grown or damped using feedback to an amplitude chosen by the experimenter. Figure 3.3 is an

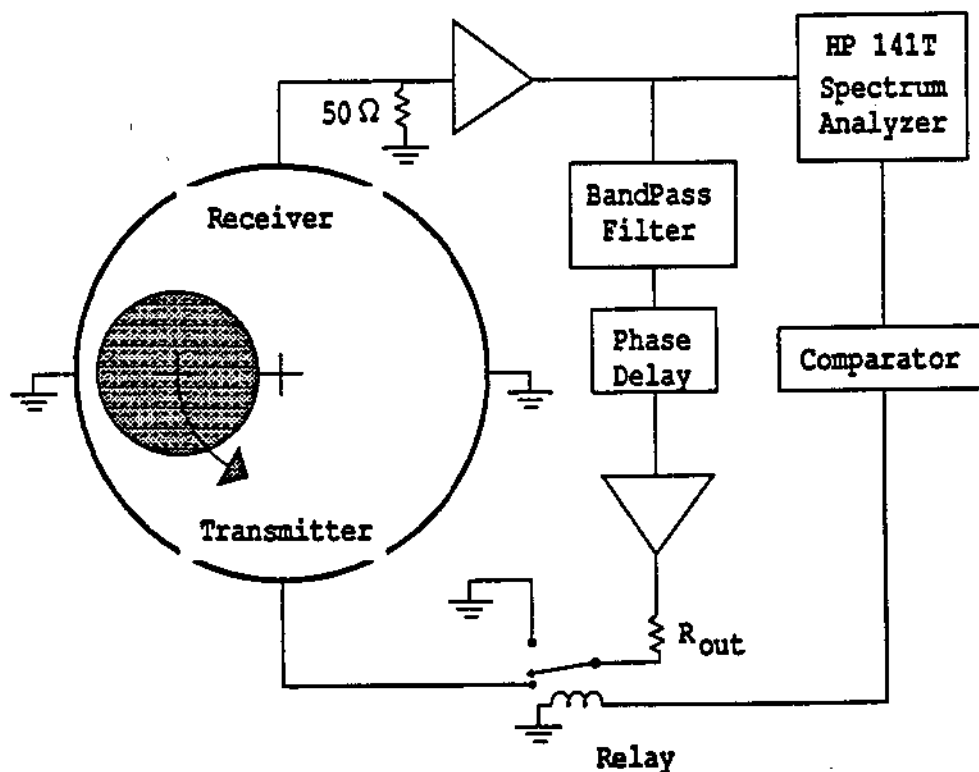


Figure 3.3: Feedback circuit.

example of the circuit used for feedback. I have previously mentioned that the EV experiment has four sector probes with centers spaced at 90° intervals. In Fig. 3.3 two of these probes have been grounded and one is labeled receiver and the other transmitter.

The receiver probe is operated with the sector probe connected to a pre-amplifier with a $50\ \Omega$ input impedance. The signal then passes through a bandpass filter that is set to a frequency near the diocotron frequency. The signal then passes through a variable phase shifter, is amplified some more, and is then delivered to the transmitter probe. A spectrum analyzer is also attached to the output of the preamp, and produces a voltage proportional to the log of the wave amplitude. This can be used with a comparator and relay to halt the feedback growth or

damping at an amplitude chosen by setting the comparator.

Since the feedback technique is fundamental to the experiments presented here, I will outline a derivation of feedback growth rates. The feedback technique has been previously analyzed by Warren White [30]; here I present a different derivation.

First, some definitions:

- $G \equiv$ gain of feedback circuit
- $\phi \equiv$ phase shift of feedback circuit
- $L_r, L_t \equiv$ length of receiver/transmitter probe
- $\theta_{rt} \equiv$ angular displacement between probe centers
- $\theta_r, \theta_t \equiv$ angular positions of probe centers
- $\delta\theta_r, \delta\theta_t \equiv$ angular width of receiver/transmitter probe
- $R_{in}, R_{out} \equiv$ input/output resistance of feedback circuit
- $C_{out} \equiv$ capacitance of transmitter probe plus circuit

The resistors attached to the probes will cause a growth rate that can be estimated using the formulas in the previous section, and will be ignored here. The feedback growth is due solely to the interaction of the transmitter probe and the plasma. The current and voltage of the transmitter probe consists of two parts:

$$i = i_f + i_p, \quad (3.11)$$

$$v = v_f + v_p, \quad (3.12)$$

where i_f, v_f are due to the feedback circuit and i_p, v_p are induced by the plasma.

The power from the transmitter to the plasma is given by

$$\Delta P \approx i_p v_f + i_f v_p. \quad (3.13)$$

From Eq. 3.6, using only the $n = 1$ term, i_p and v_f are found to be

$$i_p = -\frac{2\omega N_L e L_t}{\pi} \sin \frac{\delta\theta_t}{2} \sin(\theta_t - \omega t) \frac{D}{R_w}, \quad (3.14)$$

$$v_f = -\frac{2\omega N_L e L_r}{\pi} \sin \frac{\delta\theta_r}{2} G R_{in} \sin(\theta_r + \phi - \omega t) \frac{D}{R_w}. \quad (3.15)$$

Circuit theory can be used to obtain i_f and v_p in terms of i_p and v_f :

$$i_f = \frac{dQ_f}{dt} = C_{out} \frac{dv_f}{dt}, \quad (3.16)$$

$$v_p = i_p R_{out}. \quad (3.17)$$

Combining Eqs. 3.13 through 3.17, the power ΔP can be calculated. Averaging over time, the average power $\overline{\Delta P}$ is found to be

$$\begin{aligned} \overline{\Delta P} = & \frac{2\omega^2 N_L^2 e^2}{\pi^2} G R_{in} L_r L_t \sin \frac{\delta\theta_r}{2} \sin \frac{\delta\theta_t}{2} \frac{D^2}{R_w^2} \\ & \times \{ \cos(\theta_{rt} + \phi) - \omega C_{out} R_{out} \sin(\theta_{rt} + \phi) \}, \end{aligned} \quad (3.18)$$

This power comes from the decrease in energy of the plasma as the diocotron mode grows.

The mode energy is given by Eq. 3.5. This expression was calculated from an infinite length model, and is an approximation that ignores finite length end effects. Setting $dW/dt = \overline{\Delta P}$, we find that D grows exponentially at a rate

$$\begin{aligned} \gamma_{fb} = & \frac{4\epsilon_0}{\pi} G \omega^2 R_{in} \frac{L_r L_t}{L_p} \sin \frac{\delta\theta_r}{2} \sin \frac{\delta\theta_t}{2} \\ & \times \{ \cos(\theta_{rt} + \phi) - \omega C_{out} R_{out} \sin(\theta_{rt} + \phi) \}. \end{aligned} \quad (3.19)$$

For the experiments here, the second term in brackets is much smaller than the first, and is ignored in what follows.

I have experimentally tested Eq. 3.19 by measuring the growth rates with a spectrum analyzer as a function of G and ϕ . Fig. 3.4 displays measured growth rate versus ϕ for $\phi_{rt} = 90^\circ$. Solid lines are the predictions of Eq. 3.19. Figure 3.5

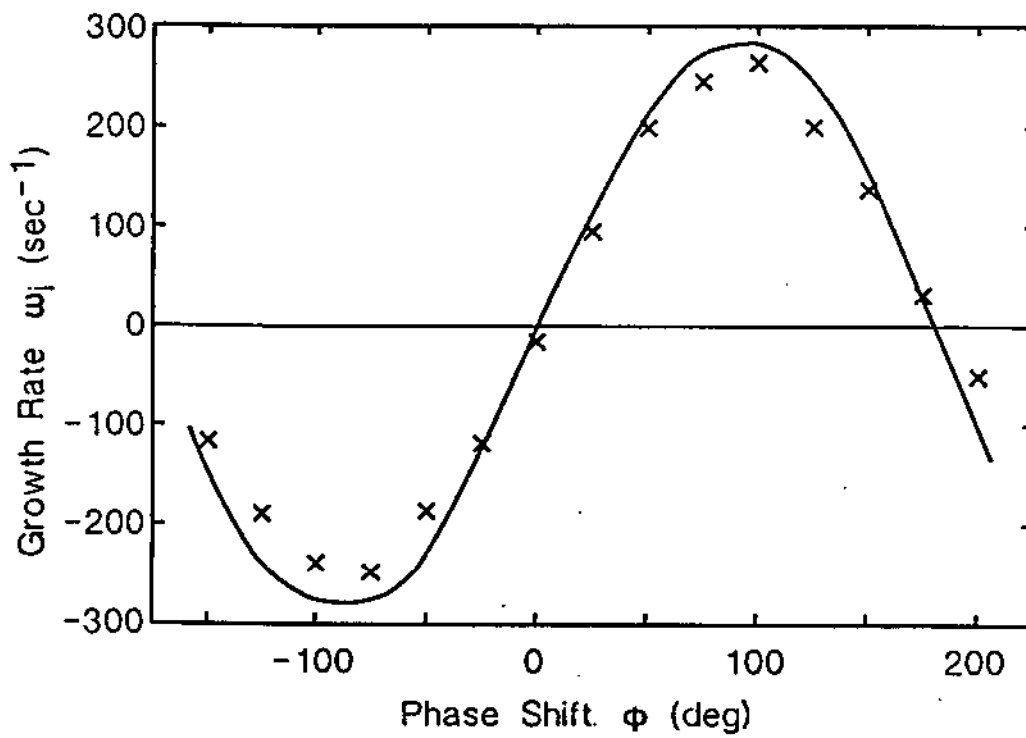


Figure 3.4: Feedback growth rate versus phase shift.

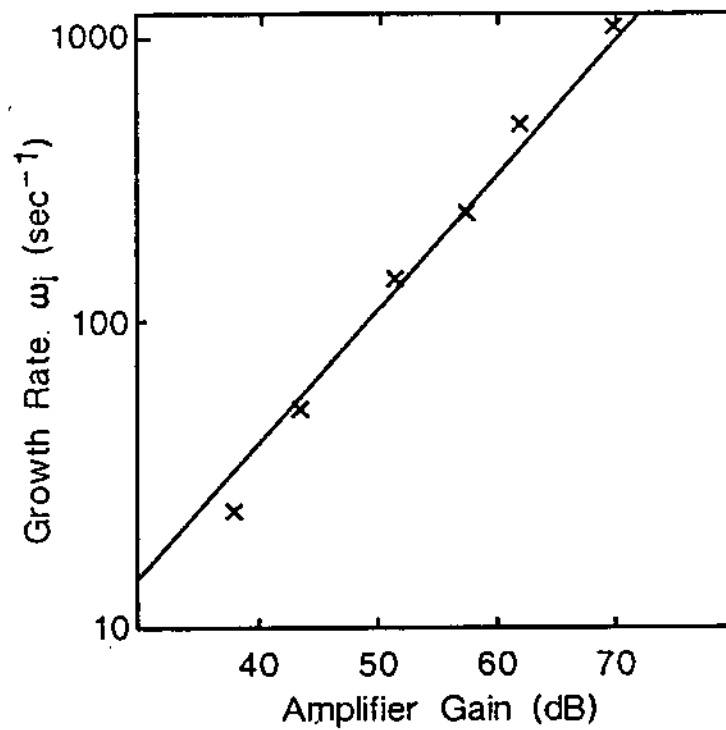


Figure 3.5: Feedback growth rate versus amplifier gain.

displays growth rate versus amplifier gain. Again, the solid line is the prediction of Eq. 3.19. The agreement between theory and experiment is reasonable in light of the few percent corrections expected from the finite length effect (Chapter 5). For perspective, the growth rate due to the resistive wall effect is predicted by Eq. 3.7 to be $\gamma_{res} \approx 0.07\text{sec}^{-1}$.

Chapter 4

The Large Amplitude Diocotron Mode

4.1 Overview

The topic of this chapter is the behavior of the $l = 1$, $k_z \approx 0$ diocotron mode at large amplitudes. This behavior is particularly striking: the mode is best described as a stable nonlinear dynamical state rather than as a perturbation of the type treated by linear theory. The dynamical state is that of a displaced and slightly distorted plasma column $\mathbf{E} \times \mathbf{B}$ drifting around the axis of the containment cylinders. In the frame rotating at the mode frequency the density is stationary, implying that the density and potential contours coincide. The small distortion of the plasma column needed to meet this condition causes some of the observed nonlinear effects.

In contrast, linear theory treats the mode as perturbation charges on the edge of the column. These theory perturbations are approximately $\delta n = D(\partial n_0 / \partial r)$: they 'model' a uniform displacement, D , of the plasma column. The linear theory appears nonlinear for displacements which are small compared to the radius of the column, even though the mode may still be basically linear.

I have measured the displacement of the plasma column, the distortion of the plasma column, and the shift of the mode frequency as the mode is excited

to large amplitudes. At finite displacements, the cross-section of the column is observed to become approximately elliptical (elongated in the θ -direction). This is a good characterization of the distortions up to amplitudes at which the plasma is essentially scraping the cylindrical wall. Indeed, one open question is why this mode is stable and essentially undamped at such extreme amplitudes.

At large amplitudes, the measured mode frequency shifts by as much as 20% (generally upward). This frequency shift can be understood best in terms of simple dynamical models: a 'rod' model predicts an upward shift proportional to D^2 ; and fields due to the observed elliptical distortions produce a downward shift, which for small D is proportional to $D^2 R_p^6$. Together, these two effects give excellent agreement with the experiment.

In order to calculate the stationary state of the plasma column, I have developed a computer code that models the plasma as a uniform density 'waterbag' column. The calculated distortions and frequency shifts are in excellent agreement with experiments for all mode amplitudes and plasma radii.

Finally, I compare a theory calculation of the frequency shifts by Prasad and Malmberg [24] to my experimental results. These predictions are a fair approximation at small amplitudes, but disagree for $D/R_w > 0.1$. This discrepancy at such low wave amplitudes is probably because the density perturbations are calculated with respect to the center of the cylindrical wall instead of the center of the plasma column: large perturbations are required to model the zero-order displacement of the column, making the perturbation series suspect.

4.2 Phase-Locked Density Measurements

4.2.1 Experimental Setup

The experiments discussed in this chapter begin with a period of magnetic tilt followed by feedback growth. The magnetic field tilt is used to generate square, low noise profiles as discussed in Section 2.8. The profiles have approximately constant density inside with a sharp edge (see Fig. 2.2b, page 17). I define the plasma radius, R_p , to be the radius at which density drops to half of the central density. The value of R_p can be varied by changing the bias across the spiral filament and the length of time the field is tilted. Plasma radii between $0.35 < R_p/R_w < 0.75$ have been generated by this procedure.

After the field tilt has been turned off and the field is again aligned, the diocotron mode is initiated by a burst at the mode frequency on the transmitter probe from an oscillator (Fig. 2.1, page 10). The growth of the diocotron mode is monitored by a spectrum analyzer attached to the receiver probe output. The spectrum analyzer frequency is fixed, and the device operates as a tuneable receiver with variable bandwidth. The output of the spectrum analyzer is proportional to the log of the input amplitude, and this output is used with a comparator that turns off the feedback when the amplitude reaches a preset value. This technique is used to grow the diocotron mode to the same amplitude on every shot.

A cross-sectional density plot of a plasma supporting a large amplitude diocotron wave can be generated by phase-locking the dump time to the wave phase. The phase of the fundamental component of the signal on the sector probe is the same as the angle of the plasma with respect to the sector probe, as shown in Eq. 3.6. If the value of this angle at dump time is varied, then a plot of density versus angle can be made from data taken on consecutive shots.

This synchronization to the sector probe signal is provided by a comparator

triggered by a positive-going zero crossing of the signal on the receiver probe. The comparator starts a timer that delays for a time set by the lab computer. The timer generates a dump trigger at the end of this time and the density is measured. The phase angle of the wave is calculated from the timer value and the measured frequency. The timer is incremented on consecutive shots in precise steps until a plot of density versus angle is generated. The radial position of the collimator is then changed, and the process repeated until a full cross-sectional density plot $n(r, \theta)$ is generated.

Figure 4.1 shows two typical examples of such plots. Density is measured on a grid shown by the small black dots. The density is linearly interpolated between points, and the grey level at each pixel is assigned according to a four level map. Contours appear as boundaries between regions of different grey levels. The data shown in Fig. 4.1 was not averaged: only one shot was taken per point. The smooth shape of the contours is an indication of the shot-to-shot repeatability of the plasma.

The time for the electrons to leave the system axially during the dump must be small compared to the diocotron period, or 'smearing' of the density plots will occur. A dump circuit was designed to switch from the negative containment voltage to ground in $\sim 0.3 \mu\text{sec}$. With this fast dump circuit in operation, the longest time for the electrons to leave axially is observed to be $\sim 1 \mu\text{sec}$. For a typical frequency of 50 kHz, this would predict a motion through 10° during the dumping process in the worst case. The smearing was investigated experimentally by taking a series of $n(r, \theta)$ plots as the dump circuit was slowed down: for slow dump times these plots show a distinctive distortion (a dip in the outer part of the profile) that disappeared at the fastest dump times. I believe that the effect of smearing is negligible in the data presented in this chapter. (An example of the

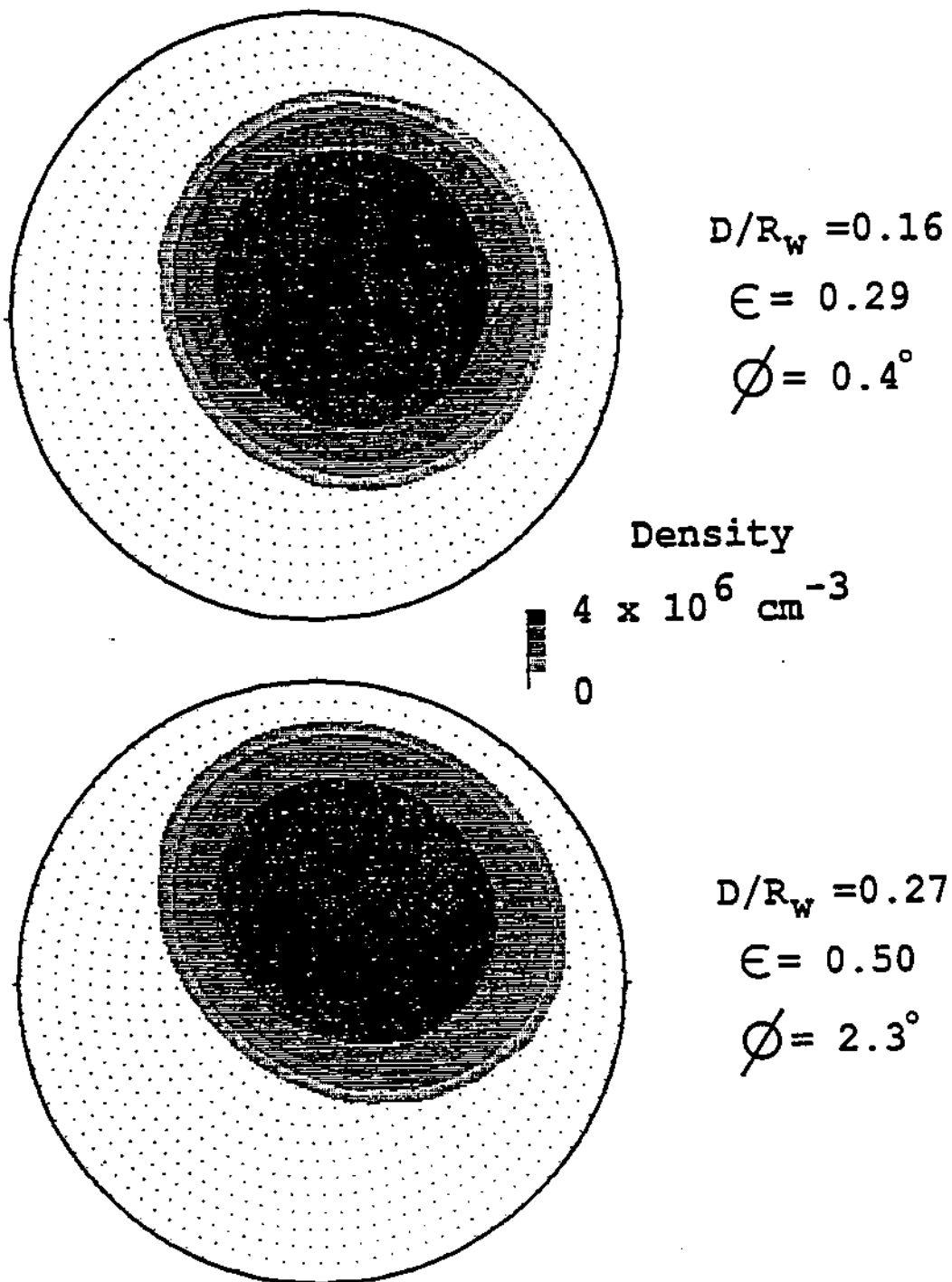


Figure 4.1: Measured phase-locked densities $n(r, \theta)$ for the diocotron mode at two amplitudes, showing elliptical distortion. For both cases, $R_p = 2.42$ cm, and the outer circle is at $R_w = 3.81$ cm.

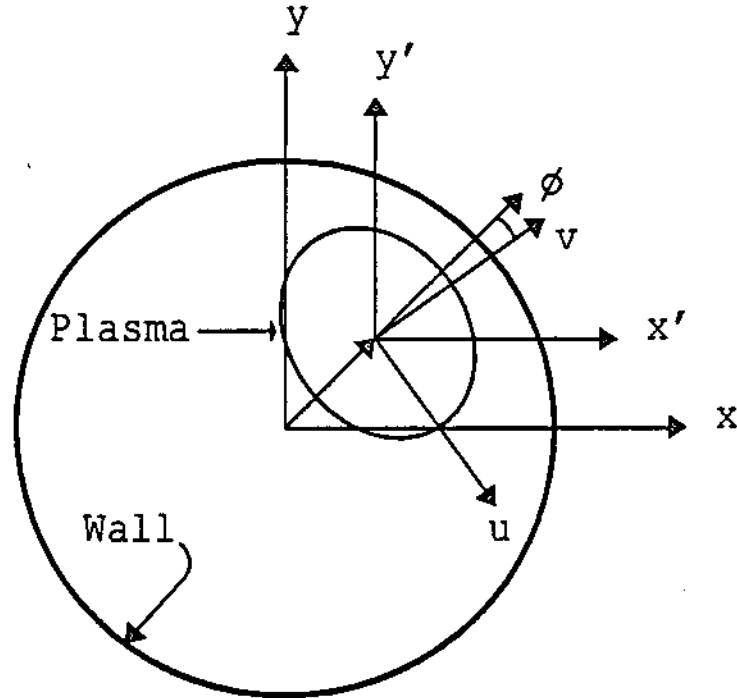


Figure 4.2: Coordinates used in the calculation of the eccentricity, ϵ , from the measured plasma density.

effect of smearing can be seen, however, in the visible asymmetry of the 'before damping' curve of Fig. 6.5, page 87).

4.2.2 Distortion of Plasma Shape

I define the wave displacement to be the distance, D , between the wall axis and the center of mass of the measured densities. The two plasmas shown in Fig. 4.1 have the same parameters, except for different values of D . It can be seen that the plasma column distorts from a circular shape on axis to an approximately elliptical shape with elongation in the θ -direction. This elliptical distortion has been seen in all the phase-locked plots I have taken at large D , and the distortion increases with D . At the very largest displacements (plasma edge at the wall), the inside edge of the plasma has been observed to curve outwards towards the wall,

so that the plasma assumes a 'kidney-bean' shape.

I characterize the plasma distortion by the eccentricity, ϵ , of the plasma shape. The eccentricity is calculated from moments of the measured $n(r, \theta)$. These moments are calculated using the coordinates illustrated in Fig. 4.2. Define the moments of density in the (x, y) coordinate system centered on the conducting wall with

$$I_{xx} \equiv \frac{1}{M} \int n x^2 dA, \quad (4.1)$$

$$I_{yy} \equiv \frac{1}{M} \int n y^2 dA, \quad (4.2)$$

$$I_{xy} \equiv \frac{1}{M} \int n xy dA, \quad (4.3)$$

where

$$M \equiv \int n dA \quad (4.4)$$

and $dA \equiv dx dy$.

These moments are transformed to a coordinate system (\hat{x}, \hat{y}) centered at the center of mass of the measured densities. Next, a principal axis transformation is made to a coordinate system (u, v) , with u being the direction of the largest moment. The eccentricity is defined in terms of these moments:

$$\epsilon^2 \equiv \frac{I_{uu} - I_{vv}}{I_{uu}}. \quad (4.5)$$

It can be shown that this definition of ϵ will match the eccentricity of the outer boundary if the plasma density is constant inside an ellipse. For actual plasma profiles (Fig. 4.1), Eq. 4.5 represents a weighted average.

The angle between the v axis and the radial direction, ϕ , can also be gleaned from the principal axis transformation:

$$\cos 2\phi = \frac{I_{\hat{x}\hat{x}} - I_{\hat{y}\hat{y}}}{I_{uu} - I_{vv}}, \quad (4.6)$$

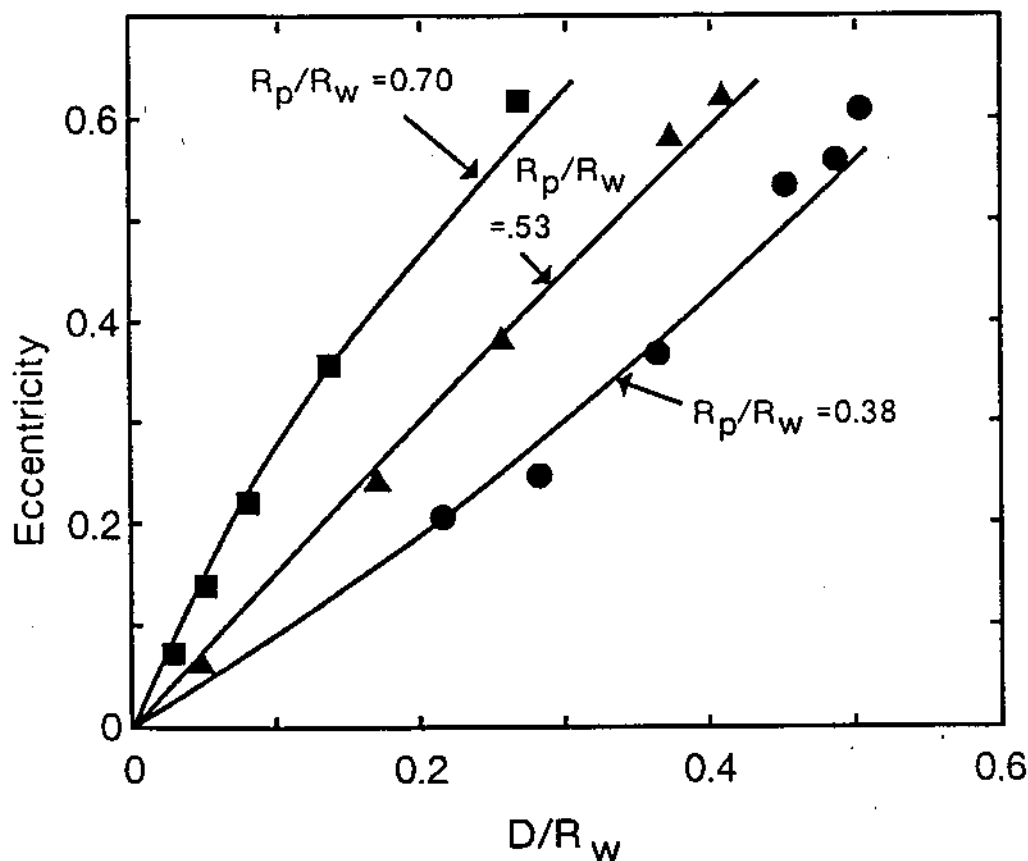


Figure 4.3: Variation of eccentricity of plasma shape versus diocotron amplitude for three different values of plasma radius R_p/R_w . Shown are the results of experiment (symbols) and the waterbag computer code (lines).

and

$$\sin 2\phi = \frac{2I_{zy}}{I_{uu} - I_{vv}}. \quad (4.7)$$

I have measured ϵ for $D/R_w < 0.5$, and $0.35 < R_p/R_w < 0.75$, as shown in Figure 4.3. The eccentricity is plotted versus D/R_w for three different radius plasmas. The eccentricity is found to increase with both D and R_p .

Also plotted in Fig. 4.3 are the results of the waterbag computer model described in Section 4.4. It is seen that the waterbag model predictions are in good agreement with experiment. Note that the eccentricity is linear with D/R_w

for small displacements, ($D/R_w < 0.2$): I have found that the formula

$$\epsilon \approx 5.4 \left(\frac{D}{R_w} \right) \left(\frac{R_p}{R_w} \right)^2 \quad (4.8)$$

is a good fit to the data in this linear range for $0.5 < R_p/R_w < 0.7$.

The values of ϕ calculated from experimental densities are shown next to the density profiles in Fig. 4.1, page 43. In both cases, the angle is less than 3° . This implies that the major axis of the ellipse is in the θ -direction, and I have found this to be true in all cases in which ϵ is large enough for an accurate calculation of ϕ .

4.3 Frequency Measurements

4.3.1 Measurement of Frequency and Displacement

I have measured the frequency, f , of the $l = 1$, $k_z \approx 0$ diocotron mode and found that the frequency varies as amplitude is increased. Upward frequency shifts as large as 20% have been measured, and smaller downward shifts have also been seen. This is in contrast to the predictions of linear theory (Eq. 3.4), wherein the frequency is necessarily independent of amplitude.

The frequency and amplitude of the mode are measured after the diocotron mode has been grown to the desired amplitude. The frequency is measured by accurately timing the interval between zero crossings of the sector probe signal. This method gives greater accuracy for the same number of cycles observed than a normal frequency counter/timer, which has an error of $1/N_{cyc}$, where N_{cyc} is the number of cycles observed. By timing zero crossings, only 100 cycles are needed to measure f to an accuracy of about one part in 10^4 .

A sample and hold circuit recorded the amplitude output of the spectrum analyzer during the frequency measurement. For an accurate measurement of amplitude, f was kept well within the analyzer bandwidth.

The plasma displacement, D , can be obtained either from the measured density $n(r, \theta)$, or from the amplitude of the sector probe signal. Defining D to be the center of mass of $n(r, \theta)$ is the most direct, but has the disadvantage that the measured coordinates have an uncertainty of about 0.2 cm. In contrast, D obtained from the sector probe signal has no offset at small amplitudes, but depends on the calibrations of all amplifier impedances and gains. To obtain the most accurate values of D , I use the measured $n(r, \theta)$ at large amplitudes to calibrate the sector probe signal.

The receiver probe is connected to ground through a 50 Ω resistor; the voltage across this resistor is then amplified to produce a signal V_{sa} at the spectrum analyzer (which is usually set to a bandwidth of 10 kHz). If D is to be correctly estimated from V_{sa} , care must be taken to correct for the effect of changes in f and N_L , where $N_L \equiv$ number of electrons per length in the column. I assume that for small changes in N_L , $N_L \propto N_t$, where $N_t \equiv$ the total number of electrons in the column. From Eq. 3.6 it can be seen that

$$D = K \frac{V_{sa}}{N_t f}, \quad (4.9)$$

where K is a proportionality constant. The constant K can be calculated from a linear fit using a series of values of D , V_{sa} , N_t and f obtained from $n(r, \theta)$ plots. For small amplitudes Eq. 4.9 can then be used to determine D from V_{sa} , N_t and f .

4.3.2 Frequency versus Displacement

The mode frequency, f , is measured for mode amplitudes ranging from the smallest detectable up to amplitudes where particles are scraped off by the wall. The data is recorded by a computer program and averaged: about 100 averages were taken at each amplitude. The lab computer generates a graph of this data, and an example of this is shown in Fig. 4.4. The horizontal axis is V_{sa} in dBm. The

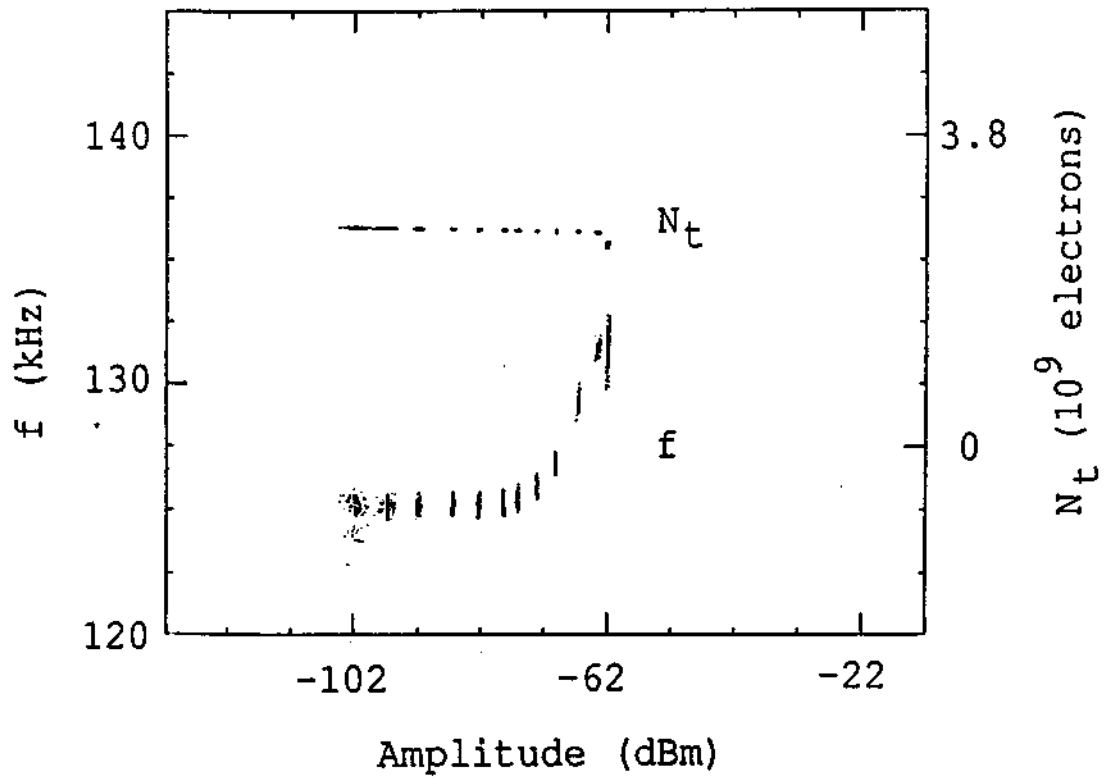


Figure 4.4: Output from frequency measurement program.

clusters of points labeled 'f' plot f on the vertical axis using the linear scale shown to the left. Each point represents one shot, and each cluster of points represents one group to be averaged, with each consecutive group taken at larger amplitudes. The scatter in f correlates well with the scatter in total number of injected electrons. The scatter in amplitude is caused by electronic noise in the detection circuit. The left-most cluster of points has a smaller cluster below it in frequency. This is because at low amplitudes the zero-crossing detector occasionally misses a cycle, and counts the frequency low. Such points are not used: the second cluster of points is the beginning of useable data.

The top set of points, labelled ' N_t ', are the corresponding endplate signals plotted on a linear vertical axis. It is seen that at large amplitudes N_t begins to decrease. This is because the outer plasma edge is 'scraping' the wall and losing electrons. I stop using the data when N_t begins to decrease sharply: this represents the upper useable limit of my frequency measurements. In this particular plot there is useable data over about 35 dB in amplitude.

One difficulty with this technique is that f changes because N_t is not exactly the same for each amplitude. Electrons at the edge of the plasma are lost to the wall, and this process varies with amplitude. Also, there are long term (over an hour) changes in the filament that results in changes in N_t . These variations in N_t are small (less than 1% except at the very largest amplitudes), but we wish to measure even smaller variations in f (less than 0.1%).

From the linear diocotron frequency relation, Eq. 3.4, it is expected that $f \propto N_L \propto N_t$. In order to correct for variations in f due to variations in N_t , I have multiplied the measured values of f by N_{t0}/N_t , where $N_{t0} \equiv$ total number at the smallest useable amplitude value in the series.

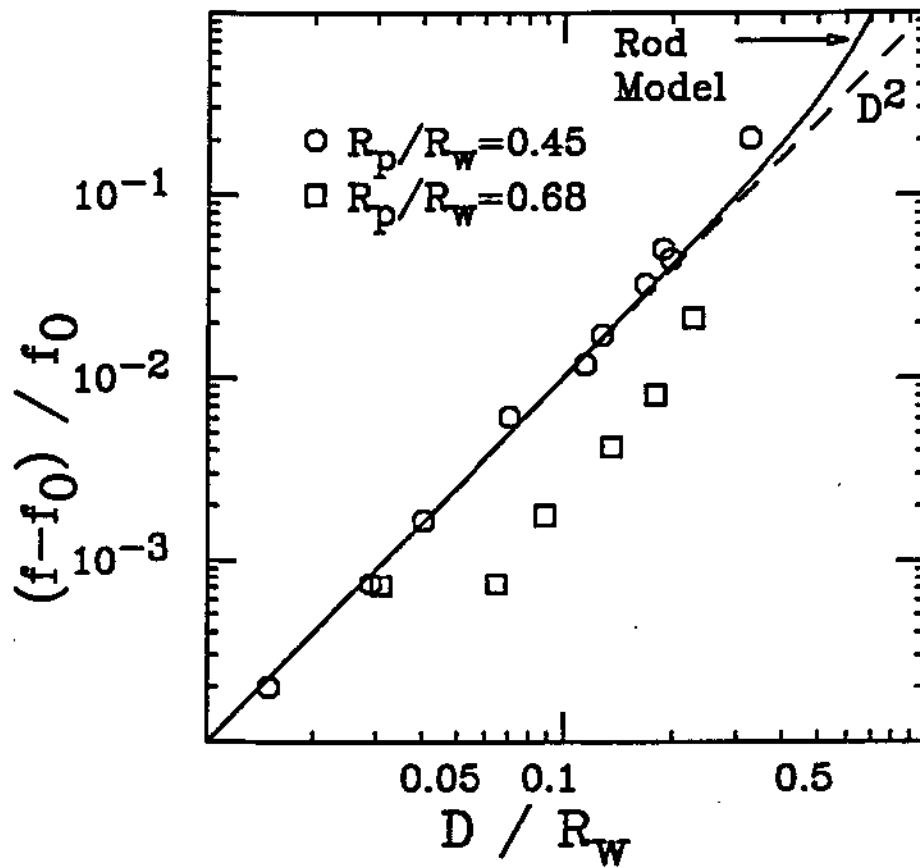


Figure 4.5: Nonlinear frequency shift versus displacement for two different radius plasmas. Also plotted are the predictions of the rod model (solid line) and $(f_0 - f)/f_0 = (D/R_w)^2$ (dashed line).

I find that the measured nonlinear frequency shift is well-fit by

$$\frac{f - f_0}{f_0} = \alpha \left(\frac{D}{R_w} \right)^2. \quad (4.10)$$

The 'zero-amplitude' frequency, f_0 , and the slope α , are determined by a linear fit to f versus $(D/R_w)^2$. Fig. 4.5 plots the results for two different radii plasmas. It can be seen in both cases that $(f - f_0)/f_0$ varies as $(D/R_w)^2$, but the slope $\alpha \approx 1$ for the 'narrow' ($R_p/R_w = 0.45$) plasma and α is smaller for the 'fat' ($R_p/R_w = 0.68$) plasma.

If this procedure is repeated for a range of R_p , it is found that α decreases smoothly with R_p/R_w . This is shown in Fig. 4.6. It can be seen that for large enough plasmas, f actually *decreases* with amplitude ($\alpha < 0$), in excellent agreement with the waterbag model, which is also plotted in Fig. 4.6. From a best fit to the data, I have derived an empirical formula for the frequency shift:

$$\frac{f - f_0}{f_0} = \left[1 - 7.3 \left(\frac{R_p}{R_w} \right)^6 \right] \left(\frac{D}{R_w} \right)^2. \quad (4.11)$$

4.3.3 Simple Model of Nonlinear Frequency Shift

Equation 4.11 can be understood as a frequency shift due to a 'rigid' displacement of the plasma column, plus a frequency shift due to an elliptical distortion of the column. The frequency shift due to rigid displacement is totally independent of the plasma profile, and can be modeled by a line charge, or infinitely thin charged 'rod'.

In the discussion of the image charge model, Section 3.2, the diocotron mode was described as the drift of the plasma in the field of an image charge at a radius of R_w^2/D . The electric field from the image was calculated at $r = 0$, even though the plasma has a substantial spatial extent around $r = 0$. This results in a prediction of frequency of the diocotron mode equal to that of linear theory.

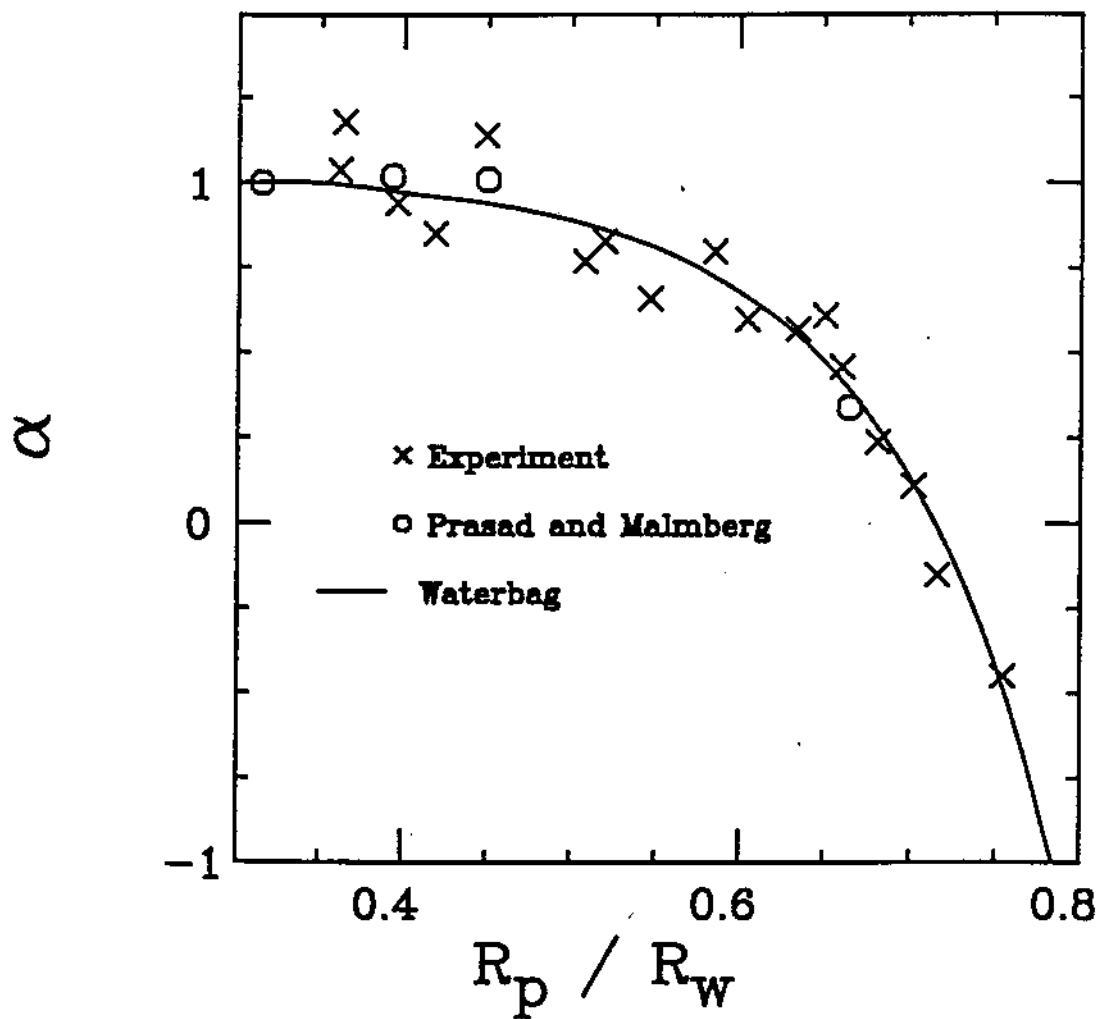


Figure 4.6: Variation of frequency shift coefficient, α , with plasma radius. Plotted are experimental points (crosses) and the predictions of the waterbag model (line). Also plotted are the results of the calculation of Prasad and Malmberg (circles).

If the electric field from the image is calculated at the center of mass of the plasma instead, there is a larger electric field and an upward frequency shift of

$$\frac{f - f_0}{f_0} = \frac{1}{1 - (D/R_w)^2} - 1 \approx \left(\frac{D}{R_w}\right)^2. \quad (4.12)$$

Note that Eq. 4.12 agrees with the empirical formula Eq. 4.11 for $R_p \ll R_w$. If the rod plasma has finite radius, the field varies somewhat across the rod. However, one can show that the average E_r is given by E_r at the center of mass.

There is an additional frequency shift due to the elliptical distortion of the column discussed in Section 4.2.2. Here, I calculate this frequency shift for small distortions and small wave amplitudes, *i.e.* $\epsilon \ll 1$ and $D/R_w \ll 1$. In order to estimate this frequency shift, it is most convenient to shift to a coordinate origin at the center of the plasma. Define an angle γ with respect to the radial direction. An elliptical distortion, ϵ , will introduce a charge perturbation δN_L per unit angle of

$$\frac{\delta N_L}{N_L} \approx \left[\left(\sin^2 \gamma - \frac{1}{2} \right) \epsilon^2 \right] \frac{d\gamma}{2\pi}. \quad (4.13)$$

Assume all this charge is at a radius R_p . The electric field due to this charge perturbation will be zero at the center of the plasma, but the image charges induced will result in an electric field causing a frequency shift of

$$\frac{f - f_0}{f_0} = -\frac{1}{4} \left(\frac{R_p}{R_w} \right)^2 \epsilon^2. \quad (4.14)$$

If the empirical formula Eq. 4.8 is used to express ϵ in terms of D and R_p , then Eq. 4.14 will predict a frequency shift equal to the second term in brackets in Eq. 4.11. Therefore, the second order frequency shifts found in both the waterbag model and experiment are completely explained by a rod model and the effect of distortion.

4.4 The Waterbag Model

I have developed a computer program that calculates the shape and frequency of a plasma column supporting a large amplitude $l = 1$ diocotron mode. The model assumes that the plasma has constant density, so that the edge of the plasma is the only density contour.

The calculation is based upon the assumption that there exists a reference frame in which the motion is steady-state. This frame is rotating at the frequency of the diocotron mode. Since electrons follow potential contours in $\mathbf{E} \times \mathbf{B}$ drift motion, the density and potential contours are coincident in this frame. The problem is then reduced to iterating the plasma shape and recalculating the potentials until the plasma boundary matches a potential contour.

The plasma shape is described by the radius of the boundary (relative to the plasma center of mass) as a function of angle. I typically divided the shape into 200 different radii at evenly spaced angles. At each iteration, the new choice of shape was constrained to conserve the cross-sectional area (*i.e.* total number of particles) and the position of the center of mass (D).

The potentials are the sum of the potential due to the plasma, plus that due to the rotation of the reference frame. The potential due to a circular plasma is easily solved by the method of images (Appendix B). Since the distorted plasma is not circular, the plasma was broken into a large circular plasma plus additional small circular plasmas around the boundary at different angles.

The potential due to rotation depends upon the frequency, f , of the diocotron mode. The frequency can be found on a particular iteration by finding the point of minimum potential in the rotating frame: the value of the electric field at that point in the *lab* frame gives the $\mathbf{E} \times \mathbf{B}$ rotation rate.

On each iteration, the potential is calculated along the plasma boundary,

and a choice for the next iteration of shape is made in order to minimize the variation of the potential along the boundary. The value of f used is the rotation rate of the preceding iteration. This process is continued until the variation of potential along the boundary is smaller than a given amount: I chose this to be one part in 10^5 , which required about 50 iterations.

The boundary shapes match very well the elliptical shapes observed experimentally (Section 4.2.2). Furthermore, the predicted values of f and ϵ are found to be in excellent agreement with experiment over the complete range of R_p and D , as shown in Figs. 4.3 and 4.6.

4.5 Comparison with Calculation of Prasad and Malmberg

The predictions were also compared to the results of a computer calculation based upon a perturbation theory published by Prasad and Malmberg [24]. Their calculation is also based upon the assumption that a unique reference frame exists in which the potential and density contours are coincident.

Prasad and Malmberg find that $(f - f_0)/f_0 = \alpha(D/R_w)^2$ for small D , and I have estimated the proportionality constant α from their calculations. These are plotted as circles in Fig. 4.6 for four different radius plasmas, and are seen to agree with experiment. Their predictions, however, only agree with experiment for $D/R_w < 0.1$.

In Fig. 4 of Ref. [24], predictions of frequency versus amplitude are made for a plasma closely resembling an experimental profile with $R_p/R_w = 0.40$. These results are plotted in Fig. 4.7 along with the results of experiment, the rod model, and the waterbag model. It can be seen that the predictions of Ref. [24] are smaller than experiment for displacements $D/R_w > 0.1$, while the rod and waterbag models

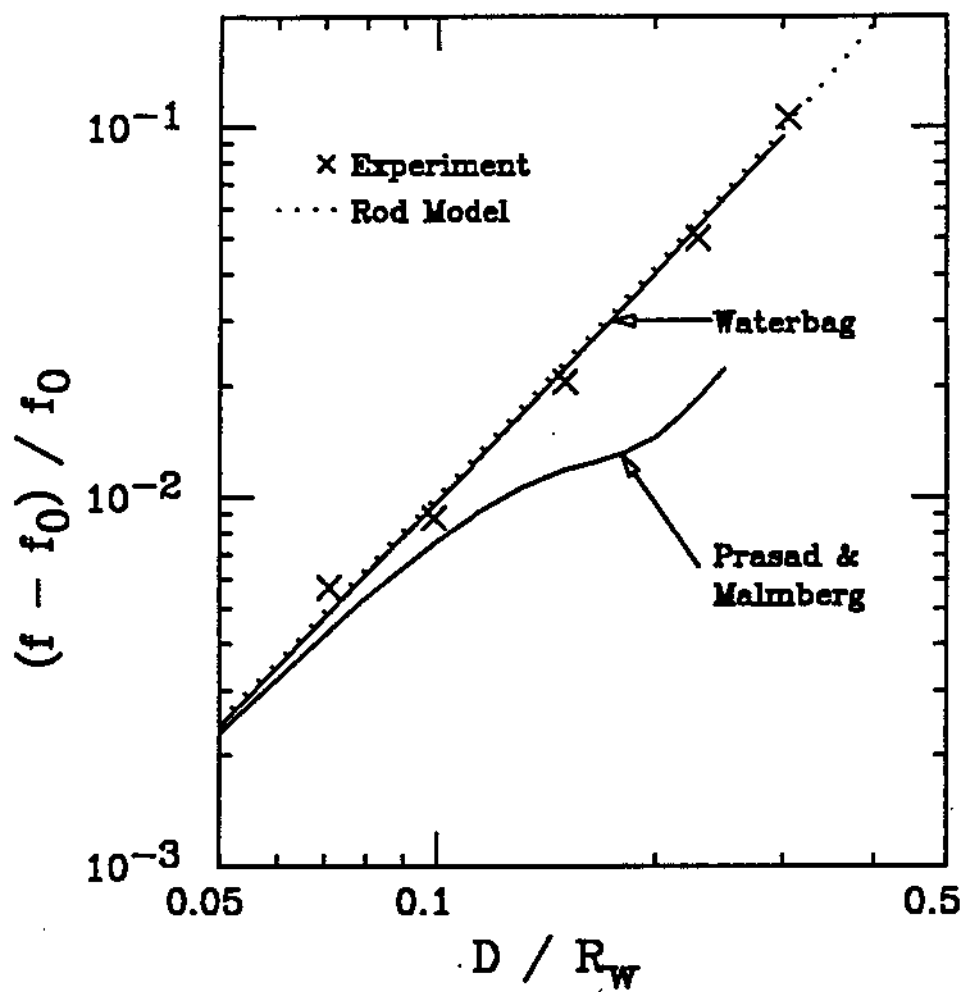


Figure 4.7: Nonlinear frequency shift versus amplitude for $R_p/R_w = 0.40$. Calculation of Prasad and Malmberg (Fig. 4 of Ref. [24]) is plotted along with the rod model, the results of the waterbag model, and experiment (crosses).

are in good agreement.

The calculation of Ref. [24] is based upon a perturbation theory, and the discrepancy with experiment is probably due to the omission of higher order terms. I believe that this theory suffers from the choice of the cylindrical wall axis instead of the plasma center as the coordinate origin: large perturbations are required just to model the zero-order displacement of the column.

Chapter 5

The Finite Length Diocotron Mode

5.1 Overview

Experimentally, the $l = 1$, $k_z \approx 0$ diocotron mode is remarkably stable in a finite length plasma, oscillating through 10^5 cycles with negligible change in amplitude. If the diocotron mode in a finite length plasma is simply modeled as an off-axis displacement, the image electric field will be z -dependent, the $\mathbf{E} \times \mathbf{B}$ drift will be z -dependent, and the plasma will not stay together. Clearly the mode must actually assume a z -dependent structure. The effect of this z -dependence on the diocotron mode is the topic of this chapter.

I have measured the small-amplitude frequency, f , of the diocotron mode as a function of plasma length and radius for $0.67 < L_p/R_w < 10$ and $0.25 < R_p/R_w < 0.73$. Furthermore, the number of electrons per length, N_L , has been calculated for each of these plasmas from the radial density profiles, and the infinite length frequency, f_d , of each column has been computed using these values of N_L in Eq. 3.4. I find that the fractional frequency shift $(f - f_d)/f_d$ increases as L_p^{-1} , and decreases with R_p . Furthermore, the fractional frequency shift versus length has been measured at three different values of B_z , and no dependence upon magnetic field has been found. Upward frequency shifts of over 200% have been observed.

These frequency measurements are in reasonable agreement with a theory of the finite length diocotron mode by Prasad and O'Neil [27]. The theory calculates the z -dependence of the mode by requiring the continuity of the mode potential at the plasma ends. This condition implies that the mode potential becomes concave as a function of z . To first order in R_w/L_p this potential is approximated by a section of a diocotron mode with a small, complex k_z . The finite length frequency is predicted to be the frequency of a mode with wavenumber k_z .

I have also measured the damping rate of the finite length diocotron mode at $B_z = 94, 188$ and 376 gauss and at different amplitudes. In all cases, the diocotron mode was found to not change amplitude to within the accuracy of the measurement, which establishes an upper limit on the damping rate. This result is contrary to the predictions of a theory by Prasad and O'Neil [26], which predicts damping rates that are three to four orders of magnitude greater than the limits established by experiment.

The theory predicts the introduction of Landau damping through the existence of small plasma modes coupled to the diocotron mode. I have estimated the velocity of resonant electrons and found that it is approximately equal to the thermal velocity. Furthermore, I have estimated the energy that must be absorbed by the plasma in order to damp a small amplitude diocotron mode, and have found that this energy is 10^{-3} times the thermal energy at the lowest diocotron amplitudes measured. Under these conditions the plasma modes would be effectively Landau damped, and the large discrepancy between theory and experiment suggests a fundamental problem in the theory.

5.2 Theory

This section will summarize two theoretical papers by Prasad and O'Neil about the finite length diocotron mode. The first paper by Prasad and O'Neil [27] models the plasma as a cold fluid. This paper uses an idealization of the experimental plasma illustrated by Fig. 5.1a.

The plasma is assumed to be constant density out to radius R_p . The plasma is assumed to have square ends, and the line density or the number of electrons per axial length, N_L , is assumed to be constant within the plasma. For purposes of the wave calculation, the wall is assumed to be continuous and grounded. Note that this simple model is entirely characterized by the parameters N_L , R_p , L_p , R_w and B_z .

The plasma is assumed to be far below the Brillouin limit; or $\omega_p \ll \omega_c$, where ω_p is the plasma frequency and ω_c is the cyclotron frequency. In this regime, centrifugal and pressure drifts can be ignored, and the plasma rotates about its axis at the $\mathbf{E} \times \mathbf{B}$ drift frequency ω_r :

$$\omega_r = \frac{\omega_p^2}{2\omega_c}. \quad (5.1)$$

The plasma behaves as a cold, dielectric fluid with dielectric constant

$$\epsilon_{zz} = 1 - \frac{\omega_p^2}{(\omega - l\omega_r)^2}. \quad (5.2)$$

Using Eq. 5.1 in Eq. 5.2, and also using the diocotron frequency relation Eq. 3.4, we see that for the diocotron mode

$$\epsilon_{zz} \approx -\frac{\omega_p^2}{\omega_r^2} = -4 \frac{\omega_c^2}{\omega_p^2}, \quad (5.3)$$

so that inside the plasma ϵ_{zz} is a large negative number.

The effect of the ends is incorporated by requiring the continuity of ϕ and $\epsilon_{zz}\partial\phi/\partial z$. These continuity requirements are implemented by a perturbation

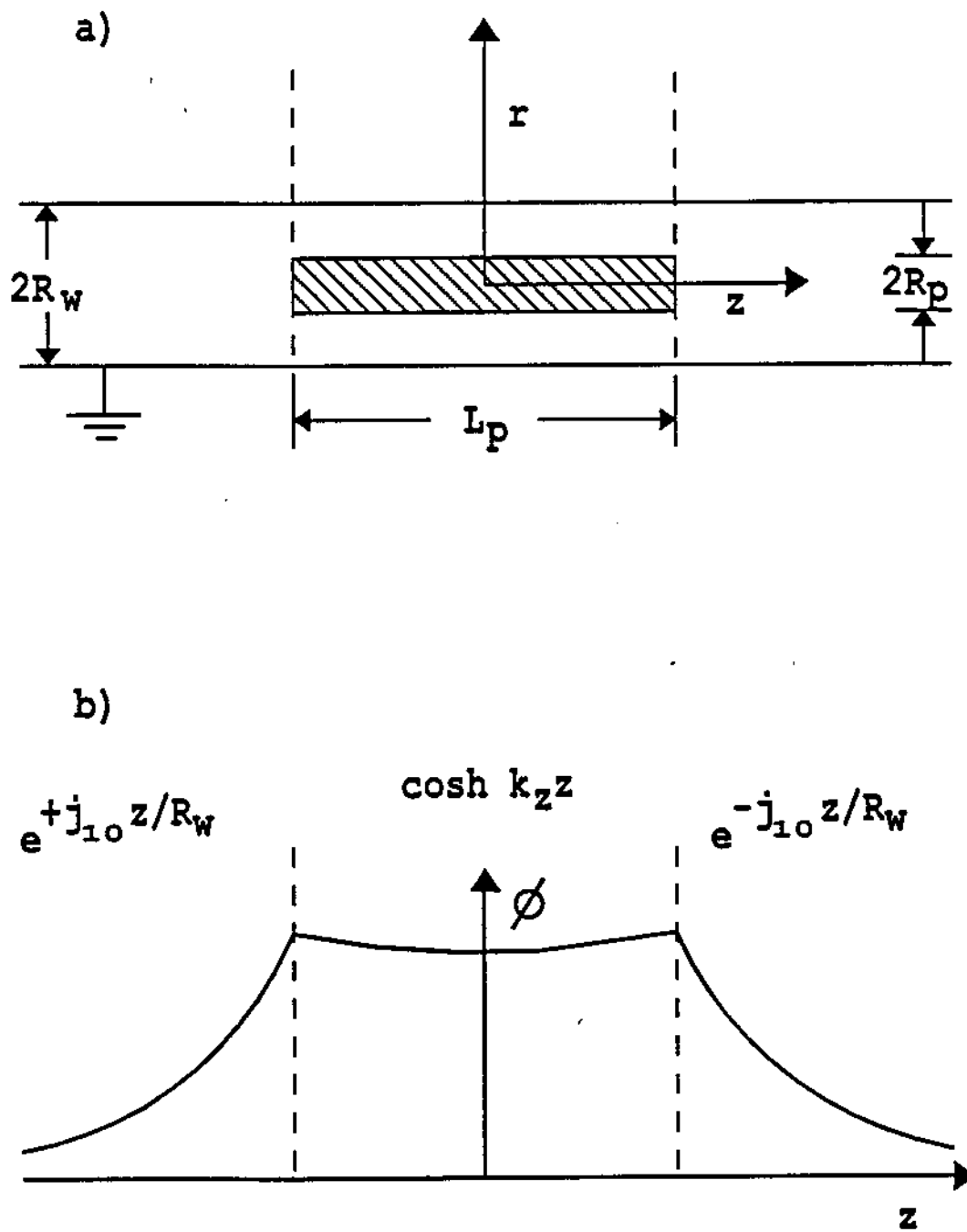


Figure 5.1: Idealized model of Prasad and O'Neil: a) geometry, b) potential inside plasma versus z .

series in two small parameters: the finite length parameter R_p/L_p ; and a parameter related to the dielectric 'stiffness' of the plasma, $\delta = (-\epsilon_{zz})^{-1/2} \approx \omega_p/2\omega_c$.

Prasad and O'Neil present the results of an analysis that is first order in R_p/L_p and δ for the $l = 1, 2$ and 3 diocotron modes. We can get an intuitive feel for the result for the $l = 1$ mode with the aid of Fig. 5.1b.

Figure 5.1b plots the mode potential, ϕ , versus z at some radius within the plasma. Outside the plasma, the mode potential satisfies Laplace's equation, and varies approximately as $\phi \sim \exp(\pm j_{10}z/R_w)$, where j_{10} is the zeroth root of the J_1 Bessel function, and the sign is chosen so that $\phi \rightarrow 0$ far from the plasma. The mode potential inside the plasma must join to the vacuum solution so that $\epsilon_{zz}\partial\phi/\partial z$ is continuous across the plasma edge. Since $\epsilon_{zz} = 1$ in the vacuum, and ϵ_{zz} is a large negative number inside the plasma, ϕ becomes slightly concave in the plasma, as shown in Fig. 5.1b.

Prasad and O'Neil show that ϕ is approximated inside by an infinite length diocotron mode with a wavelength much longer than the plasma. The dispersion relation for $l = 1$ diocotron modes varying as $e^{ik_z z}$ (see [27]) is

$$\omega = \omega_d - (\omega_c/4)(k_z R_p)^2, \quad (5.4)$$

which is plotted in Fig. 5.2 for typical experimental parameters.

The dashed line shows imaginary k_z ; the solid line shows real k_z . The mode with imaginary k_z is usually ignored in a treatment of an infinite column because it diverges as $z \rightarrow \pm\infty$. However, this objection does not apply to the finite length case, and it is the imaginary k_z mode that approximates the concave shape of the finite length mode.

We see from Fig. 5.2 that the finite length diocotron mode will be shifted upward from the $k_z = 0$ frequency, f_d . Prasad and O'Neil present the results of the calculation of this frequency shift in graphical form. For reference I write down an

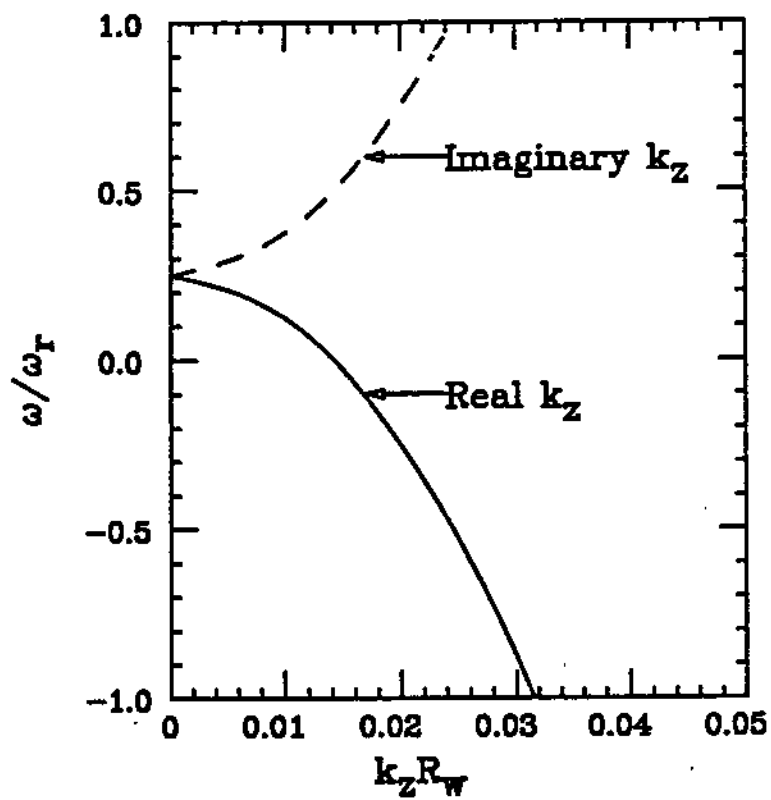


Figure 5.2: Dispersion curves for z -dependent, infinite length $l = 1$ diocotron mode. Drawn to scale for typical experimental parameters: $R_p/R_w = 0.5$, $\omega_p/\omega_c = 0.02$, $\omega_r/\omega_p = 0.01$. The dashed line indicates the imaginary k_z mode. See Ref. [27].

approximate formula that reproduces their graph:

$$\frac{f - f_d}{f_d} = \left(1.30 - 1.08 \frac{R_p}{R_w}\right) \left[\frac{1}{R_p/R_w} - \frac{R_p}{R_w} \right] \left(\frac{R_w}{L_p} \right), \quad (5.5)$$

valid for $.1 < R_p/R_w < .8$. The experiments to be described in the next section are in close agreement with this prediction.

The stability of the finite length diocotron mode is explored in a second paper by Prasad and O'Neil [26]. This second paper uses the drift-kinetic approximation, which adds the effect of bounce motion in z and parallel temperature. The finite length diocotron mode is also expressed in terms of infinite length modes. However, in this paper the modes are quantized so that $k_z = n\pi/L_p$. The calculation is a perturbation theory in the small parameter R_w/L_p . To lowest order in R_w/L_p , Prasad and O'Neil find that the finite length diocotron mode is just the $k_z = 0$ mode. To the next order in R_w/L_p , small $l = 0$ plasma modes with $k_z = n\pi/L_p$ are mixed in with the diocotron mode.

The presence of the small plasma modes introduces resonant particles and consequently Landau damping. This is especially significant since the $k_z = 0$ diocotron mode is otherwise neutrally stable. Prasad and O'Neil calculate the imaginary part of the frequency of the diocotron mode that appears due to this Landau damping. This imaginary part occurs in order $(R_w/L_p)^2$ and is given by:

$$\omega_i = -[0.4] (\omega_r - \omega_d) \left(\frac{\omega_r - \omega_d}{\omega_p} \right) \ln \left(\frac{\omega_p}{\omega_r - \omega_d} \right) \frac{2\lambda_D}{L_p}, \quad (5.6)$$

where ω_r is the rotation frequency and λ_D is the Debye length. (The 0.4 in brackets is the approximate value of a function of R_p/R_w that varies between 0.3 and 0.5 in Fig. 5 of Ref. [26].) As will be seen in Section 5.4, my experimental measurements give no indication of this damping.

The final significant prediction of Prasad and O'Neil is that for certain choices of plasma parameters the diocotron and plasma frequencies become equal.

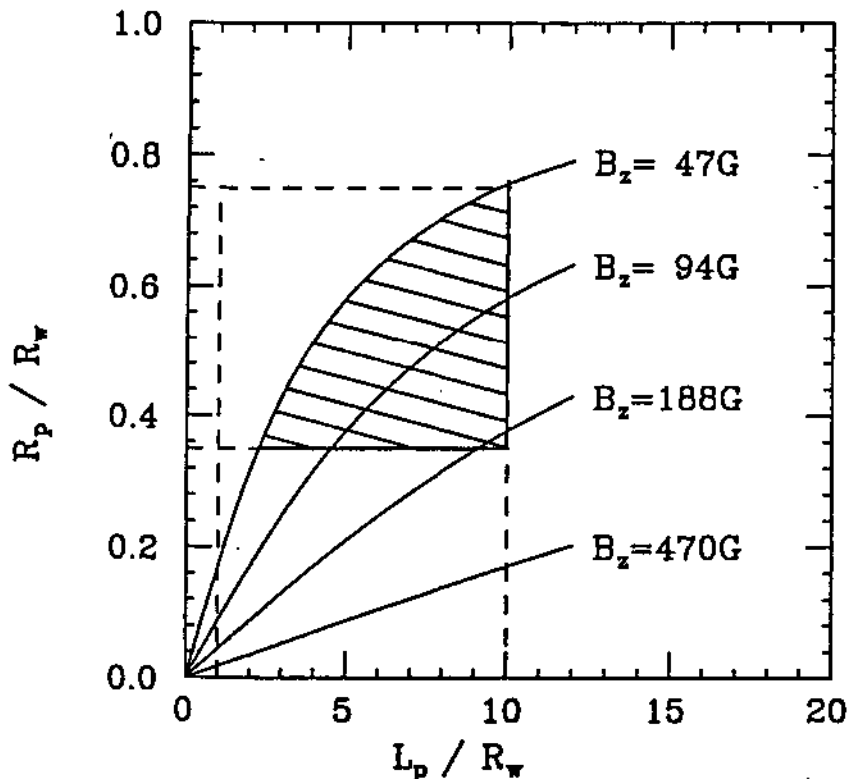


Figure 5.3: Values of L_p and R_p that satisfy degeneracy condition between diocotron mode and $m = 1$ plasma mode for four different values of B_z . Typical values of L_p and R_p for the EV experiment lie between the dashed lines: degeneracy is reachable within the triangular shape.

This degeneracy is predicted to cause the plasma wave amplitude to be of the same order as the diocotron amplitude, giving a greatly increased damping rate. The condition for the diocotron mode to be degenerate with a plasma wave with radial mode number n and wavenumber $k = m\pi/L_p$ is

$$\frac{R_p}{L_p} = \frac{1}{2} \frac{j_{2n}}{m\pi} \left[1 - \left(\frac{R_p}{R_w} \right)^2 \right] \frac{\omega_p}{\omega_c}, \quad (5.7)$$

where j_{2n} is the n -th root of the J_2 Bessel function.

The degenerate values of R_p and L_p are plotted in Fig. 5.3 for $n = 1$ and $m = 1$, for a density of 10^7 cm^{-3} . The solutions of Eq. 5.7 for different values of B_z appear as a family of curves. Values of R_p and L_p that can easily be reached

in the EV experiment lie between the dashed lines. The EV experiment can easily match the degeneracy condition inside the shaded region in Fig. 5.3. However, no systematic experimental search was made to detect this degeneracy.

In summary, there are three theoretical predictions made by Prasad and O'Neil that can be checked by experiment: 1) The upwards frequency shift of a finite diocotron mode from the $k_x = 0$ value f_d (Eq. 5.5) 2) The damping induced in the diocotron mode which is neutrally stable for $k_x = 0$ (Eq. 5.6) 3) Greatly enhanced damping of the diocotron mode at certain plasma parameters due to a degeneracy with a plasma wave (Eq. 5.7).

5.3 Shifts in the Real Part of the Frequency

The experimental setup of the finite length frequency measurement is almost identical to the setup for the measurement of the nonlinear diocotron mode. The small-amplitude frequency, f , is desired, and this can be obtained from a series of data taken at different amplitudes, as described in Chapter 4.

The only significant difference is the use of 'cutting'. If a short plasma is desired, a cylinder within the containment region is ramped from ground to a negative voltage to 'cut' the plasma into two sections. The experiment will then be performed with only the plasma nearer the dump gate, and I assume that the other plasma is sufficiently separated by the cut gate to be ignored.

The cutting procedure is used because the tilt effect is much stronger in longer plasmas. In Chapter 6, data will be presented on the transport due to tilt for different containment lengths, L_c . Essentially, I have found that a tilt angle that causes rapid transport to a square low noise profile in a plasma with $L_c = 35.6$ cm will have barely noticeable effect in a plasma with $L_c = 19.8$ cm. Therefore, the tilt is used to 'prepare' the plasma with $L_c = 35.6$ cm (or greater), and then the

plasma is cut to obtain a shorter length.

A profile is taken for each plasma without the diocotron mode present to determine the initial state of the plasma. An example is shown in Fig 2.2b. The plasma is squarish and low noise.

The finite length theory of Prasad and O'Neil depends only upon the parameters N_L , R_p , L_p , R_w and B_z . Both B_z and R_w are known from direct measurement. The parameters N_L , R_p , and L_p do not have unambiguous definitions in the experimental plasma. The experimental plasma has rounded ends (see Fig. 2.1); N_L will be a function of z , and L_p will be a function of r .

I proceed by making reasonable, self-consistent definitions of these three quantities using initial profiles of which Fig. 2.2b is an example. The plasma radius, R_p , is defined to be the point at which the measured projection density, $Q(r)$, falls to one-half of its value at the center. There are a number of other reasonable definitions. An example is the radius of a column with the same central density and total number of electrons. However, because the density profile is nearly square, these definitions all give about the same radius.

As was described in Chapter 2, profiles like the ones in Fig. 2.2 can be used as input to a computer program that calculates $n(r, z)$. Define a line density at each point in z by

$$N_L(z) = \int_0^{R_w} dr 2\pi r n(r, z). \quad (5.8)$$

This line density must be averaged over z to obtain a single number. A reasonable way to do this is to weight N_L by the number of electrons per length, or just N_L :

$$\overline{N_L} \equiv \frac{\int_{-\infty}^{\infty} N_L^2(z) dz}{\int_{-\infty}^{\infty} N_L(z) dz}. \quad (5.9)$$

The plasma length is defined to be consistent with $\overline{N_L}$ and the measured total number of electrons, N_T :

$$L_p \equiv \frac{N_T}{\overline{N_L}}. \quad (5.10)$$

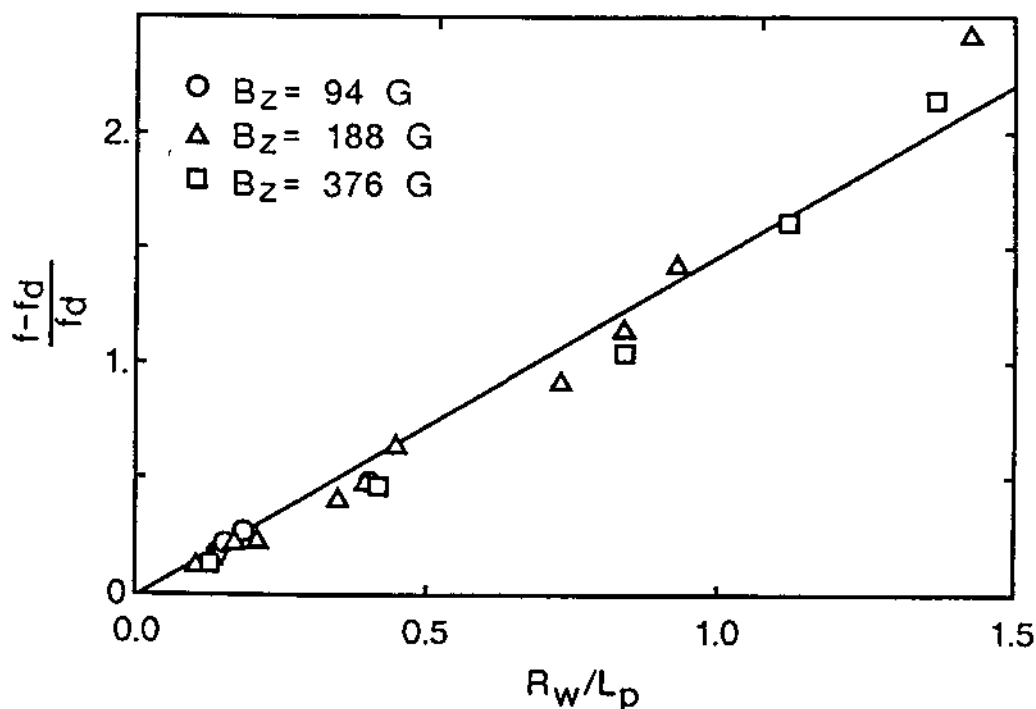


Figure 5.4: Finite length frequency shift versus L_p^{-1} holding plasma radius approximately constant.

These definitions are used to experimentally test Eq. 5.5. For each plasma, an initial profile is taken, and from this profile R_p , $\overline{N_L}$ and L_p are calculated. Then f_d is calculated using Eq. 3.4. Next, the diocotron frequency is measured as a function of amplitude, and extrapolated back to zero amplitude to obtain a value for f . The experiment is repeated for different plasma R_p and L_p values and $(f - f_d)/f_d$ is compared to the predictions of Eq. 5.5.

Figure 5.4 shows the results of this procedure for various plasma lengths L_p . Here, the radius R_p was kept as constant as possible: for the points shown $0.436 < R_p/R_w < 0.451$. The data was taken at three different B_z values: 94 gauss, 188 gauss, and 376 gauss. At $B_z = 188$ gauss the frequencies measured varied from 70 to 250 kHz, with N_L varying by a factor of 2.4 due to the cutting procedure. The theory line in Fig. 5.4 is the result of using $R_p/R_w = 0.44$. Note the good

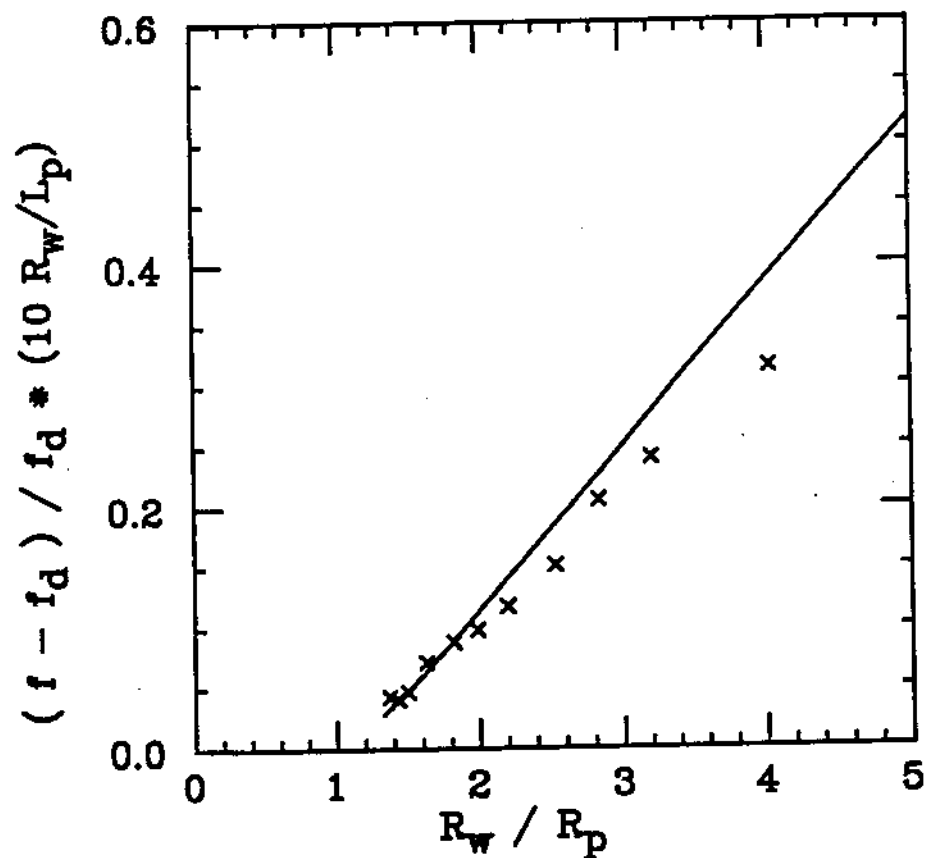


Figure 5.5: Finite length diocotron frequency shift versus R_p^{-1} holding plasma length approximately constant.

agreement between theory and experiment, even at $R_w/L_p > 1$. Also note that there is no indication of magnetic field dependence, which is also in agreement with theory.

Figure 5.5 plots the measured frequency shift when R_p is varied while keeping L_p approximately constant. For these points $0.099 < R_w/L_p < 0.124$. The experimental points plotted are corrected for this 25% variation by multiplying by the factor $(10/(L_p/R_w))$, *i.e.* presuming the length variation in Eq. 5.5. The theory line comes from using $L_p/R_w = 10$ in Eq. 5.5. There is a trend for the data to fall below theory for small R_p , but there is still reasonable agreement between theory and experiment.

To summarize, I have compared the real frequency shifts of the finite length diocotron mode to the idealized theoretical model of Prasad and O'Neil by making reasonable definitions of plasma parameters. The agreement between theory and experiment is reasonable, even at plasma lengths where the experimental plasma is more spherical than cylindrical.

5.4 Shifts in the Imaginary Part of the Frequency

The finite length theory of Prasad and O'Neil predicts that the diocotron mode will acquire a small damping due to coupling with plasma modes. This damping rate is given by Eq. 5.6. In this section an experiment will be described to measure the long time damping of the diocotron mode. The experimental measurements show none of the predicted damping.

The experimental procedure is similar to that described in Chapter 4. Field tilt is used to obtain a low noise profile, and feedback combined with a comparator is used to grow the diocotron mode to a repeatable amplitude. There is a difficulty with using this setup for the measurement of the long term stability of the diocotron

mode: the input impedance of the receiving amplifier will cause a small growth (see Section 3.4) that can mask the damping that is expected from Eq. 5.6.

In order to circumvent this difficulty, the receiving probe is connected to the receiving amplifier through a relay. When the relay is energized, the receiving amplifier is connected to the receiving sector, otherwise the receiving sector is connected to ground. The relay is energized for an initial period during feedback growth, at the end of the growth the amplitude is measured and the relay turned off. Then, after waiting many diocotron cycles (about 10^5), the relay is again energized and the amplitude is measured again.

Note that the sector probe cable resistances and finite wall resistance (see Section 3.4) are predicted to produce a growth ω_i with $\omega_i/\omega \sim 2 \times 10^{-8}$.

The amplitude is measured by connecting a digital oscilloscope to the output of the spectrum analyzer. The analyzer is operated as a bandwidth filter turned to the diocotron frequency, and its output voltage is proportional to the log of the diocotron amplitude versus time. The oscilloscope has the capability of averaging the amplitude over many shots to reduce noise.

There is an upper limit on the number of cycles between the initial and final amplitude measurements. As was mentioned in Section 2.7, there is a slow expansion of the plasma towards the wall. At some point in time this expansion will result in particle loss to the wall. The particle loss will in turn cause the frequency and amplitude of the signal to decrease. In order to avoid this, the time at which particle loss to the wall occurs is taken as the upper limit on the time that the final amplitude is measured.

The results of these measurements are shown in Table 5.1. The decay rate was measured at three different magnetic fields and several different amplitudes. All the data was taken with a plasma length $L_p \approx 30$ cm. In all cases no decay

B_z (gauss)	D/R_w	v_{res}/v_{th}	$-\omega_i/\omega(10^{-6})$		Theory/Exp (10^3)
			Exp	Theory	
94	0.008	0.29	< 0.6	1000	1.7
	0.317		< 0.2		5.0
188	0.020	0.49	< 0.09	1500	17
	0.063		< 0.02		75
	0.126		< 0.09		17
376	0.025	0.75	< 0.2	1500	7.5
	0.032		< 0.2		7.5
	0.112		< 0.09		17
	0.159		< 0.09		17

Table 5.1: Comparison between diocotron damping rates predicted by the theory of Prasad and O'Neil and experimental measurements.

of the wave was actually observed, and the measurements only established upper limits on the experimental decay rates. The predictions of Eq. 5.6 are also shown in Table 5.1. The measured damping rates are smaller than the predictions of theory by three to four orders of magnitude.

The theory also uses the approximation $v_{res}/v_{th} \gg 1$, where v_{res} is the velocity of a resonant electron, and v_{th} is the thermal velocity. The resonant velocity can be calculated from the condition that a resonant electron be in phase with the wave, giving $\omega - l\omega_r - k_z v_{res} = 0$. The results are shown in Table 5.1. In all three cases $v_{res} \approx v_{th}$, so that the theory approximation is not satisfied. Nevertheless, in Landau damping the damping is usually *maximum* when $v_{res} \approx v_{th}$, since the number of resonant particles available to absorb the wave energy is large. It is difficult to see how having $v_{res} \approx v_{th}$ could *decrease* the damping.

It is possible that the background velocity distribution is heavily modified by the diocotron mode, which would tend to reduce the damping. To estimate the effect of the diocotron mode on the thermal distribution, it is instructive to calculate the change in electrostatic energy that would occur if the mode were

completely damped. This energy change is not just due to the mode energy, because the column must also expand in order to conserve the angular momentum, P_θ . This expansion will lower the energy in the column. To estimate these energy changes, assume that the column initially has a square profile of radius R_p and a diocotron amplitude of D . Also assume that after the diocotron mode damps away, the column is still a square profile with a radius larger by ΔR_p . In addition, ignore the effect of the ends on the energy.

The profile must expand by the amount

$$\Delta R_p = \frac{D^2}{R_p} \quad (5.11)$$

in order to conserve P_θ . The electrostatic energy per length of a centered column of radius R_p is

$$\frac{W}{L_p} = \frac{e^2 N_L^2}{4\pi\epsilon_0} \left(\frac{1}{4} + \ln \frac{R_w}{R_p} \right), \quad (5.12)$$

so that the electrostatic energy per length changes by an amount

$$\frac{\Delta W}{L_p} \approx -\frac{e^2 N_L^2 D^2}{4\pi\epsilon_0 R_p^2}. \quad (5.13)$$

The diocotron mode energy per length is given by Eq. 3.5. The mode energy change is *positive* when the mode damps; adding this to Eq. 5.13 the total energy change per electron is

$$\frac{\Delta W_t}{N_L L_p} = -\frac{e^2 N_L}{4\pi\epsilon_0} D^2 \left(\frac{1}{R_p^2} - \frac{1}{R_w^2} \right) = -(2 \times 10^{-3} \text{ eV}) \left(\frac{D/R_w}{0.01} \right)^2, \quad (5.14)$$

where the last equality is obtained by taking experimental values $N_L = 5 \times 10^7$ electrons per cm and $R_p/R_w = 0.5$. The plasma temperature is about 1 eV, so that for the smallest amplitudes in Table 5.1, the energy the plasma must absorb to damp the mode is 10^{-3} times the thermal energy per electron. Since for $v_{res}/v_{th} \approx 1$ a large fraction of the electrons would partipate in the damping, it seems unlikely

that modification of the electron distribution is the source of the large discrepancy between theory and experiment.

Even if the distribution function were modified by the mode, electrons would be scattered into resonance at a high rate. The 90° scattering time for a thermal particle in an electron plasma is

$$\nu_{ee} \approx 220 T^{-3/2} \left(\frac{n}{10^7} \right) \text{sec}^{-1}, \quad (5.15)$$

where T is in units of eV and n is in cm^{-3} (see [15]). At 1 eV and a density of 5×10^6 , the distribution would refill roughly 100 times a second, and even less energy would have to be absorbed by a thermal electron to damp the mode.

The damping of the diocotron mode has been previously measured by DeGrassie [8] in a similar experiment. DeGrassie found that the diocotron amplitude $\delta\phi$ decayed as $|\delta\phi|^2 \sim \exp(-\alpha^2 t^2)$, where α was found to vary with pressure. DeGrassie's experiment operated at higher neutral pressures than EV (10^{-6} Torr as opposed to 5×10^{-11} Torr), and the background transport was much higher due to the neutrals. It is likely that some electrons had expanded to the wall by the time the diocotron wave was measured. Neither the effect of the wall or of neutral collisions on the diocotron wave have been investigated in the EV machine.

Chapter 6

Induced Damping and Transport from External Field Perturbations

6.1 Overview

The effect of field perturbations on plasma transport is of central importance in plasma physics. In this chapter, the effects on the electron plasma of two particularly simple perturbations are discussed.

One perturbation is the 'squeeze' field, in which an axisymmetric electric field is created by a voltage, V_{pert} , applied between the cylinders in the containment region. The effect of this perturbation is to induce exponential damping in the previously neutrally stable diocotron mode. Since the fields are axisymmetric, the damping should conserve P_θ , and this has been verified by experiments. A description of the damping has emerged from phase-locked density measurements: the diocotron displacement, D , decreases smoothly and continuously while the plasma radius expands to keep P_θ constant.

I have measured the exponential damping rate, γ , versus V_{pert} and D at four different values of B_z . At small amplitudes ($|V_{pert}| < 0.5$ Volts), γ is proportional to V_{pert}^2 . The scaling with B_z is roughly $\gamma \propto B_z^{-2}$.

I speculate that the z -dependent squeeze perturbation introduces resonant particles and consequently damping. It is possible that this is via the nonlinear

interaction proposed by Crawford, O'Neil and Malmberg [5], and calculated in detail by Crawford and O'Neil [4]. In the case of the squeeze perturbation, the nonlinear interaction would be between the squeeze field and the diocotron wave. A beat wave would be produced that would transfer electrostatic energy in the plasma into thermal energy via Landau damping. This is consistent with the electrostatic energy *decreasing* when the diocotron mode is damped. (Electrostatic energy decreases when the diocotron mode is damped due to the plasma expansion necessary to conserve P_θ , see Section 5.4). Their theory predicts exponential damping of the diocotron mode proportional to V_{pert}^2 , in agreement with experiment. For the $k_z = \pi/L_p$ component of the squeeze field, the theory also predicts a peak in the damping near the center of the experimental range of B_z , and this has not been observed. Higher k_z components in the squeeze field may explain this discrepancy.

The second perturbation is the magnetic field tilt introduced in Chapter 2. The tilt differs from the squeeze field in that it is not axisymmetric. Therefore, the transport induced by the tilt does not necessarily conserve P_θ . I have measured the rate of change of angular momentum, ν_p , and the rate of change of the central density, ν_0 , versus tilt angle. I have found that tilt angles as small as 10^{-4} radian can induce significant particle transport. These measurements were repeated at five different values of B_z , and three different values of L_p . In all cases, the minimum of ν_p occurs at approximately the same angle as the minimum of ν_0 , corresponding to optimal alignment. I find that $d\nu_p/d\theta$ varies approximately as B_z^{-2} . Also, the tilt effect is much less strong in short plasmas, although I have not obtained the scaling versus L_p .

The tilt transport has a dramatic effect on the radial profile, producing square density and flat temperature profiles, and reducing the shot-to-shot jitter

by a factor of ten. These profiles resemble thermal equilibrium profiles [22,25], but they are not thermal equilibria: I find that the width of the plasma edge is substantially less than the predicted edge width for thermal equilibrium of $2\lambda_D$. I speculate that the tilt transport drives the plasma towards a state where the $E \times B$ drift rate is constant with radius, perhaps by increasing internal mixing.

There will be electrons in the plasma that will be resonant with the tilt field, and it may be that these electrons are driving the transport. However, no careful theory has yet been formulated for this case. It may be that this particularly simple perturbation will provide an incisive test of resonant particle transport theory.

6.2 Axisymmetric Electrostatic Field Perturbations (Squeeze)

6.2.1 Measurement of Induced Diocotron Mode Damping

Figure 6.1 illustrates the induced damping experiment. At the top of Fig. 6.1 is a schematic of the experiment. The containment region is divided into two equal length cylinders. The cylinder nearest the dump gate includes the sector probes, and is at ground potential. One sector probe, the receiver, is connected to amplifiers and a spectrum analyzer, and is used for detecting the diocotron mode. The other probe, the resistive growth sector, is connected to a resistor through a relay. This resistor causes the diocotron mode to grow due to the resistive wall instability (see Section 3.4). The only reason that feedback techniques were not used is that this experiment was completed before the feedback circuitry was in place.

The cylinder nearest the inject cylinder is connected to a 'perturbator'. The perturbator is a voltage pulser that has its output at ground potential during the injection of the plasma and the growth of the diocotron mode. The perturbator

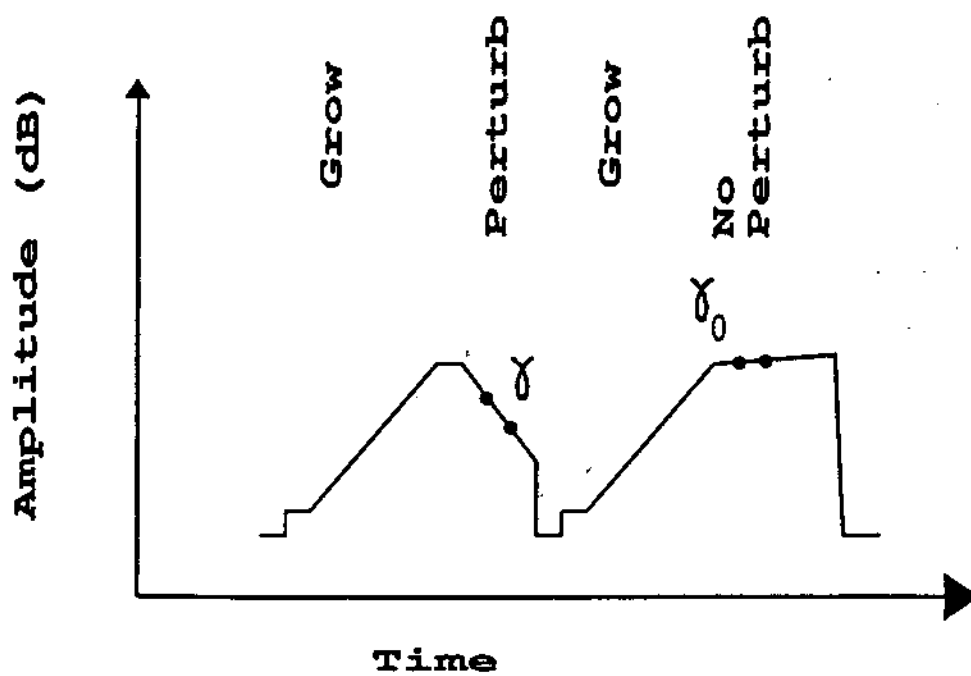
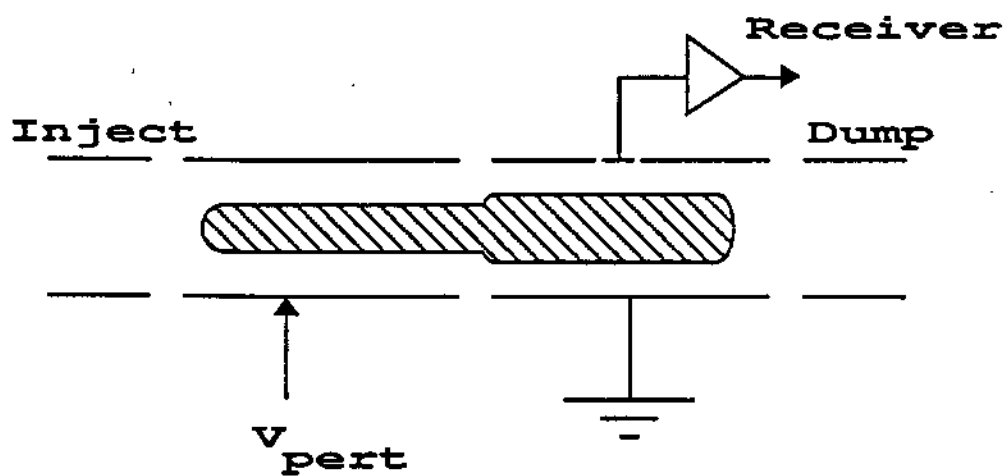


Figure 6.1: Experimental setup to measure induced damping as a function of V_{pert} , amplitude and B_z .

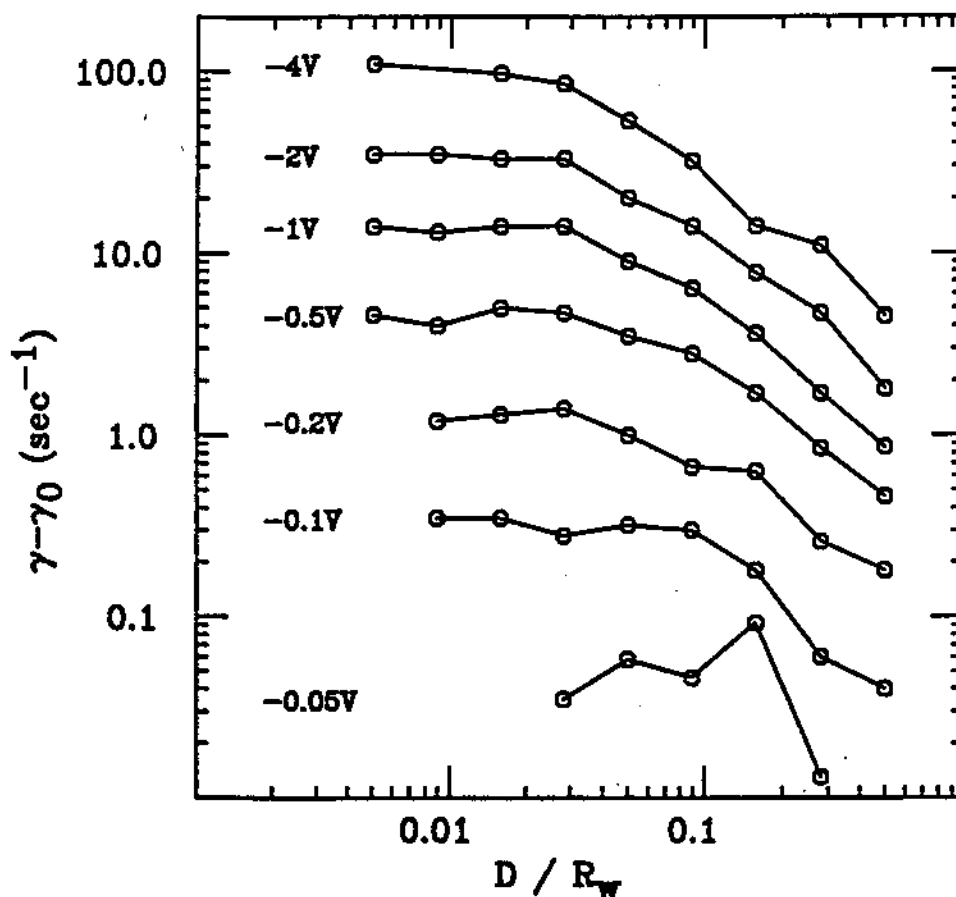


Figure 6.2: Measured damping rate versus amplitude for various values of V_{pert} for $B_z = 188$ gauss. The curves merely connect the points in each set.

output is then pulsed to a voltage of V_{pert} . At this time there will be an electric field between the two parts of the containment section that will be azimuthally symmetric ($l = 0$). This is called a 'squeeze' perturbation, since the field will tend to squeeze electrons from one part of the containment section to the other.

The log of the amplitude of the diocotron mode is plotted at the bottom of Fig. 6.1. Two consecutive shots are shown. During both shots the diocotron mode is grown to an amplitude that is controlled by the amount of time that the resistive growth relay is energized. The perturbator is driven to V_{pert} on only the first shot.

Both shots are grown exponentially to the same amplitude using the growth resistor. After the growth relay is turned off, both shots still display a small growth due to the 50Ω resistor attached to the receiving sector. This growth rate, γ_0 , is measured during the second shot. The first shot displays an exponential decay at a rate γ , which is presumably due to a combination of damping due to squeeze and growth due to the resistor on the receiving sector. I assume here that $\gamma - \gamma_0$ is due to the squeeze field alone.

The dots on the amplitude graph indicate points at which the amplitude is measured by a differential sample and hold. With these measurements γ and γ_0 can be calculated. In practice, many such pairs of shots are taken and γ and γ_0 are average values.

Measurements of γ and γ_0 were taken varying V_{pert} , the diocotron amplitude, D , and B_z . The two pieces of the containment section were each 15.8 cm long in all cases. Fig. 6.2 plots $\gamma - \gamma_0$ versus D/R_w at $B_z = 188$ gauss, for various values of V_{pert} . It can be seen that $\gamma - \gamma_0$ is constant with mode amplitude below a certain value. The measurements in Fig. 6.2 were made by growing the mode to different amplitudes, and measuring the damping rate when the squeeze was first applied. Nevertheless, I believe that that Fig. 6.2 is a good characterization of the damping over time of a diocotron mode in the squeeze field. The region of constant $\gamma - \gamma_0$ then implies exponential damping. This was verified by the output of the spectrum analyzer, which displayed a straight line decay on the log-linear display for small amplitudes.

For amplitudes above a critical value, the damping rate is less than would be expected from the exponential damping at low amplitude. For large amplitudes Fig. 6.2 gives an approximate scaling of $\gamma - \gamma_0 \propto D^{-1}$.

Measurements of $\gamma - \gamma_0$ versus D and V_{pert} were also made at $B_z = 47, 94$

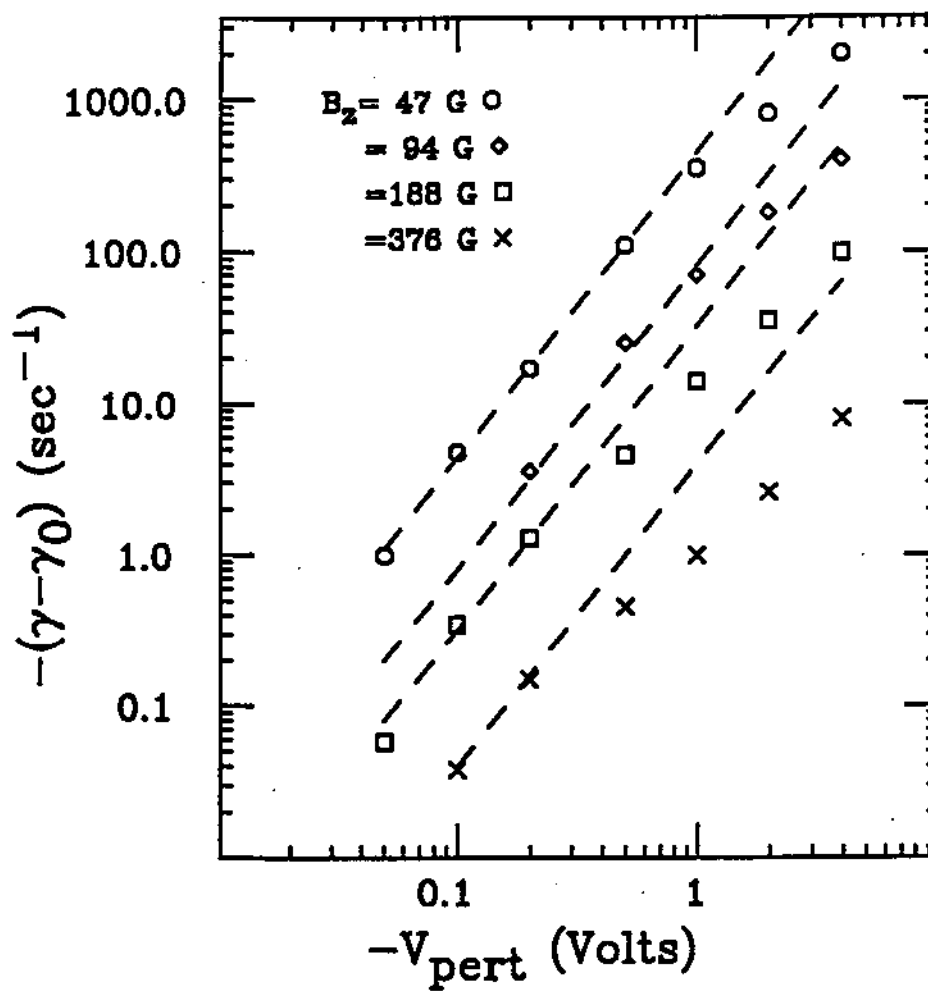


Figure 6.3: Measured exponential damping rate versus V_{pert} for four different values of B_z . Dashed lines are proportional to V_{pert}^2 .

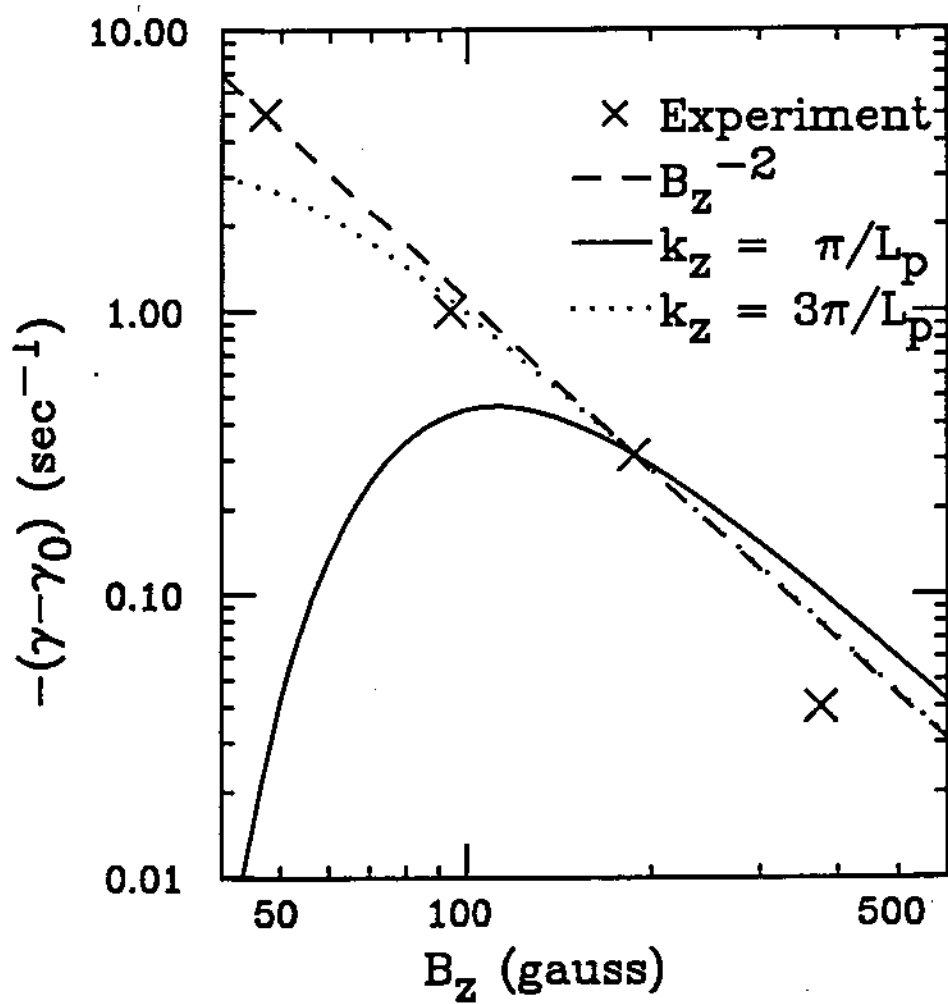


Figure 6.4: Measured exponential damping rate versus B_z for $V_{pert} = -0.1$ Volts (crosses). Also shown are the theoretical rates for $k_z = \pi/L_p$ and $k_z = 3\pi/L_p$, both of which are scaled to match experiment at $B_z = 188$ gauss.

and 376 gauss. The damping was found to be exponential at small amplitudes for all values of B_z . However, the curves of damping rate versus D at these values of B_z do not show as clean a separation between exponential damping and the damping proportional to D^{-1} as can be seen at $B_z = 188$ gauss.

The damping rate was measured in the region of exponential decay in Fig. 6.2, and is plotted versus V_{pert} in Fig. 6.3 at four different values of B_z . Note that all four sets of points show V_{pert}^2 dependence for small values of V_{pert} . Beyond a critical value of V_{pert} , the damping becomes smaller.

Figure 6.4 displays the damping rate versus B_z for $V_{pert} = -0.1$ Volts. It can be seen that the damping rate scales roughly as B_z^{-2} .

6.2.2 Relation to Beat-Wave Theory

One possible theoretical explanation of the above data is that the nonlinear interaction between the squeeze field and the diocotron mode produces a beat wave that interacts with resonant particles. This idea will become clearer with the aid of Table 6.1. The squeeze field is represented as a zero frequency wave with $l = 0$ and $k_z = \pi/L_p$. This wave interacts with the diocotron mode to produce a beat wave. The beat wave has mode numbers which are the sum of the two interacting waves. From Table 6.1, it can be seen that the beat wave is an $l = 1$, $k_z = \pi/L_p$ wave at the diocotron frequency, ω .

The predicted damping is essentially due to Landau damping of the beat wave, and is exponential with time. This prediction matches the observation of exponential damping in experiment in the small amplitude range. Furthermore, the decrease in damping rate above a certain amplitude could simply be due to modification of the velocity distribution, which could be expected to occur at larger amplitudes.

The expected scaling of damping with V_{pert} can be derived using a heuristic

	Azimuthal Mode Number	Longitudinal mode Number	Frequency
Squeeze	$l = 0$	$k_z = \pi/L_p$	$\omega = 0$
\pm Diocotron	$l = 1$	$k_z = 0$	ω
= Beat Wave	$l = 1$	$k_z = \pi/L_p$	ω

Table 6.1: Mode numbers and frequencies for squeeze, diocotron and beat waves.

argument taken from a paper by Ott and Dum [23]. The beat wave amplitude, ϕ_b is proportional to the product of the diocotron amplitude, ϕ_d , and V_{pert} : $\phi_b \propto \phi_d V_{pert}$. The damping rate of the diocotron mode is proportional to the ratio of the rate of energy dissipation by the beat wave and the energy associated with the diocotron mode, or $\gamma \propto \phi_b^2/\phi_d^2$. Combining the two proportionalities, we see that $\gamma \propto V_{pert}^2$, which is the scaling seen in experiment. Note here that even though the diocotron wave is *negative* energy, the energy change to damp the diocotron wave while P_θ is conserved is *positive* (see Section 5.4). This means that energy must be *absorbed* by the particle distribution in order to damp the diocotron wave.

The scaling of damping versus B_z is more complicated. The damping will change in part because the resonant velocity is a function of B_z . If v_{res} is the resonant parallel velocity, then

$$\omega - l\omega_r - k_z v_{res} = 0, \quad (6.1)$$

where ω_r is the plasma rotation frequency. Solving for v_{res}

$$\frac{v_{res}}{\bar{v}} = \frac{\omega_r - \omega}{\bar{v}k_z} = \frac{158}{mB_z}. \quad (6.2)$$

where $k_z = m\pi/L_p$, $T = 1$ eV, $R_p/R_w = 0.5$, $L_p = 26$ cm, $n = 10^7$ cm $^{-3}$ and B_z is

in gauss. From Crawford and O'Neil's theory, γ is predicted to be

$$\gamma \propto \frac{V_{pert}^2}{B_z} \times \frac{v_{res}}{\bar{v}} \exp \left[-\frac{1}{2} \left(\frac{v_{res}}{\bar{v}} \right)^2 \right]. \quad (6.3)$$

The scaling of γ versus B_z can be obtained by using Eq. 6.2 in Eq. 6.3. The results of this calculation for $k_z = \pi/L_p$ are plotted as the solid curve in Fig. 6.4, where the curve has been normalized to the experimental damping rate at $B_z = 188$ gauss. The peak in the curve is due to the fact that $v_{res} = \bar{v}$ in the middle of the graph. Clearly this curve does not match experimental scaling.

Higher k_z modes may be important. The squeeze electric field is a square wave in z , so that it can be thought of as having higher k_z components. The scaling of γ for $k = 3\pi/L_p$ is plotted in Fig. 6.4 as the dotted curve, where again it has been normalized so that it matches experimental damping rate at $B_z = 188$ gauss. This curve matches experimental scaling much better. For all higher k_z modes, the exponential in Eq. 6.3 is near one, and the scaling is $\gamma \propto B_z^{-2}$.

The relative importance of the various k_z modes of the squeeze electric field would require the evaluation of matrix elements in the theory of Crawford and O'Neil. This appears to be a difficult calculation, and I am left with an inconclusive result: theory matches the observed scaling of γ with B_z if higher k_z modes dominate, but there is no proof that this is the case.

6.2.3 Radial Transport due to Squeeze

Angular momentum should be conserved during the damping caused by the squeeze field as should electrostatic energy. This follows from the fact that the squeeze field is axisymmetric, and therefore P_θ is a conserved quantity. Since $P_\theta \propto \sum_j r_j^2$, this implies that the plasma must expand as its center moves to the axis of the conducting wall (i.e. D goes to zero).

Radial profiles of a plasma undergoing this process are shown in Fig. 6.5.

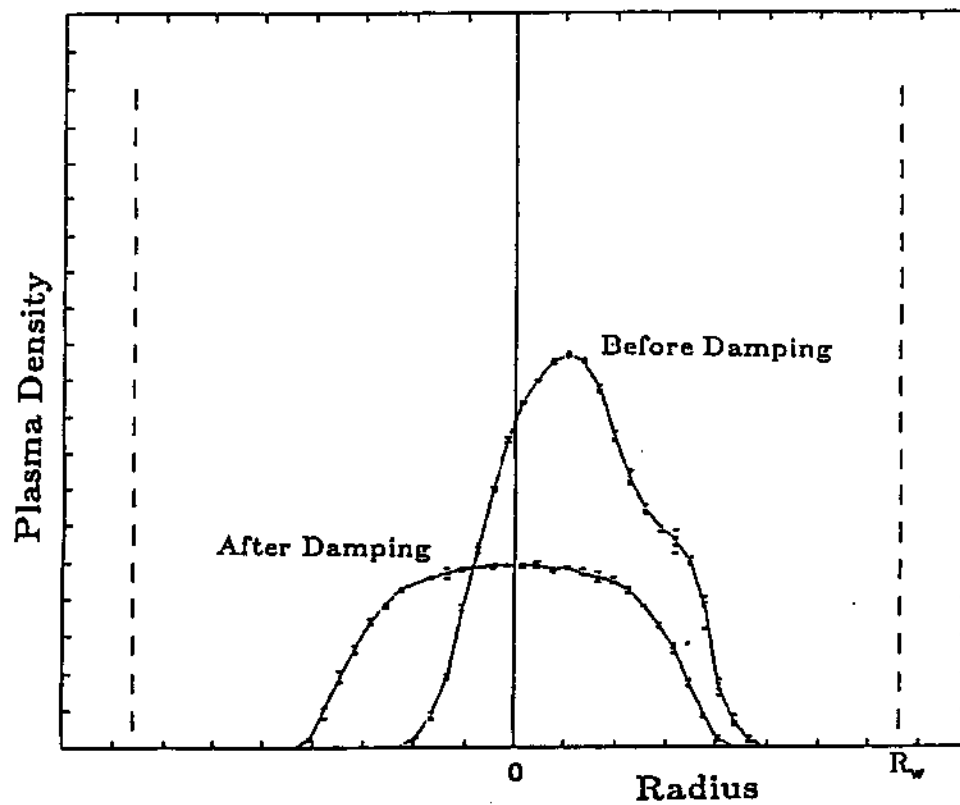


Figure 6.5: Phase-locked radial profiles of the plasma before squeeze damping and after 30 dB of damping. The asymmetry in the 'before damping' profile is due to dump smearing and does not exist in the plasma.

The profiles were taken with the phase-locked technique described in Chapter 4, and are scans approximately through the center of the plasma. It can be clearly seen that the plasma is becoming more broad and that the density is dropping. Note that the asymmetry in the 'before damping' profile is due to dump smearing (see Section 4.2.1), and does not actually exist in the plasma.

An experiment was performed to test the conservation of P_θ . As was previously mentioned, P_θ can be calculated from radial profiles without knowing the z -dependent structure of the plasma. This technique is somewhat complicated by the θ dependence of the diocotron mode. This problem is solved by averaging: if a non-phase locked radial profile is taken of a plasma orbiting with a large diocotron mode, and if a large number of shots per radial point are taken, then the average of all the shots taken at that radius will give the θ -averaged density at that radius. The θ -averaged density profile can then be used to calculate P_θ in the same way as for a centered profile.

The results of using this averaging technique to measure P_θ are shown schematically in Fig. 6.6. The abscissa is the time after injection, the ordinate is the log of the diocotron amplitude. The numbers between points are the changes in P_θ , expressed as percent of P_θ right after injection. The changes during four different processes are shown. One process is plasma containment without the diocotron wave grown, in which case P_θ decreases by 3.0% in 0.75 seconds, presumably due to external field errors. Another process is the growth of a diocotron wave by 25 dB using the resistive wall effect; in this case P_θ decreases by 16.3%. This relatively large change is to be expected, since the wave growth is induced by asymmetric fields.

A third process is the squeeze damping of the diocotron wave, during which P_θ is found to decrease by 2.1%. Note that this rate of loss of P_θ , about 4% per

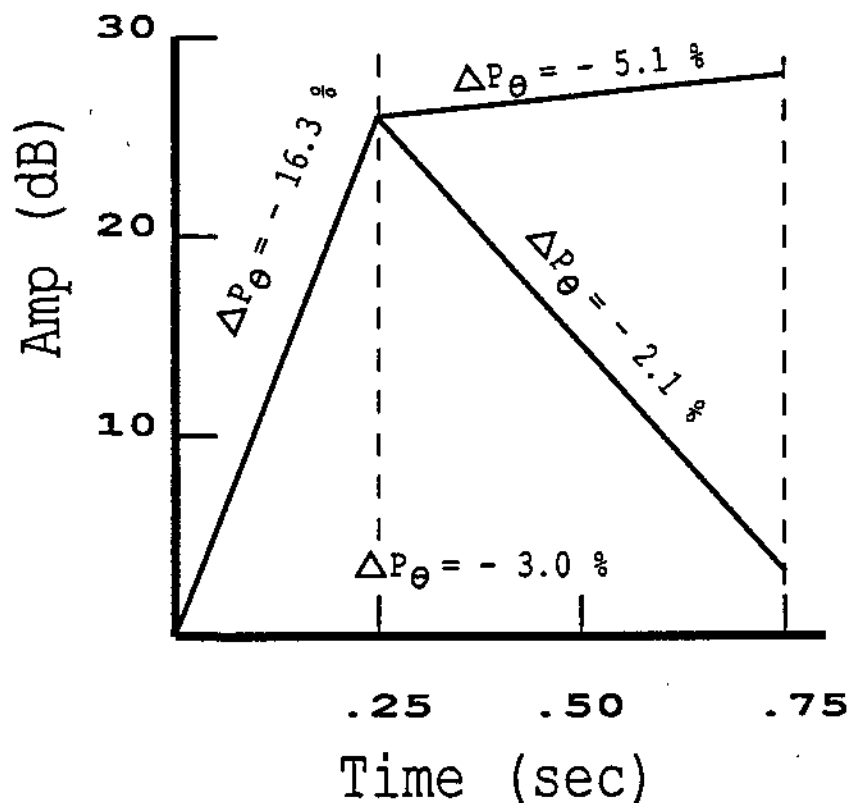


Figure 6.6: Changes in angular momentum during resistive growth feedback damping compared to no growth and growth but no damping.

second, is about the same as in the case where the diocotron mode is not grown. It is reasonable to assume that this loss is also due to external field errors.

The final process measured was growth of the diocotron mode without squeeze damping. The loss rate of P_θ is over two times the background rate in this case. This could be because of larger magnetic errors at bigger radius, or because of interactions with the wall, neither of which have been carefully studied.

To summarize, in contrast to the loss of angular momentum during resistive growth, angular momentum change during squeeze damping decreased the same rate as during background external transport. This supports the basic theoretical idea that axisymmetric fields conserve angular momentum.

6.3 Magnetostatic $l = 1$ Field Perturbations (Tilt)

In Chapter 2, the use of magnetic field tilt to create square, low noise plasmas was discussed. In this section I will discuss the experimentally observed scalings of the tilt transport with L_p , tilt angle and B_z .

An illuminating measure of the transport caused by tilt is the rate of momentum change, $\nu_p \equiv (1/P_\theta)(dP_\theta/dt)$. If the fields were perfectly cylindrically symmetric, angular momentum would be constant and ν_p would be zero. A nonzero value of ν_p must be due to either the background field errors, the magnetic field tilt, or both. The advantage of ν_p is that it is a single number which gives a measure of the integrated effect of the non-symmetric part of the fields.

The angular momentum, P_θ , can be calculated directly from a radial profile using Eq. 2.5. An estimate of ν_p can be made from two profiles taken at different confinement times. In practice, the two radial profiles are measured in a single radial scan. At each radial point, the confinement time is alternated on consecutive shots. A number of these pairs of density measurements are taken, and the densities at the two times are averaged separately. The difference in average density between the two times is calculated and then the collimator plate is moved to another radial location. This is essentially a form of coherent detection.

Another measure of the transport rate is the rate at which the central density decreases, $\nu_0 \equiv (1/n_0)(dn_0/dt)$. The typical initial radial profile is somewhat peaked at the center, and the field tilt causes this peak to go away. The value of ν_0 was measured by eye: I measured the central density difference between two radial profiles with a ruler, averaging over irregularities.

I define the tilt angle, $\Delta\theta = (B_x - B_{x,min})/B_z$, to be the angle between \vec{B} and the magnetic field direction where ν_0 is minimized. The values of ν_p and ν_0 versus tilt angle for three different containment cylinder lengths, L_c , are shown in

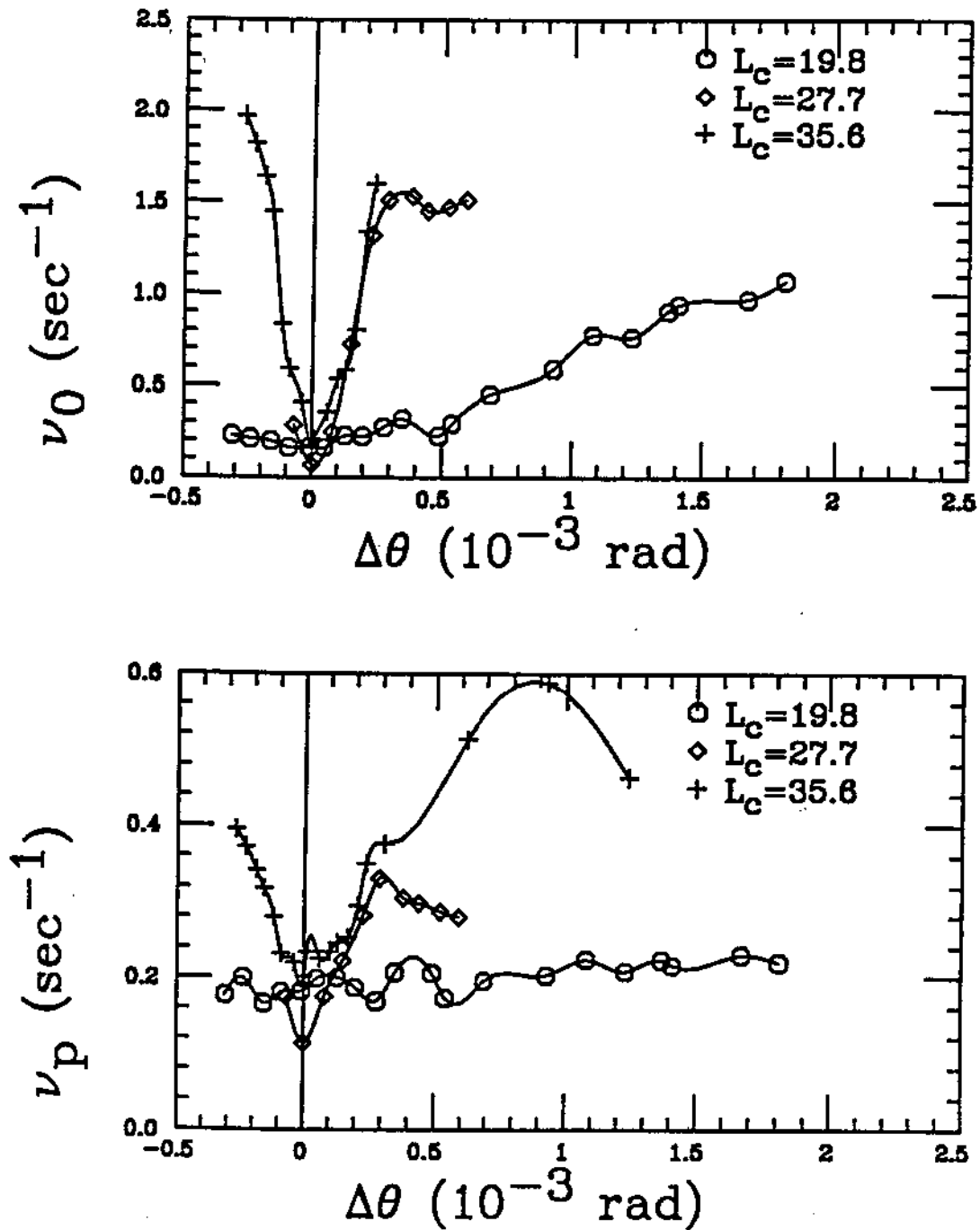


Figure 6.7: Transport rates ν_p and ν_0 versus magnetic field tilt angle for three different confinement lengths. All data was taken with $B_z = 94$ gauss.

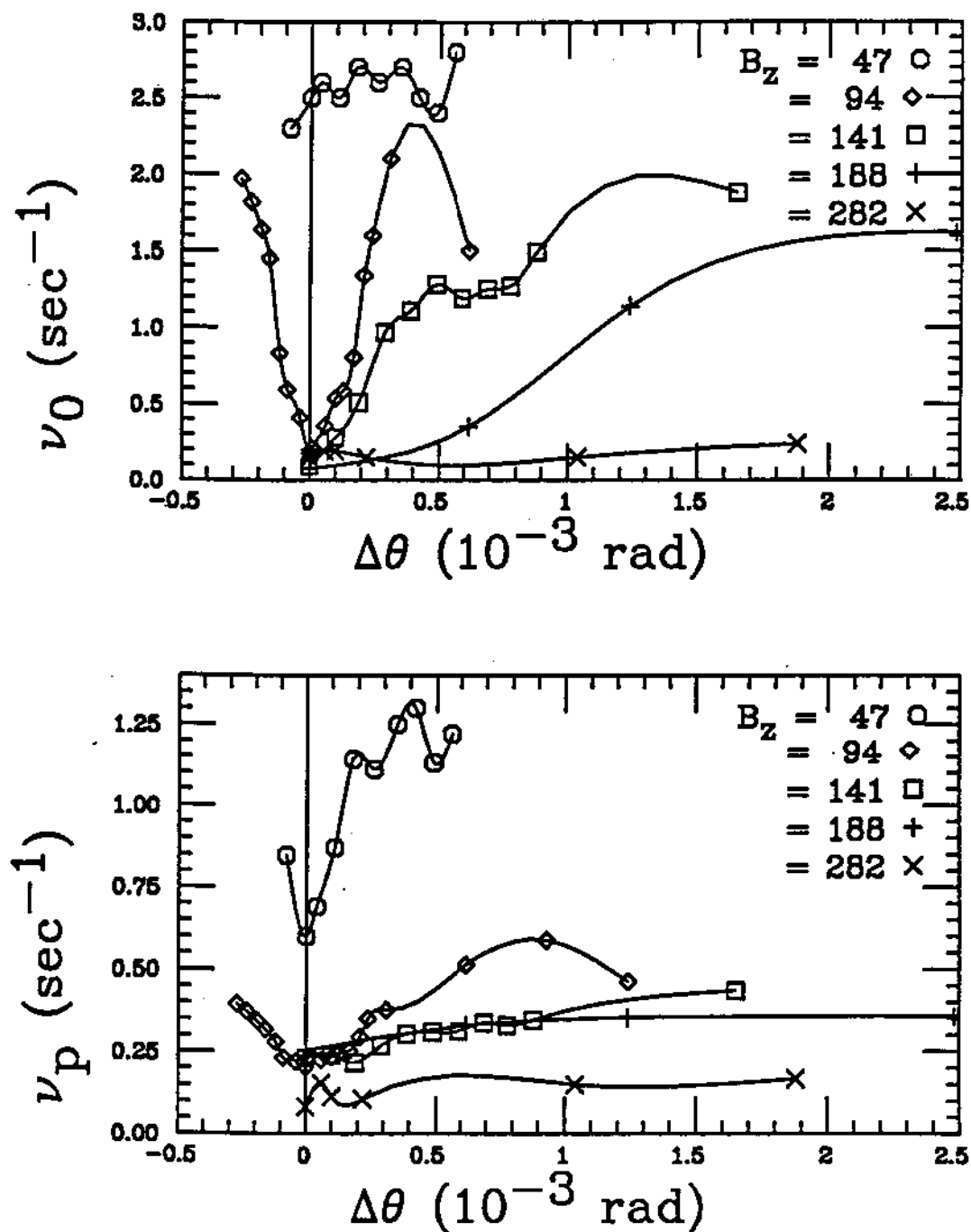


Figure 6.8: Transport rates ν_p and ν_0 versus magnetic field tilt at different values of B_z . All data was taken for a confinement length of 35.6 cm.

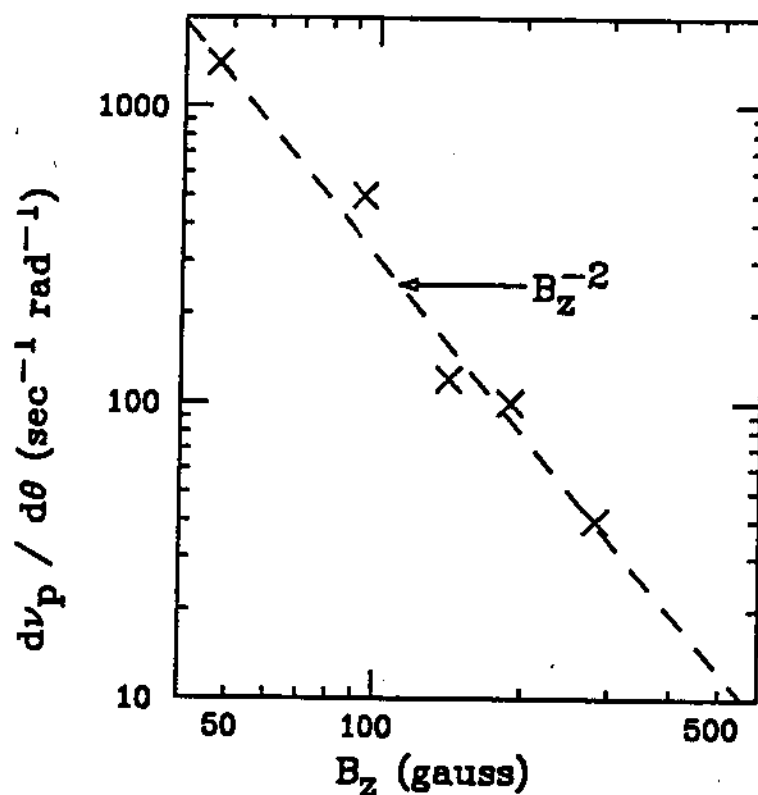


Figure 6.9: Sensitivity of ν_p to tilt angle versus B_z .

Fig. 6.7. These transport rates were measured shortly after injection. All density changes were measured between an initial dump time of 0.017 seconds and a time at which P_θ had decreased by a few percent. The minimum of ν_p is located at approximately $\Delta\theta = 0$. The tilt effect was measured at even shorter lengths, and very little effect was observed.

The value of ν_p at zero tilt angle is presumably due to background field errors. This transport has been previously found to scale approximately at a rate proportional to $(L_p/B_z)^2$ (see Section 2.6). The fact that the scaling shown in Fig. 6.7 does not scale as L_p^2 is not too surprising, since the data of Reference [10] has almost a decade of scatter and was taken for much longer confinement times.

There is clearly a strong length dependence to the data shown in Fig. 6.7.

The effect of tilt is much stronger in longer plasmas.

Figure 6.8 displays ν_p and ν_0 versus tilt angle at different values of B_z for $L_p = 35.6$ cm. Again the curves have minimums near zero tilt angle, with the exception of the curve of ν_0 at $B_z = 47$ gauss. The tilt transport is a strong function of B_z , with the strongest effect for small B_z . To get a rough idea of how the transport scales with B_z , I measure the slope $d\nu_p/d\theta$ near zero tilt angle and plot this slope versus B_z in Fig. 6.9. These measurements are factor of two at best. Nevertheless, Fig. 6.9 suggests that the effect of the tilt transport at a given tilt angle scales approximately as B_z^{-2} .

The tilt transport also decreases shot-to-shot variability of the density measurement. Fig. 6.10 displays the results of an experiment to compare the shot-to-shot variability of a plasma with the field tilted to the same plasma without the field tilted. A total of 64 shots were taken at each of several dump times; each set of 64 was averaged to obtain n_r and the standard deviation δn_r was calculated. Figure 6.10 plots n_r and δn_r versus dump time. The tilt causes n_r to decrease faster than without tilt, but causes δn_r to decrease even faster. An improvement of five to ten in shot-to-shot repeatability is usually found. In experiments where statistical averaging is used, this corresponds to 25 to 100 times fewer shots for the same uncertainty!

The tilted profiles appear similar to thermal equilibrium shapes: the temperature profiles are flat, and the density profiles are square. However, the edges are too steep for the measured temperatures. O'Neil and Driscoll [22], and also Prasad and O'Neil [25], have calculated the shapes of thermal equilibrium pure electron plasmas. They find that for long plasmas (a few R_p in length), the radial profile thermal equilibrium shape is approximately square with an edge that decreases in density from 90% to 10% of the central density in a distance of about

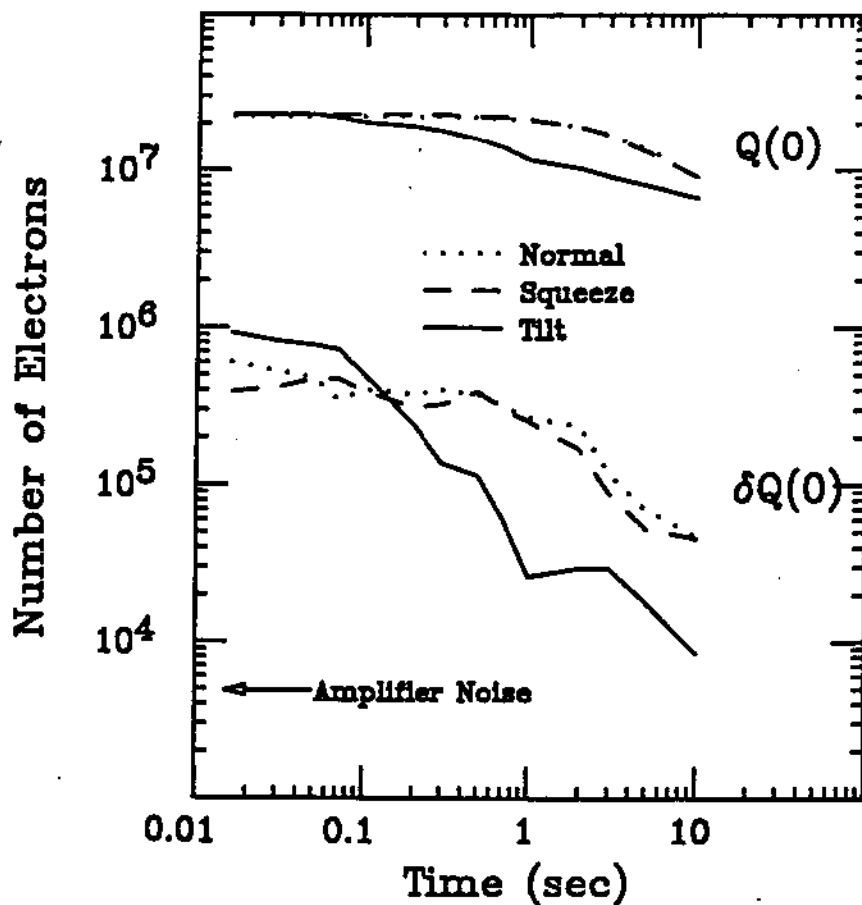


Figure 6.10: Decrease in shot-to-shot noise due to tilt transport. The number of electrons collected with the collimator hole centered, $Q(0)$, and the standard deviation of this signal for 64 shots, $\delta Q(0)$, are plotted versus dump time. These curves are shown for three different situations: normal operation, with the squeeze perturbation, and with the tilt perturbation.

$2\lambda_D$. The tilted profiles do not match this edge criterion. For example, the plasma in Fig. 2.2b drops from 90% to 10% density in a distance of about 0.74 cm, but $\lambda_D \approx 0.83$ cm.

The thermal equilibrium plasma has a constant rotation frequency as a function of radius, *i.e.* it is a rigid rotor. The rotation rate is composed of an $\mathbf{E} \times \mathbf{B}$ drift and a diamagnetic (∇P) drift, with the diamagnetic drift largest at the edge. The tilt profiles resemble a plasma in which only the $\mathbf{E} \times \mathbf{B}$ drift is a constant with radius. Perhaps the tilt causes an internal mixing that is sensitive only to the $\mathbf{E} \times \mathbf{B}$ drift rate.

The thermal equilibrium plasma state has been observed in the EV apparatus, and this state typically has lower shot-to-shot jitter than the initial state. This is presumably because the final state is determined by initial total energy, angular momentum and number of particles; all of which have much less jitter than the initial radial density measurements. The final tilt shape appears to be an expanding square profile. Perhaps this expanding shape has greater shot-to-shot repeatability for reasons similar to those for the thermal equilibrium case.

There will be electrons that are in resonance with the tilt perturbation. It may be that these particles are responsible for the transport. No one has yet created a careful resonant particle theory for the tilt transport, or explained the reason tilt causes the transport to a profile that is flat in density and temperature. The tilt field is a simple perturbation with a dramatic signature; if it was explained, it could become a paradigm for transport due to field asymmetries.

Appendix A

Estimate of Electron Loss inside Collimator Hole

When the plasma is dumped, exiting electrons encounter the collimator plate, and a fraction of them will go through the plate and be measured by the collector (see Fig. 2.1). If the plate were infinitely thin, then the number that would pass through would be those electrons that happened to be inside the collimator hole when the electrons first encounter the plate.

The plate actually has a thickness of 0.159 cm. Electrons will continue to spiral along cyclotron orbits while journeying through the collimator hole, and a fraction of these will collide with the hole wall and be lost. In this appendix I estimate this fraction, and find that this fraction is 3%–4% for the EV experiment at a temperature of 1 eV, independent of B_z .

The collimator plate is biased to +158 V, so that all electrons will have at least 158 eV of energy at the plate. The cyclotron frequency for electrons is $f_c = 2.8 B_z$ MHz, where B_z is in gauss. At an energy of 158 eV, an electron will travel an axial distance $l_c = 266/B_z$ cm during one cyclotron oscillation, and while inside the plate will execute

$$\eta = 6 \times 10^{-4} B_z \quad (\text{A.1})$$

fractions of an orbit.

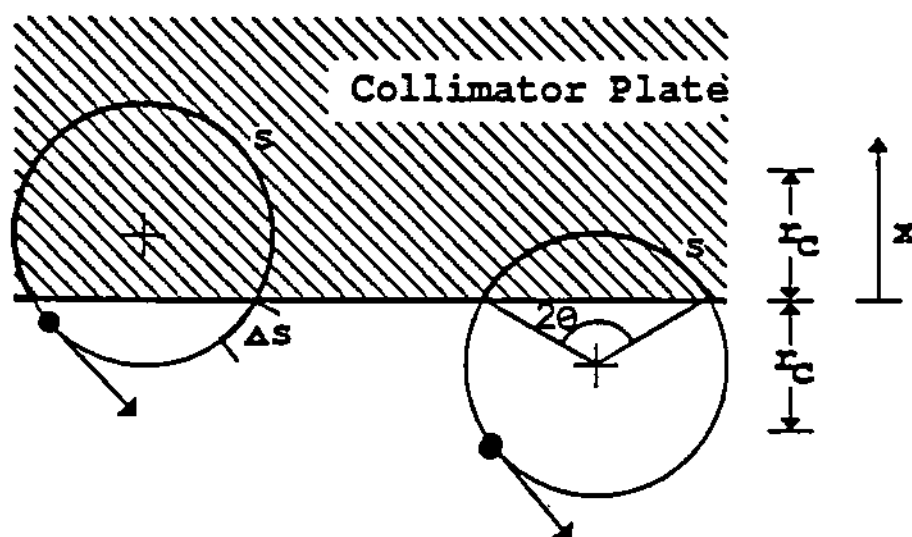


Figure A.1: Geometry of cyclotron orbits near collimator hole edge.

The situation is illustrated by Fig. A.1. I assume that the collimator hole radius is much larger than the cyclotron radius, r_c , so that the hole edge can be considered straight. The coordinate x measures the location of the guiding centers. Assume that the density of guiding centers is constant over the collimator hole. Consider for the time being a group of electrons all with the same r_c . Note that only electrons with $x > -r_c$ can collide with the hole edge.

The position of electrons in their orbits will be random before electrons encounter the hole. The fraction of electrons with guiding centers at x passing through the hole is

$$\text{Fraction passing through hole} = 1 - \frac{s + \Delta s}{2\pi r_c}, \quad (\text{A.2})$$

where s is the arc length of the cyclotron orbit that intersects the plate, and Δs is

the arc length the electron moves through while inside the hole. Note that

$$\frac{\Delta s}{2\pi r_c} = \eta. \quad (\text{A.3})$$

The arc length is given by

$$s = 2r_c \cos^{-1} \left(-\frac{x}{r_c} \right). \quad (\text{A.4})$$

The fraction of electrons, f , in the range $-r_c < x < r_c$ that pass through the collimator hole is given by averaging Eq. A.2 over x :

$$f = \frac{1}{2r_c} \int_{-r_c}^{r_c \cos \eta \pi} \left[1 - \eta - \frac{1}{\pi} \cos^{-1} \left(-\frac{x}{r_c} \right) \right] dx. \quad (\text{A.5})$$

Here, the upper limit is the point where $\Delta s = 2\pi r_c - s$, since all electrons will collide with the wall beyond this point. Assuming $\eta \ll 1$, and integrating Eq. A.5,

$$f = \frac{1}{2} - \eta + \mathcal{O}(\eta^2). \quad (\text{A.6})$$

Equation A.6 can also be derived from a symmetry argument. For each electron with guiding center at x and arc length s , there will be another electron at $-x$ with arc length $2\pi r_c - s$, as shown in Fig. A.1. Summing the two fractions, exactly half of the electrons in the range $-r_c < x < r_c$ will pass through in the limit $\Delta s = 0$. In addition, the effect of small Δs is that a fraction η of incoming electrons will collide while inside the hole.

Using Eq. A.6, the overall correction to the collimator area can be estimated. The number of electrons lost while inside the hole is approximately the number of electrons in a strip $2r_c$ wide and $2\pi R_h$ long times η . This is effectively a change in the collimator hole size by ΔA_h :

$$\frac{\Delta A_h}{A_h} \approx -\eta \frac{2\pi R_h 2r_c}{\pi R_h^2} = -4\eta \frac{r_c}{R_h}. \quad (\text{A.7})$$

Equation A.7 can be averaged over particles with different r_c . The average radius of a cyclotron orbit is

$$r_c = \frac{2.38 T_{\perp}^{1/2}}{B_z} \text{ cm}, \quad (\text{A.8})$$

where $T_{\perp} \equiv$ perpendicular temperature in eV.

Using Eqs. A.8 and A.1 in Eq. A.7, and taking the hole radius $R_h = 0.159$ cm, the fractional area change is

$$\frac{\Delta A_h}{A_h} \approx -0.036 T_{\perp}^{1/2}. \quad (\text{A.9})$$

At a typical temperature of 1 eV, 3%–4% of the electrons will be lost to the collimator hole edges, independent of B_z .

Appendix B

Image Charge in Cylindrical Geometry

Consider an infinite, conducting cylindrical wall of radius R_w containing a line charge with charge per unit length $-N_L e$ (see Fig. 3.1, page 27). The line charge is displaced from the axis of the conducting wall by distance D . Define coordinates (r, θ) with origin at the wall axis, and with the line charge at $\theta = 0$. We wish to solve for the potential $\Phi(r, \theta)$ everywhere inside the conducting wall.

The method of images is based upon the mathematical statement that the grounded wall can be replaced by a collection of 'image' charges outside the wall radius. These image charges, along with the line charge, satisfy the boundary condition $\Phi(R_w, \theta)$ constant. Since the charge interior to the wall and the boundary condition are the same, the solution to Poisson's equation is identical (see Jackson [16, page 54]). Our goal here is to find the appropriate image for this case.

Make the guess that the image charge is another line charge with opposite charge per length $+N_L e$, and place this image at radius S . From symmetry, the image charge must lie along the same radial line ($\theta = 0$) as the line charge. Using the solution of potential for an infinite line charge:

$$\Phi(r, \theta) = -\frac{N_L e}{2\pi\epsilon_0} \left[\ln \sqrt{r^2 + D^2 - 2rD \cos \theta} - \ln \sqrt{r^2 + S^2 - 2rS \cos \theta} \right], \quad (\text{B.1})$$

where the second term is the potential due to the image. Rewrite Eqn. B.1 as

$$\Phi(r, \theta) = -\frac{N_L e}{2\pi\epsilon_0} \ln \left[\frac{r \sqrt{1 + D^2/r^2 - 2D \cos \theta/r}}{S \sqrt{1 + r^2/S^2 - 2r \cos \theta/S}} \right]. \quad (\text{B.2})$$

If we make the choice $S/R_w = R_w/D$, then at $r = R_w$

$$\Phi(R_w, \theta) = -\frac{N_L e}{2\pi\epsilon_0} \ln \left(\frac{D}{R_w} \right), \quad (\text{B.3})$$

which meets the boundary condition of constant potential at the wall. The expression for S is easiest to remember in normalized coordinates; $d \equiv D/R_w$ and $s \equiv S/R_w$:

$$s = \frac{1}{d}. \quad (\text{B.4})$$

References

- [1] R. J. Briggs, J. D. Daugherty, and R. H. Levy. Role of Landau damping in crossed-field electron beams and inviscid shear flow. *Physics of Fluids*, 13:421, Feb 1970.
- [2] O. Buneman. Ribbon beams. *Journal of Electronic Control*, 3:507, 1957.
- [3] O. Buneman, R. H. Levy, and L. M. Linson. Stability of crossed-field electron beams. *Journal of Applied Physics*, 37:3203, July 1966.
- [4] J. D. Crawford and T. M. O'Neil. Nonlinear collective processes and the confinement of a pure-electron plasma. *Physics of Fluids*, 30:2076, 1987.
- [5] J. D. Crawford, T. M. O'Neil, and J. H. Malmberg. Effect of nonlinear collective processes on the confinement of a pure-electron plasma. *Physical Review Letters*, 54:697, 1985.
- [6] C. C. Cutler. Instability in hollow and strip electron beams. *Journal of Applied Physics*, 1028, Sep 1956.
- [7] Ronald C. Davidson. *Theory of Nonneutral Plasmas*. W. A. Benjamin, Inc., 1974.
- [8] J. S. deGrassie and J. H. Malmberg. Waves and transport in the pure electron plasma. *Physics of Fluids*, 23:63, 1980.
- [9] M. H. Douglas and T. M. O'Neil. Transport of a nonneutral electron plasma due to electron collisions with neutral atoms. *Physics of Fluids*, 21:920, 1978.
- [10] C. F. Driscoll, K. S. Fine, and J. H. Malmberg. Reduction of radial losses in a pure electron plasma. *Physics of Fluids*, 29:2015, 1986.
- [11] C. F. Driscoll and J. H. Malmberg. Length-dependent containment of a pure electron plasma. *Physical Review Letters*, 50:167, 1983.
- [12] C. F. Driscoll, J. H. Malmberg, K. S. Fine, R. A. Smith, X-P. Huang, and R. W. Gould. Growth and decay of turbulent vortex structures in pure electron plasmas. In *Proc. of 12th International Conference on Plasma Physics and Controlled Nuclear Fusion*, I.A.E.A., 1988.

- [13] Andrew V. Haeff. The electron-wave tube—a novel method of generation and amplification of microwave energy. *Proceedings of the I. R. E.*, 37, 1949.
- [14] A. W. Hyatt. *Measurement of the Anisotropic Temperature Relaxation Rate in a Magnetized Pure Electron Plasma*. PhD thesis, University of California at San Diego, 1988.
- [15] A. W. Hyatt, C. F. Driscoll, and J. H. Malmberg. Measurement of the anisotropic temperature relaxation rate in a pure electron plasma. *Physical Review Letters*, 59:2975, 1987.
- [16] J. D. Jackson. *Classical Electrodynamics, Second Edition*. John Wiley and Sons, 1975.
- [17] C. A. Kapetanacos and A. W. Trivelpiece. Diagnostics of non-neutral plasmas using an induced-current electrostatic probe. *Journal of Applied Physics*, 42:4841, 1971.
- [18] R. H. Levy. Two new results in cylindrical diocotron theory. *Physics of Fluids*, 11:920, 1968.
- [19] J. H. Malmberg and C. F. Driscoll. Long-time containment of a pure electron plasma. *Physical Review Letters*, 44:654, 1980.
- [20] J. H. Malmberg and T. M. O'Neil. Pure electron plasma, liquid and crystal. *Physical Review Letters*, 39:1333, 1977.
- [21] T. M. O'Neil. A confinement theorem for nonneutral plasmas. *Physics of Fluids*, 23:2216, 1980.
- [22] T. M. O'Neil and C. F. Driscoll. Transport to thermal equilibrium of a pure electron plasma. *Physics of Fluids*, 22:266, 1979.
- [23] Edward Ott and Christian Thomas Dum. Nonlinear Landau damping and beat wave trapping. *Physics of Fluids*, 14:959, 1971.
- [24] S. A. Prasad and J. H. Malmberg. A nonlinear diocotron mode. *Physics of Fluids*, 29:2196, 1986.
- [25] S. A. Prasad and T. M. O'Neil. Finite length thermal equilibria of a pure electron plasma. *Physics of Fluids*, 22:278, 1979.
- [26] S. A. Prasad and T. M. O'Neil. Vlasov theory of electrostatic modes in a finite length plasma. *Physics of Fluids*, 27:206, 1984.
- [27] S. A. Prasad and T. M. O'Neil. Waves in a pure electron plasma of finite length. *Physics of Fluids*, 26:665, 1983.

- [28] R. A. Smith, M. N. Rosenbluth, C. F. Driscoll, and T. M. O'Neil. Two-dimensional shear instabilities in a pure electron plasma. *Bull. Am. Phys. Soc.*, 33, 1988. To be published.
- [29] H. F. Webster. Breakup of hollow electron beams. *Journal of Applied Physics*, 1386, 1955.
- [30] W. D. White and J. H. Malmberg. Feedback damping of the $l = 1$ diocotron wave. *Bull. Am. Phys. Soc.*, 27:1031, 1982.
- [31] W. D. White, J. H. Malmberg, and C. F. Driscoll. Resistive wall destabilization of diocotron waves. *Physical Review Letters*, 49:1822, 1982.

